LAWRENCE
LIVERMORE
NATIONAL
LABORATORY

LLNL-TR-605934

FXR Optimization Project: Determining Beam Quality By Cathode Plasma Image Analysis

T. L. Houck, M. M. Ong, R. D. Paris

December 3, 2012

Disclaimer

This work performed under the auspices of the U.S. Department of Energy by Lawrence Livermore National Laboratory under Contract DE-AC52-07NA27344.

Table Of Contents

Table Of Figures

Brief History and Goals

The LLNL Flash X-Ray (FXR) Accelerator[1, 2] was the first accelerator in the US to be optimized for the radiography of thick explosive objects. FXR was also the first radiographic machine based on linear induction accelerator technology. Since its completion in 1982, FXR has been actively used for a large variety of explosive tests and has been periodically upgraded to achieve higher performance. For radiographic machines the figure of merit (FOM) for performance is described as x-ray dose divided by spot size. Upgrades have included improved transport magnets[3], redesign of the injector[4], impedance damping of the accelerator cells[5], novel magnetic transport techniques[6], improved pulsed power timing[7], and a new cathode configuration[8]. These upgrades primarily improved spot size by minimizing the transverse motion of the beam. The injector upgrade also increased beam energy leading to higher dose. A major upgrade in capability was the double pulse option that permitted two-frame imaging. There has been a parallel effort to improve reliability and maintainability of the accelerator by refurbishing and replacing ancillary systems, e.g. magnet power supplies, oil cleaning system, and SF_6 recovery system.

Most importantly, diagnostics have also been upgraded. Without improved diagnostics it would not have been possible to determine whether the upgrades had been effective and what the priority for upgrades should be. Several of the diagnostics will be mentioned and described in this paper including B-Dot probes, Beam Bugs (also referred to as Beam Position Monitors, BPM), and high speed, framing cameras.

The numerous upgrades have been successful and FXR's FOM has steadily improved as the x-ray spot size has decreased. Each upgrade has also made it possible to recognize the next phenomenon with the largest contribution to the existing spot size. Beam emittance, an inherent beam quality related to the parallelization of individual electron orbits, and back streaming ions from the target are presently the largest contributors to spot size. This report concerns a diagnostic for measuring the initial emittance of the beam.

Emittance is a critical beam quality. Once the beam is in thermal equilibrium, the normalized emittance, is a conserved quantity and will only increase as the beam quality degrades during transit of the accelerator. The larger the emittance, the larger the minimum spot size will be. Previous studies[9,10,11] of FXR led to the conclusion that the injector and, more specifically, the cathode were the source of higher than expected beam emittance. Images of the light produced on the cathode during the current pulse showed a very non-uniform light intensity distribution over the velvet emission surface. An assumption was that the light intensity correlated to the current density. A non-uniform current density indicates, or will lead to, a higher beam emittance. Increasing the electric field stress on the velvet was expected to improve the initial beam emittance through two mechanisms. First was that the time to reach "light-off", i.e. the point where explosive emission began, would be shortened allowing more sites on the velvet surface to emit before being effected by neighboring sites generating a more uniform current density. The second was that the area of the velvet, thus the area over which variations could occur, would be reduced while maintaining the same total emitted current. The success of this approach was demonstrated when the new cathode configuration produced the expected decrease in spot size.

Unfortunately, the beam emittance is difficult to measure with FXR's parameters and has only been attempted a few times[12,13,14,15]. The absolute value of FXR's emittance is not known with great certainty. The measured spot size provides an upper limit on the emittance value, but separating the various contributors to spot size on a regular and routine basis is not possible at this time. Establishing a new emittance diagnostic that is easy to deploy and measures emittance at the cathode would be a major accomplishment.

The primary goal for this study was to establish a relative emittance measurement based on images of the cathode during the high voltage, current pulse. At a minimum, the cathode image would provide and indication as to the suitability of the cathode emitting surface. The image could be used to determine if a new velvet installation was correct and would produce a quality beam. Also, by watching changes in the cathode image, one would be able to determine when the condition of the velvet had deteriorated to a degree that the velvet should be replaced. This goal has been achieved.

1 Introduction

This work is a continuation of earlier study that described a camera system[16] for imaging the plasma light generated on the surface of the FXR velvet cathode. Some mechanical improvements have been completed for improving the structural stability of the camera and mirror that were recommended. That study also suggested several future tasks:

- Collect baseline images, especially before and after changing the velvet to:
  - determine the wear on the velvet
  - determine beam centroid position
  - determine intensity, possibly with absolute flux levels
  - analyze beamlet patterns
  - determine the condition of the cathode shroud
- Develop software tools to:
  - support the above analysis
  - automate the collection of images and analysis
  - archive the images and analytical results
- Study the effect of ultraviolet (UV) illumination and other technologies to generate better current uniformity.

This study accomplished a number of the above tasks and generated a new list. The most important task involved analyzing the beamlets or emission spots in the cathode images and establishing a relationship between image characteristics and beam quality.

A pertinent question to ask is why we started another study of the cathode images after a five-year lapse since establishing the cathode camera. There were three reasons for doing this new study:

1. Installation of a new cathode configuration – a new baseline needed to be established
2. Improved reproducibility – performance characteristics are no longer masked by random variations
3. Better acquisition & analysis software – trends in performance can be established and quickly correlated

An early stimulus for starting this study of the cathode image was a changing cathode surface appearance during the pulse. Figure 1-1 shows a series of cathode images starting with the original large velvet configuration on the left that shows the spotty distribution of light. Section 2 discusses how the images are attained, viewing angle, and operating definitions. Images a, b, and d were taken with 10 ns exposures about 30 ns after the start of the pulse. Image c was taken with 100 ns exposure starting about 20 ns before the pulse. The second image (b) of the series is of the first velvet with the new cathode and indicates an improved uniformity of the light distribution. After a short test with the reconfigured cathode, the original cathode was reinstalled for operational reasons. Some months later the cathode was returned to the new configuration and it was noted that the cathode image did not appear to be as uniform as before. Following a series of discussions concerning the velvet installation technique, a third velvet (c) was installed which also exhibited a less

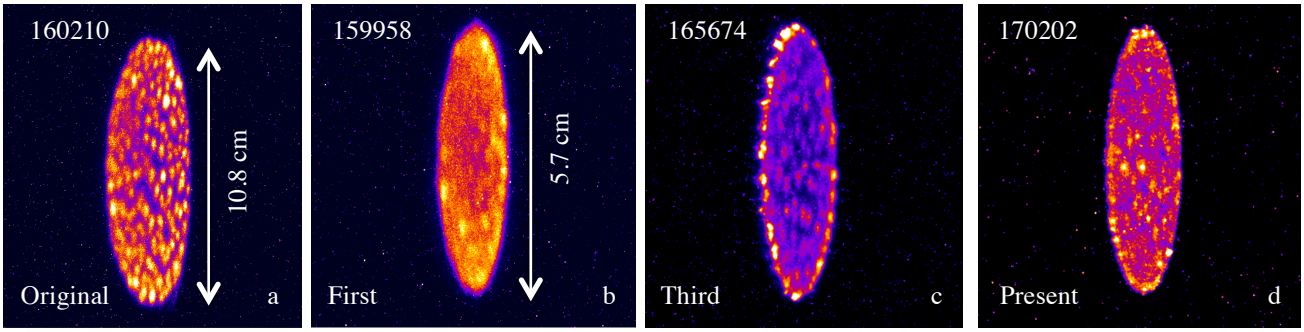

Figure 1-1. Images of the FXR cathode during the current pulse: a) original large cathode configuration, b) first velvet with new configuration, c) third velvet with new configuration, and d) the velvet installed during this study.

than desirable uniformity. The final image in the series is of the velvet for this study. The important point to Figure 1-1 is that a change was made to the cathode configuration that improved the uniformity of the light associated with the velvet emission surface and on subsequent changes of the velvet the uniformity degraded for unknown reasons.

The second observation that indicated a need to reexamine the cathode was the perveance. Determining the quality of the electron source or cathode in an operational injector is often limited to simply checking the perveance, that is the amount of current produced for an applied diode voltage. Refer to Appendix E for more details on perveance. In the case of thermionic cathodes, the cathode surface temperature may be measured with an optical pyrometer if a viewing port is

available. Otherwise the temperature can be inferred by a thermal probe located in a low electrical field stress region of the diode or by the filament heater power. Knowing the temperature and emission as a function of time allows the expected lifetime, or replacement time, to be determined. For a field emission (velvet) cathode, determining when the velvet needs to be replaced is problematic. The emitted current and/or perveance can show little change even when there is significant change to the appearance of the velvet surface in terms of color and material condition. However, the emittance of the produced beam may be seriously degraded. There is little or no information relating the effect of changing perveance on the beam's emittance in an operational injector. What was noted with the FXR injector after the cathode reconfiguration was a decline in perveance when the velvet was replaced as shown in Figure 1-2.

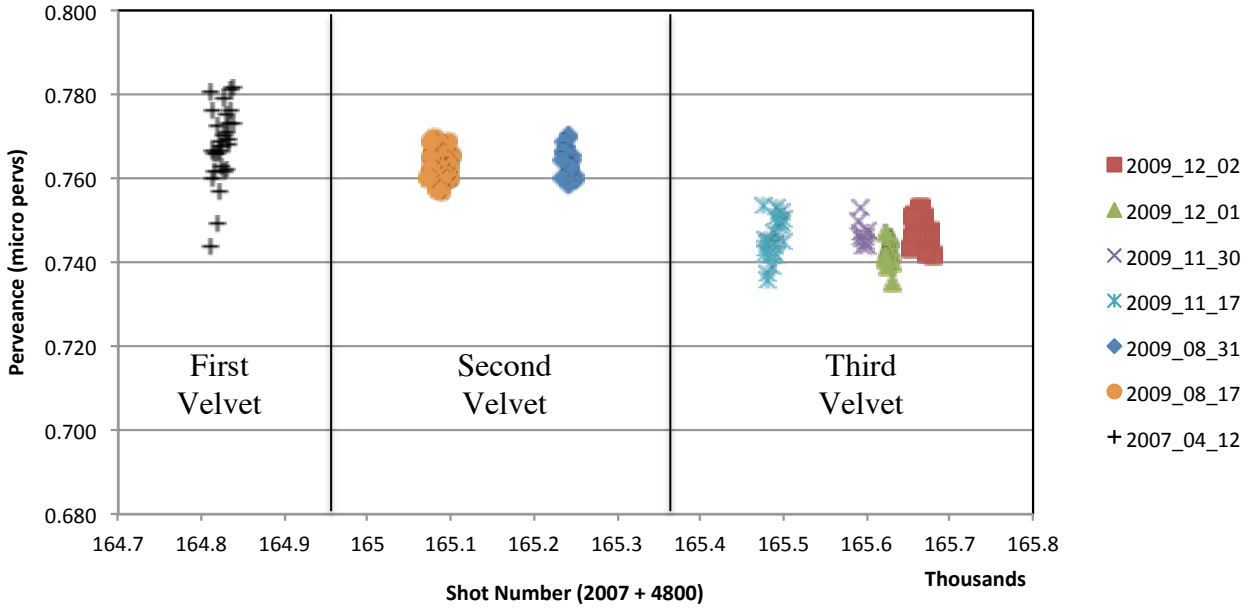

Figure 1-2. Perveance is plotted for different "shots", i.e. high voltage pulses on the diode.

A number of caveats are associated with Figure 1-2. Perveance is defined as $I/V^{3/2}$, where I is the current measured at the exit of the injector (I35 BPM) and V is the voltage on the diode. In Section 2 *Equipment and Experiments*, *Relating Images to Beam Parameters*, the loss of current between the cathode and the exit of the injector is discussed. A more accurate measurement of the emitted current would be at the diode (I20 B-Dot). The variation in the perveance during a day is due to minor variations in beam energy (diode voltage) leading to a change in the amount of current lost in transmission through the injector. For the "First Velvet" case, the magnetic field to transport the beam was intentionally adjusted leading to varying current loss and calculated perveance. However, the variation in the daily average current shown in Figure 1-2 is not easily explained and was unexpected since operational parameters were kept the same.

Emittance is difficult to measure for the FXR beam parameters and cathode replacement is time consuming. Exiting the injector the beam is space charge dominated. The diameter and expansion of the beam is determined by the enclosed charge. A mask can be placed in the path of the beam allowing only a small "beamlet" to pass and reducing the effects of space charge. This technique is referred to as a pepper pot measurement. To accomplish such a measurement part of the accelerator would need to be removed to allow placement of the diagnostic. Even then there are complications due to the intensity of the beam, scattering effects, etc. Optical Transition Radiation (OTR) is impractical at low energy as the wide-angle light cone is difficult to capture through a normal viewport. At the exit of the accelerator the beam is less space charge dominated, but needs to be reduced significantly in diameter to be truly emittance dominated. At the required diameters the intercepting imaging foils are damaged/destroyed. The use of OTR is a viable option at the accelerator exit. Unfortunately OTR emittance measurements are a very time consuming effort. Also, measurements performed at the accelerator exit have the disadvantage of not indicating whether the emittance is solely due to the cathode or if there is a flaw in the transport of the beam in the accelerator.

In this study the emphasis was in developing the cathode camera as a useful diagnostic for determining cathode performance with respect to producing low emittance beams. The camera system was automated to permit the collection, analysis, and display of the images with a FOM. A description of the equipment involved, experiments and data, image analysis performed with supporting computer simulations, and recommendation for further work is provided in the following report.

2 Equipment and Experiments

In this section the equipment and image acquisition technique is described. The experimental plan and equipment parameters for specific images are listed in Appendix A. The cathode images will have a six digit "Shot Number" provided along the lower edge of the image that matches with the "Shot Number" listed in the experimental plan and in the FXR Operations Log Book. The Shot Number is used to index all accelerator and beam measurements. The cathode mages were taken with a gated, intensified, scientific camera. The evolution of the cathode light was achieve by adjusting the start and duration of the exposure time, i.e. the time the microchannel plate of the camera was active, relative to the voltage pulse applied to the diode. To accomplish this it was necessary to demonstrate the repeatability of the setup and phenomena as only one image was acquired per voltage pulse. A major goal was to relate the cathode images to beam parameters. This also required establishing a time link between various diagnostics and the camera trigger/exposure time.

Figure 2-1 shows a sketch of the injector with the diode, two diagnostics (B-Dot and BPM), and transition zone labeled. The beam, depicted in red, originates on the cathode, is transported through the anode portion of the injector and passes through a beam position monitor (BPM) before entering the accelerator. I20 and I35 are location designations.

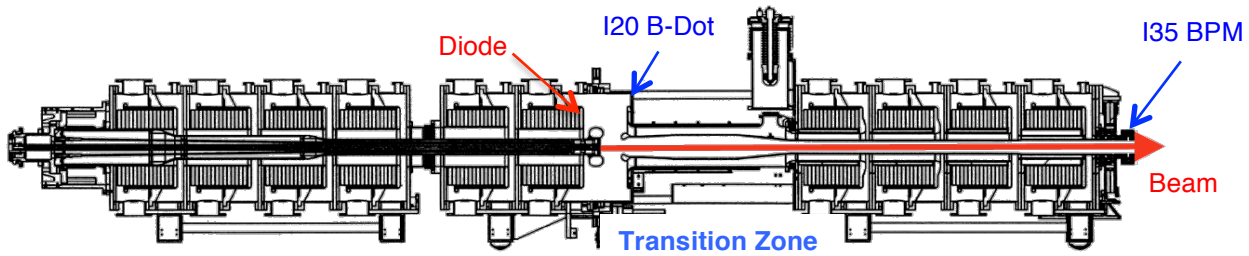

Figure 2-1. Schematic of the FXR Injector.

Cathode Camera and Velvet Cathode

A Princeton Instrument PI-MAX camera housed inside a Faraday enclosure was used to take photographs of the light formed on the surface of the cathode during the high voltage pulse. Refer to Figures 2-2 and 2-3. The camera, a first generation PI-MAX, is a high performance intensified camera system featuring a high-resolution CCD fiberoptically coupled to a Gen II intensifier. The images are 1,024 by 1,024 pixels with 16-bit depth (65,536). Nano-second (minimum 2 ns) gating capability and an integrated programmable timing generator (PTG) permit a wide range of gate widths (exposures) and delays. Due to the dimness of the cathode plasma light especially for short exposures, the camera gain was set at the maximum (255) with a small F-number (f/2.8) for the images in this study. In Figure 2-2 the larger black box is the controller and PTG with the camera along side in the foreground.

Figure 2-2. PI-MAX camera in Faraday enclosure.

The first generation PI-MAX cameras are susceptible to gamma radiation in that CCD elements will be charged by a passing gamma producing a saturated pixel in the image. This effect is often referred to as starring and can be seen in our images. To reduce the starring problem the Faraday enclosure has several inches of lead shielding on the sides adjacent to the injector (radiation source). Figure 2-3 shows the camera and Faraday Enclosure positioned next to the diode region of the FXR Injector. The cathode portion of the injector is in the foreground. The view of the cathode is at a relative large angle

Figure 2-3. Faraday enclosure containing the camera is positioned next to the FXR Injector.

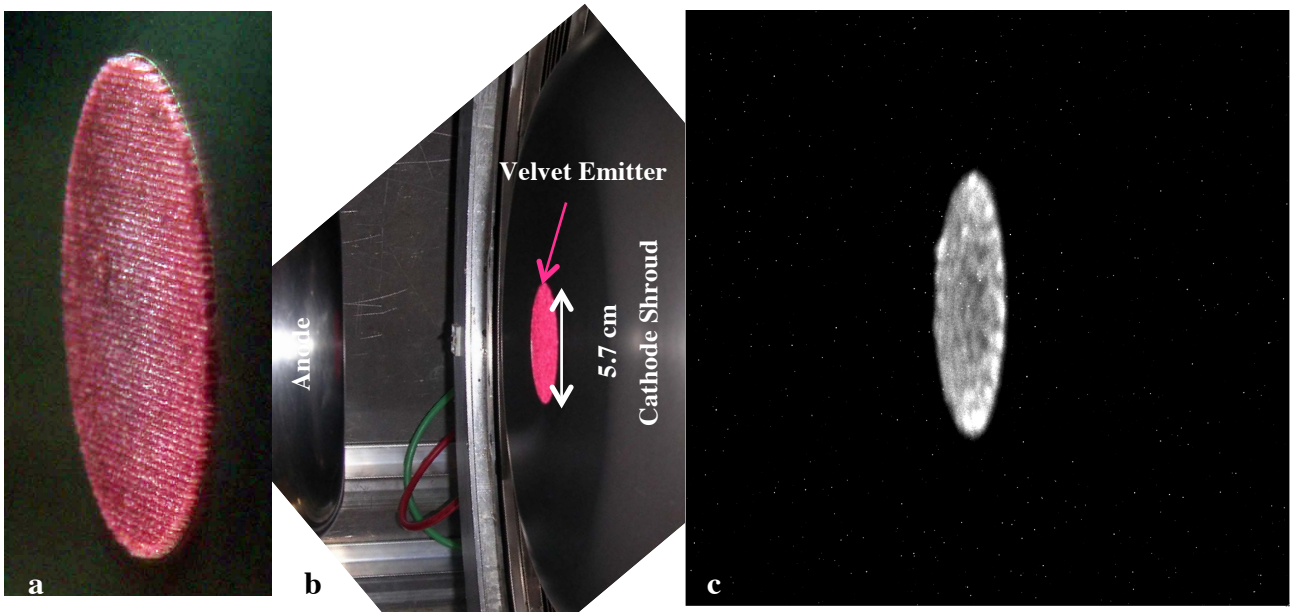

Figure 2-4. Camera views of FXR velvet cathode: a) close up of the synthetic velvet protruding ~1 mm beyond the face of the cathode shroud, b) larger view showing the cathode shroud with cathode and the anode, c) raw cathode image.

to the surface normal (74°) through a quartz port on the vacuum chamber surrounding the diode region of the injector.

Figure 2-4 shows the camera view of the diode region and the resulting foreshortening of the circular cathode velvet. The cathode velvet material is 100% rayon, Lucia brand, mounted to a 304 stainless steel surface with double-sided tape. For many of the analyzed images shown in this paper the raw image has been stretched in the horizontal plane to provide a pseudo forward view of the surface. Long exposures using physical light were used to image the velvet and establish a mechanical center with respect to the image center that was used as a reference for the light formed on the surface. Refer to Appendix D for an example of a front illuminated image. The large viewing angle creates a problem with respect to the edge of the cathode. If the velvet is extended beyond the plane of the cathode shroud, the image records light from the side of the velvet in addition to the surface. Similarly, for the recessed velvet part of the surface is hidden below the edge of the cathode shroud. This will be discussed in the "Image and Data Analysis" Section below.

The field of view was set for an earlier cathode design that used an emitting surface almost twice the diameter of the present cathode[17] that was installed in May 2007. The 135 mm lens system was left unchanged resulting in a smaller than desired area of interest on the full cathode image. The lens system does allow a significant portion of the shroud to be monitored. The small F-number used limits the depth of field forcing a compromise between the sharpness of the far and near edges of the velvet. The camera focus was checked and varied to achieve an optimum for the study. The old focus was reasonably near optimum and focus does not explain the filled in "valleys" between the bright emission centers noted in the images. Resolution for the camera system is about 8 pixels/mm on the velvet surface in the vertical.

Source Of Visible Light

The light appearing on the surface of the cathode is assumed to be due to the plasma formed by explosive emission. No spectroscopic measurements were performed and we rely on the work of Krasik[18] and others to describe the plasma. The PI-MAX camera is sensitive to the expected H_α (656 nm) and H_β (486 nm) spectral lines. The light is correlated to the application of the high voltage pulse and extraction of current. There are indications that the more intense points of light are related to current conduction paths through the velvet backing material. There are no indications of fluorescence or photoluminescence of the velvet. There are some questions related to the reflection of light off the velvet surface compared to the anodized, dark cathode shroud. This will be discussed in the "Image and Data Analysis" Section below.

Sample Images and Reproducibility

Figure 2-5 shows a set of images taken over a span of 3.5 hours to demonstrate the reproducibility of the images. The first two images (a and b) were taken on adjacent shots with a separation of about 1 minute. The next two images (c

and d) were taken on adjacent shots, but approximately 3.5 hours after the first two. Major features of the images remain the same although variation can be seen with individual emission sites. The images were stretched in the horizontal to provide a pseudo front view of the cathode, cropped to delete non-emitting areas, and false colored to enhance contrast. The pixel intensity range was limited to 0-4,000 due to the low level of photons during the short exposure. The effect of pixel saturation (starring) due to radiation was reduced by limiting the intensity range. Equipment parameters including the accelerator and beam were the same for all four images. The Shot Number adjacent to the image can be used to check equipment parameters in Appendix A.

A total of 13 sets of images were taken at the beginning of the experiment (refer to Appendix A) to establish repeatability. Figure 2-6 is a second set of images similar to Figure 2-5 with 10 ns exposures, but with a delay of 220 ns taken over a span of three hours. These images show the increase in brightness of the periphery spots described in other papers[19,20]. As with the earlier delay, these images maintained the major features with some variation in details of individual emission sites.

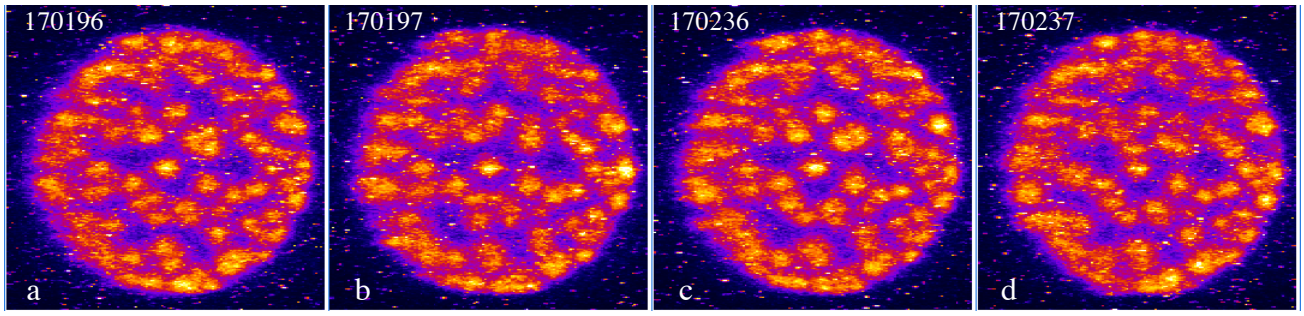

Figure 2-5. Four cathode images taken with a 10 ns exposure and a trigger delay of 170 ns show reproducibility.

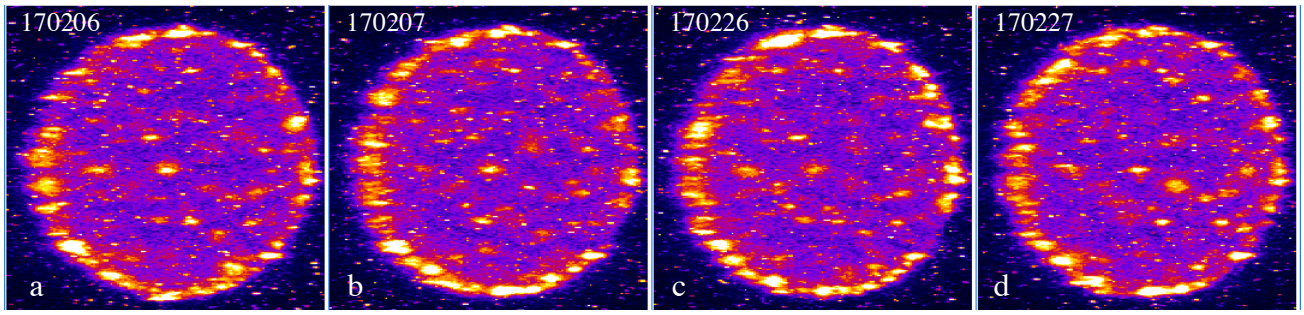

Figure 2-6. Four images taken with 10 ns exposure and a trigger delay of 220 ns to show reproducibility.

Relating Images To Beam Parameters

Establishing an absolute timing between the images and the beam is critical and proved to be more difficult than anticipated. The camera is triggered by a signal generated by the high voltage pulse that is eventually applied to the diode. This trigger system ensures that the relative timing between the diode voltage/beam/camera remains fixed. However, the data acquisition system for the other diagnostics uses a trigger from a different section of the pulsed power system. The time difference between the two triggers in addition to a number of diagnostic cables time lengths were required. Appendix B provides information on how this absolute timing was achieved. The principle beam diagnostics for the injector are a B-Dot array of rf loops located on the vacuum spool around the diode and a resistive wall beam position monitor[21,22] (BPM) at the exit of the injector. Both of these diagnostics have issues that will be described. There is no direct voltage measurement at the diode. The calculated perveance and measured current at the I20 B-Dot diagnostic can be used to estimate the diode voltage. The initial voltage pulse is generated by ten inductive adder cells located along the cathode (6 cells) and anode (4 cells) stalks. The individual pulses can be summed allowing for transit time to produce the expected diode voltage. A voltage resistive divider (VRD) is installed on the anode stalk, but was not calibrated and/or used for this effort. Also, the VRD output would had to have been transit time corrected and summed with the cathode cells.

The BPM issue is related to transport of the beam to the location of the diagnostic. The magnetic transport used in FXR is energy sensitive. Portions of the beam that are “off energy” such as the head and tail of the current pulse will intersect the vacuum wall of the injector and not arrive at the position of the BPM. In fact a section of the anode is

designated as the transition zone, refer to Figure 2-1, and intentionally used to eliminate off-energy current that is not desired. Thus, the current pulse measured at the BPM could be, and normally is, much different than the current from the cathode. Refer to Figure 2-8 below. The BPM signals and beam scrapping in the transition zone will be discussed in more detail in the "Image and Data Analysis" Section.

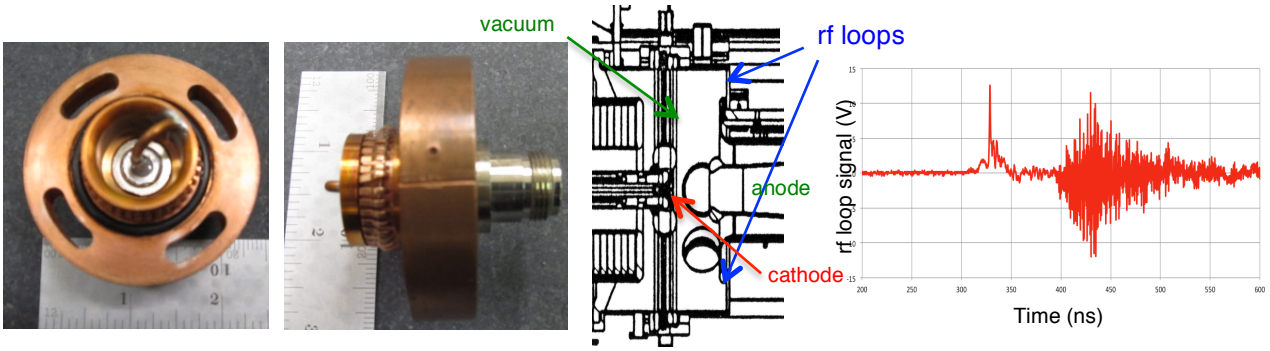

Figure 2-7. Photographs of a rf loop, sketch of vacuum spool identifying position of loops, and raw signal from a loop.

The B-Dot diagnostic has several issues. The four rf loops that comprised the diagnostic are located in the radial walls of the vacuum spool and not the outer wall as is normally the case for B-Dot diagnostics used for beam current and position diagnostics. Refer to Figure 2-7 above. There are many good references[23,24] for B-Dot diagnostics and a simplified description of their operation for our experiment is given in Appendix C. The general shape of the vacuum spool where the rf loops are located presents a problem. The spool behaves as a resonant cavity and is excited by the applied HV pulse and beam. The raw signal of the rf loop shows a distinct ringing towards the end of the current pulse at 900 MHz as seen in the right graph of Figure 2-7 that matches the TM_{120} resonance of a cylindrical cavity of the same outer diameter of the spool. The ringing cancels when integrating the signal to acquire the current. For offset calculations, the ringing normally occurs at the completion of the HV pulse and does not impact the portion of the current pulse that is transmitted to the accelerator. As described in the "Image and Data Analysis" Section there is a correlation between this ringing starting earlier in the pulse and beam transverse instability, often referred to as Beam Breakup[25,26,27,28] (BBU), in the accelerator. A final issue with the location of the rf loops is that the loops are located radially above the anode stalk. Return currents flowing on the stalk redistribute such that the field asymmetry of an off-center beam is significantly reduced. Appendix D provides a detailed analysis of this effect.

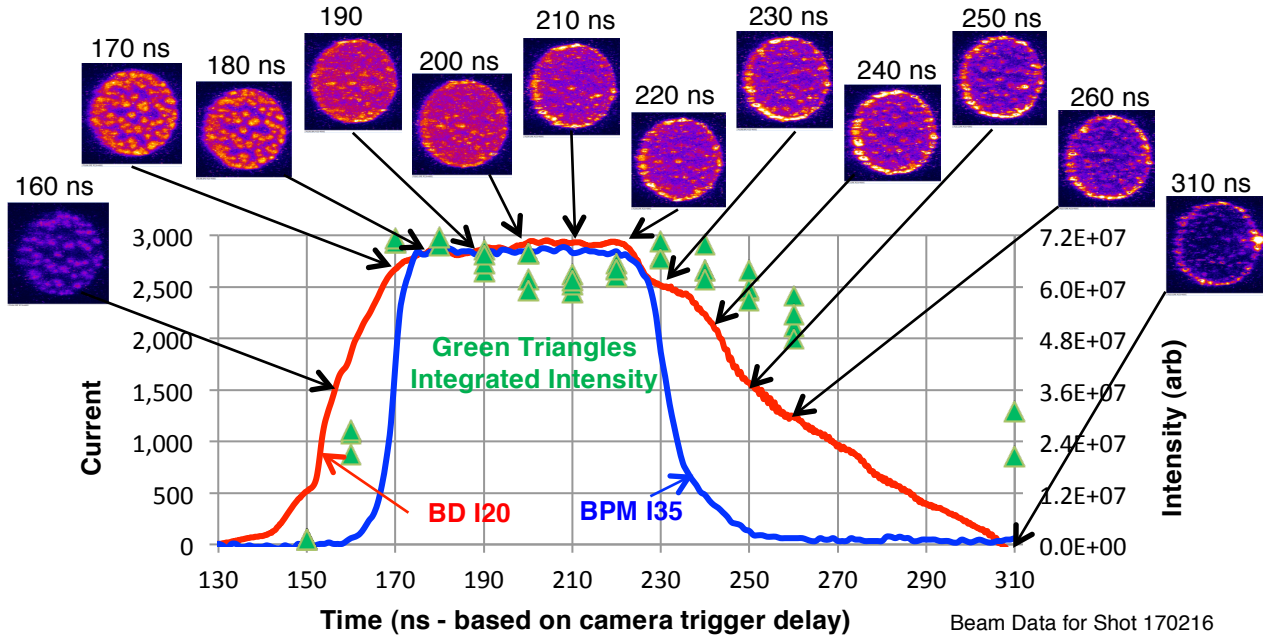

Figure 2-8. Composite picture showing the current pulse as measured at the diode (BD I20), the current pulse measured at the injector exit (BPM I35), cathode images for different exposures during the current pulse, and the integrated intensity of cathode images.

All of the timing information was used to generate Figure 2-8. Timing accuracy between the various signals and images is between 3 ns and 5 ns. A larger version of Figure 2-8 is provided in Appendix B with additional information on the preparation of the data. The images were taken with 10 ns exposures and represent a movie of the cathode light with the caveat that each represents a different HV/current pulse. The importance of reproducibility between pulses cannot be over stressed. The loss of current between the diode and injector exit is readily apparent in the figure. Cathode light at longer delay times will be discussed in the "Image and Data Analysis" Section.

Experimental Plan

The cathode light image data was acquired on three separate accelerator operation days each separated by about one month to allow time for analyzing images and determining needed data. There were also a number of trips to the accelerator facility for software development and equipment checks. The plan for acquiring images evolved as data was acquired and analyzed. However, a few requirements of highest priority did not change: verifying reproducibility and determining cathode light parameters as a function of pulse time. Other measurements such as checking performance with respect to velvet position relative to the cathode shroud, determining absolute timing, and checking current variation between the diode and exit were included in the experimental plan as the need became obvious. Appendix A lists the goals and data taken for the three accelerator operation days. Additional data concerning beam parameters has been added to the daily log.

3 Image and Data Analysis

Onset of Light

The first appearance of light on the cathode is important for relating the phenomena to the applied voltage and emitted current. The onset of light was determined by varying the camera trigger delay in 10 ns increments with a 10 ns exposure and then repeating at 5 ns exposures. The series of images in Figure 3-1 indicates that the light begins sometime between 165 ns and 170 ns trigger delay.

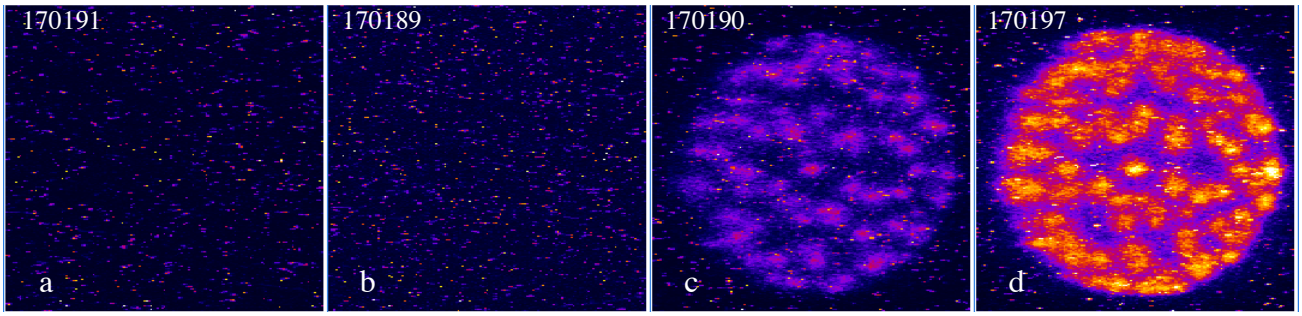

Figure 3-1. Series of cathode images showing onset of light. Left to right: a) 150 ns delay with 10 ns exposure, b) 160 ns delay with 5 ns exposure, c) 160 ns delay with 10 ns exposure, d) and 170 ns delay with 10 ns exposure.

The images in Figure 3-1 have a pixel range of 0 to 4,000 as for earlier images shown in this report so that relative comparison of light intensity may be quickly observed. Subtracting a background and integrating the total number of pixel intensities gives a value for the 10 ns exposure at 160 ns trigger delay of about one third of the value as that of the 10 ns exposure at 170 ns trigger delay. Note that there is no contribution from the first 5 ns of the 160 ns trigger delay exposure. This indicates that the light intensity achieves full value very quickly.

Explosive Emission, Plasma Expansion, and Perveance,

Explosive electron emission for velvet cathodes is described by Miller[29]. Experiments[30] were performed at LLNL in 2006 to characterize the light off of small tuffs of the FXR cathode velvet (1 mm diameter and 1.5 mm in height) as part of a larger study on electrical break down in vacuum. For the parameters used in the experiment, 1-cm electrode spacing and 100 ns rise time to 100 kV, the onset of explosive emission began between 40 kV to 60 kV with a plasma closure rate of approximately 2 cm/μs. These results compare closely with those presented in Miller's work. Using his scaling relationship with plasma closure velocity (Equation 21 of Reference 8) with the FXR diode parameters, 10-cm gap and 2.5 MV, produces a plasma velocity of 2.8 cm/μs.

Several of our images allowed a measurement of the plasma velocity in situ. Figure 3-2 is a series of images for an experiment where the surface of the velvet was moved longitudinally with respect to the plane of the cathode shroud surface. Refer to Appendix D for photographs of the diode with velvet position and more details of the images. One set of images was captured with a 10 ns exposure and a 170 ns trigger delay, essentially at the beginning of the pulse. A second set was captured 50 ns later, i.e. trigger delay of 220 ns. The difference in vertical height of each pair of images was divided by two and then divided by 50 ns to provide an average plasma expansion velocity. This expansion velocity was used for determining an estimated beamlet size as described below.

For the recessed case the velvet surface was nominally 1 mm below the cathode surface and the plasma should be

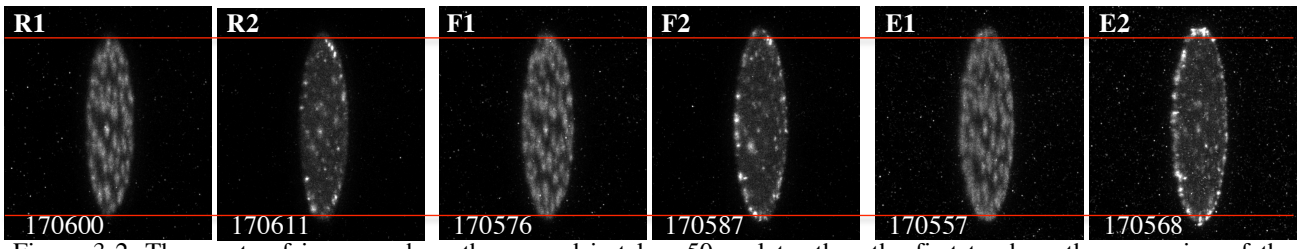

Figure 3-2. Three sets of images where the second is taken 50 ns later than the first to show the expansion of the plasma. The sets from left to right are for recessed (R), flush (F), and extended (E) velvet with respect to the cathode.

constrained by the shroud and limited in transverse expansion. The images indicated an increase in diameter of 0.5 to 1.5 mm or an expansion of 0.5 to 1.5 cm/μs. When the velvet surface was moved to be even with the shroud surface, the diameter increased by 3 mm or an expansion of 3 cm/μs. With the velvet extending about 1 mm beyond the shroud, similar to the early experiment mentioned above, the diameter increased by 2 mm or an expansion of 2 cm/μs.

It is reasonable to expect the plasma to move longitudinally into the A-K gap similar to the transverse motion. This has the effect of decreasing the effective gap. Refer to Appendix E on perveance. At velocities of 2 cm/μs over the 65 ns of the "flat top" portion of the current pulse, the plasma will move about 1.3 mm both radially outward from the edge of the velvet and across the AK gap. Note that the surface of the plasma is the electron emission surface. We can estimate the expected change in current using Equation (D4) in Appendix D and assuming constant voltage:

$$\frac{I_f}{I_i} = \frac{(r+\Delta)^2}{(d-\Delta)^2}\frac{d^2}{r^2} = \frac{\left(1+{}^{\Delta}/_{r}\right)^2}{\left(1-{}^{\Delta}/_{d}\right)^2} \cong 1 + 2\frac{\Delta}{r} + 2\frac{\Delta}{d}, \text{ where}$$

I_f is the final current, I_i is the initial current, Δ is 1.3 mm (plasma movement), r is 29 mm (velvet radius), and d is 77 mm (effective AK gap). The current is expected to increase about 12.5% over the pulse if the voltage is held constant. It does not seem possible to have both a "flat top" current and a "flat top" voltage pulse from the injector.

General Image Characteristics, Emission Spots, Beamlet Size, and Reproducibility

The cathode images are comprised of bright spots on a pedestal. Refer to images in Figure 3-3 that were taken with 10 ns exposures and with trigger delays of 170 ns and 210 ns, respectively. The maximum range of the pixel intensity has been limited to 4,000 counts. There are several interesting features of the image intensities. Outside of the velvet area the intensity is low except for noise spikes and starring due to background gamma radiation noise. Over the velvet there is a larger background or pedestal, about 1,000 counts, that exists between the bright spots. Refer to the vertical and horizontal lineouts presented in Figure 3-4. Except for the edges of the velvet, the earlier, i.e. shorter trigger delay, images tend to have higher intensity spots.

These observations lead to a number of questions starting with the reproducibility of the pattern of spots. The following is conjecture, but follows the thoughts of others. The bright spots are assumed to be points of explosive emission on the velvet surface and indicate conduction paths of electrons from the metallic base through the tape and then through the velvet. The FXR velvet has a non-conducting tape backing. Saveliev[31] has shown that the bright spots (emission centers) are related to current conduction paths. A plausible explanation for the consistent pattern of spots is that during initial operations with a new cathode, channels are burned into the tape backing that become preferred conduction paths. However, there is some scatter in the location of the emission spots. The cloth backing of the velvet is comprised of many small openings, basically the spacing between threads. The channels in the tape determine the general location of spots while a stochastic mechanism based on local velvet conditions and space charge contributed electric fields controls the current flow through the cloth backing and specific emission locations upon the underlying channels.

The previous FXR cathode used a 10.7-cm diameter velvet that required two parallel strips of tape to secure to the stainless steel base. For one mounting, there was a small gap between the two strips of tape that provided a conduction path. Figure 3-5 contains a series of images for this velvet that show a bright line associated with the gap. If the spots are associated with conductions paths burned into the tape, they should be fixed after a short "burn in" period and cause a reproducible pattern similar to the tape gap. The pattern of spots is highly reproducible as shown in Figures 2-5 and 2-6. Figure 3-6 demonstrates that the pattern persists over a month and hundreds of HV pulses. In Figure 3-6 the images were taken at the beginning of the pulse where the bright, emission spots were most pronounce. Figure 3-7 demonstrates that the interior spots remain even in the tail of the HV pulse, although new and/or more intense spots form on the edge.

The size and distribution of spots is of interest. Krasik[32] was able to produce cathode images consisting of many small spots with a more uniform distribution than FXR's by using velvet glued with a conductive-silver-loaded epoxy to an aluminum base. The pattern was no longer uniform when a mylar film was inserted between the velvet and aluminum. Saveliev[33] was able to produce specific emission spot patterns by establishing conduction paths for the velvet. Figure 3-8 is taken from Saveliev and shows three forced patterns and an unforced random distribution. Velvet placed directly on a conductive surface produces a high concentration of emission spots. The tape used by FXR is not a perfectly uniform insulator and exhibits a random pattern of non-insulating spots, or very thin areas that can be electrically penetrated leaving burned-in conducting channels. The number of emission spots may be related to how fast the electric field stress is applied to the cathode. The new, smaller cathode requires a faster rise in the electric field and has smaller spots than the old cathode (see Figure 1-1). A rough approximation of the diameter of an emission spot is:

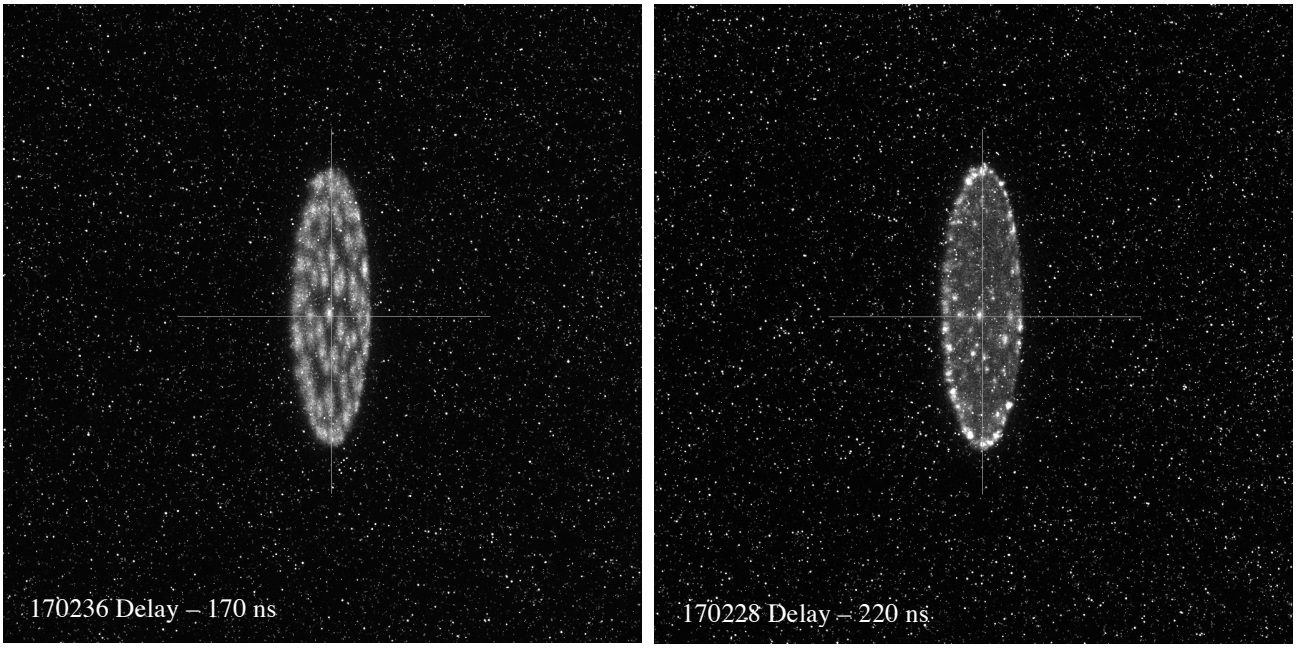

Figure 3-3. Images were taken with 10 ns exposure, left 170 ns delay and right 210 ns delay. (Range 1-4,000)

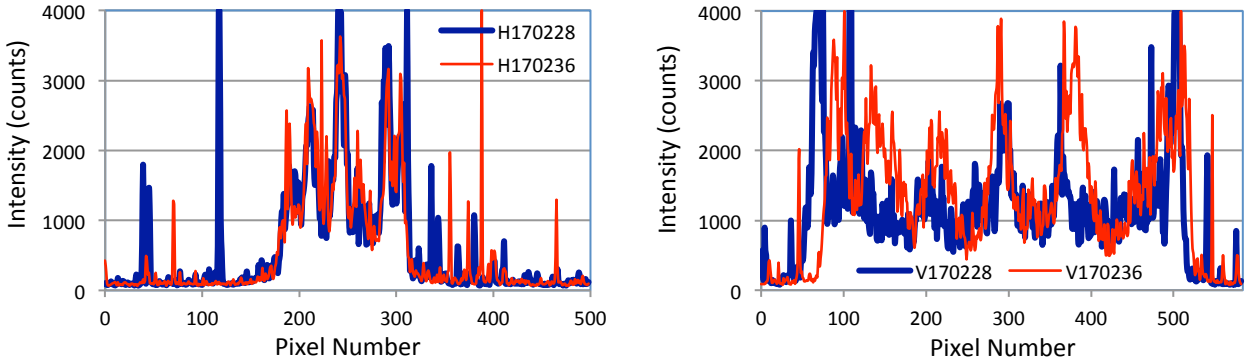

Figure 3-4. Intensity profiles along the horizontal/vertical lines indicated in the Figure 3-3 images.

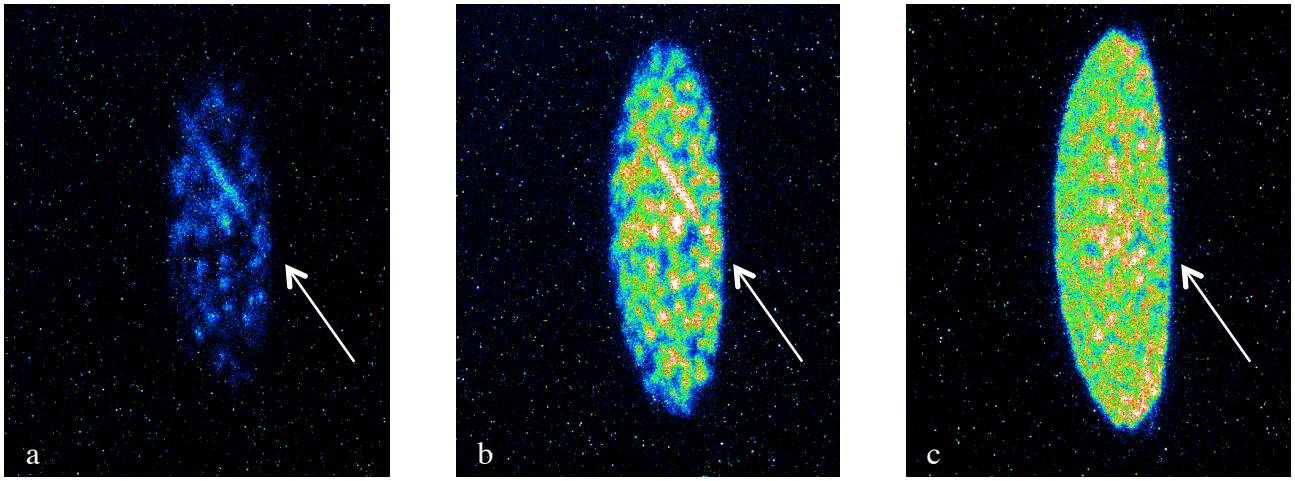

Figure 3-5. FXR old cathode images taken with 10 ns exposure and with 10 ns increments in trigger delay. The arrow indicates the gap between the two strips of backing tape used to secure the velvet to the metallic base.

1. A single velvet tuff is about 1 mm in diameter
2. plasma expansion rate is ~3 mm per 100 ns and it takes about 25 ns from light off to flat top current = 1.25 mm
3. the spot/beamlet above the plasma doubles in size from space charge and geometry, refer to Section 4
4. Final tally is (1 + 1.25)x200% = 4.5 mm

If emission spots begin to form closer than this diameter, the emission of one spot will dominate. The total maximum number of spots is the cathode area divided by spot area, $(28.5/2.5)^2$ or 130 5 mm diameter. If the diameter is taken to be 4 mm the maximum number is 210 spots and for a 6 mm diameter the maximum is 90 spots. These numbers are upper limits as the spots do not fit together perfectly. In Section 5 "Automated Image Analysis", the FXR images were found to have about 100 bright spots, although there were some obvious gaps between spots.

The higher background of the pedestal, the dimming of the emission spots during the HV pulse, and the increase intensity of the edge are difficult to explain. The abrupt drop of intensity moving from the velvet to the black anodized shroud has led to speculation that there is light reflected off of the velvet. Switching to a matte black velvet would determine if reflected light is a contributor. Another mechanism would be light from the emission spots scattering on the plasma. As the plasma expanded longitudinally, the light from the emission spots would undergo numerous scatterings producing a more uniform distribution that masks the initial light source. This explanation is consistent with the information shown in Figure 2-8 where the integrated intensity remained reasonably constant while the individual interior spots grew dimmer. The edge emission spot brightness could be similarly explained by noting that light from the velvet periphery would not undergo as much scattering.

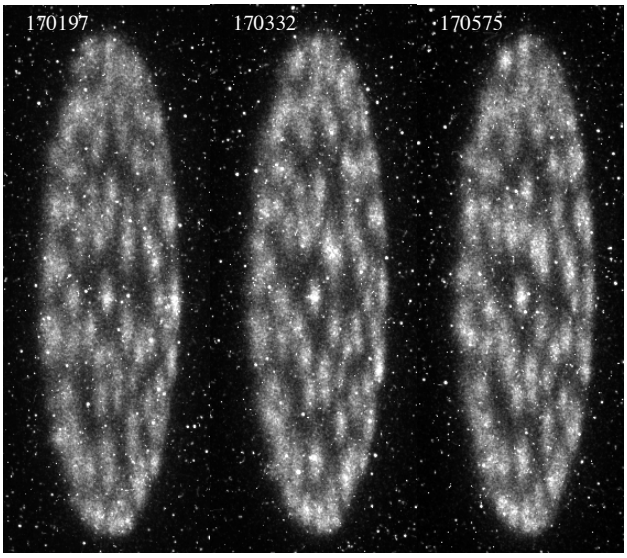

Figure 3-6. Images were taken under same operational parameters on 1/31/12, 2/8/12, and 3/1/12 respectively.

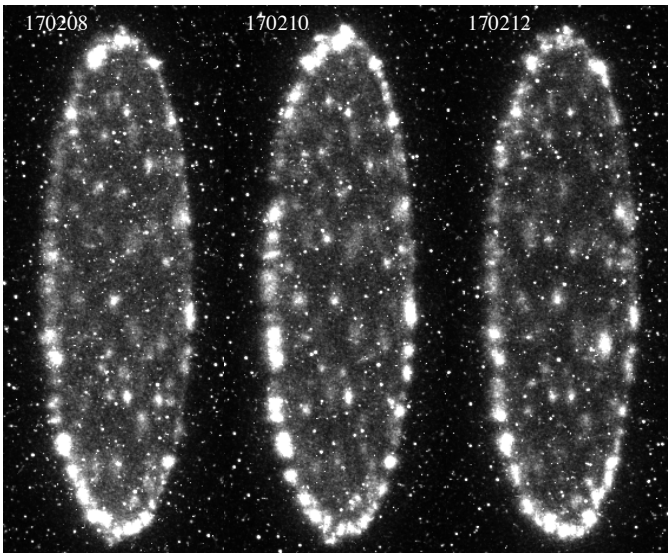

Figure 3-7. Images taken with delays of 230, 240, and 250 ns respectively, but under same operational parameters,

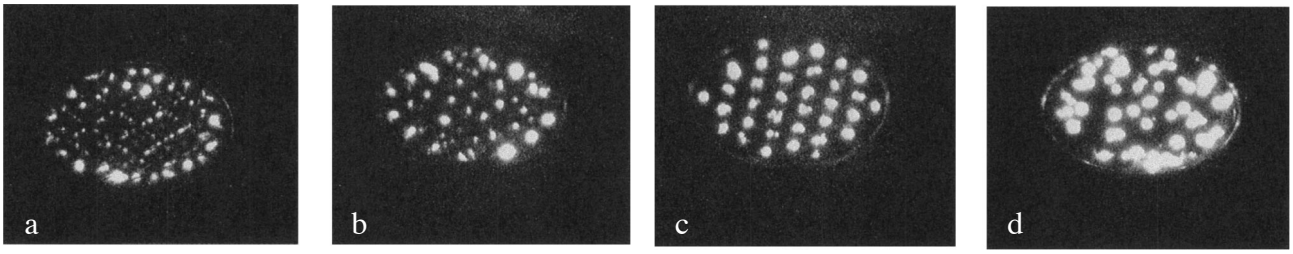

Figure 3-8. Images are from Saveliev, JAP 94 2003: Velvet cathode with (a) grid of thin wires buried at roots of velvet fibers, (b) velvet fabric stretched over pattern of metal needles, (c) metal perforated mask, and d) a carbon fiber cathode.

Velvet Position Impact on Emittance, Current Transport, and BBU

Studying the effect of moving the velvet surface with respect to the plane of the cathode shroud was motivated by the observation that the transverse stability of the beam (Beam Breakup or BBU) could be improved by extending the velvet beyond the shroud. The start of the 900 MHz ringing on the B-Dot diagnostic occurs earlier when BBU is noted

on the beam as shown in Figure 3-9. Both of these phenomena are associated with off-axis beams. An off-axis beam excites the transverse resonances of the diode vacuum spool that are detected by the B-dot. Similarly, an off-axis beam passing through an accelerator cavity excites the transverse resonances of the cavity leading to growth of the BBU instability. Thus, there was a conjecture that the image would indicate a distribution change in light that correlated with the B-Dot signal and BBU. In addition, the emittance of the beam is changed by the velvet/shroud position and edge effects.

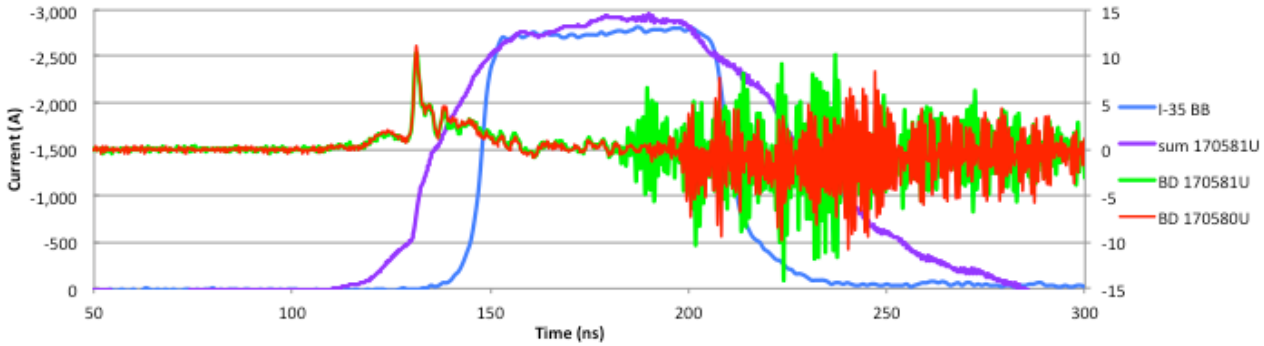

Figure 3-9. Plot of raw B-Dot signals for two shots, 170580 no BBU and 170581 high BBU, overlaid on current pulse.

There is more BBU motion as the velvet is retracted. The graph in Figure 3-10 shows the BBU signal strength as calculated by the BBU Tool[34] at the end of the accelerator (L44) for the shot series taken on 1 March 2012 at different velvet positions. "Extend" refers to the nominal position of the velvet for this study that is ~1 mm beyond the face of the cathode shroud, "Flush" is when the velvet was retracted about 1 mm and is nominally flush with the surface of the cathode, and "Recessed" is when the velvet was retracted another mm below the surface of the shroud. Refer to Appendix D for photographs of the diode/cathode for the different positions. The average value for the BBU signal strength was 0.29, 0.69 (0.5 without the one outlier), and 0.95 for the "Extend", "Flush", and "Recessed" cases, respectively.

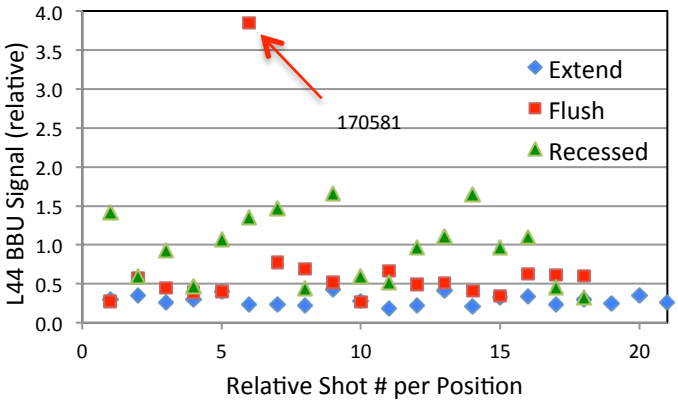

Figure 3-10. Relative strength of BBU instability is shown for various positions of velvet with respect to the cathode.

There was a significant change in the current transported through the injector for the three velvet positions. The two graphs in Figure 3-11 show the current at the diode, I-20 B-Dot, and at the end of the injector, I-35 BPM, for the three shot series. Emitted current from computer simulations is included for comparison. The current for the I-20 B-Dot does not have an absolute calibration, but the relative changes should be accurate. The first eleven shots on the "Extend" I-20 are not shown as they were with a different diagnostic line configuration and have a different calibration than the remaining shots. Table 1 list the change in current as the velvet was moved. From the previous discussion on changing perveance, the current changes were expected to be about 10% for each shift of the velvet. Determining the appropriate current change is complicated due to larger effective diameter and emission from the sides when the velvet is extended. The "Flush" position going to the "Recessed" position is closer to the situation discussed in the previous section, but the shielding of the electric field by the edge of the shroud opening would lead to a larger drop in emission. Altogether, the results for I-20 B-Dot measurements seem reasonable.

The small drop in current at I-35 going from the "Extend" to "Flush" position suggests that the beam diameter in the "Extend" case starts larger and about 10% of the current on the outer diameter of the beam is lost (scrapped off) during transport. With the "Flush" and "Recessed" cases the beam is a smaller diameter and much less of the current is lost in the injector. To confirm this hypothesis a set of simulations were performed. Refer to the next Section, "Computer Simulations". The simulations supported the hypothesis and showed that for the "Extend" position several hundred amperes were lost within 35 cm of the cathode in the entrance of the anode stalk. Current lost in that area would produce a noticeable amount of radiation near the camera that should increase the "starring" on the image. The cathode images shown in Figure 3-12 do in fact show this increased starring as the velvet is extended. Some of the increase could be due

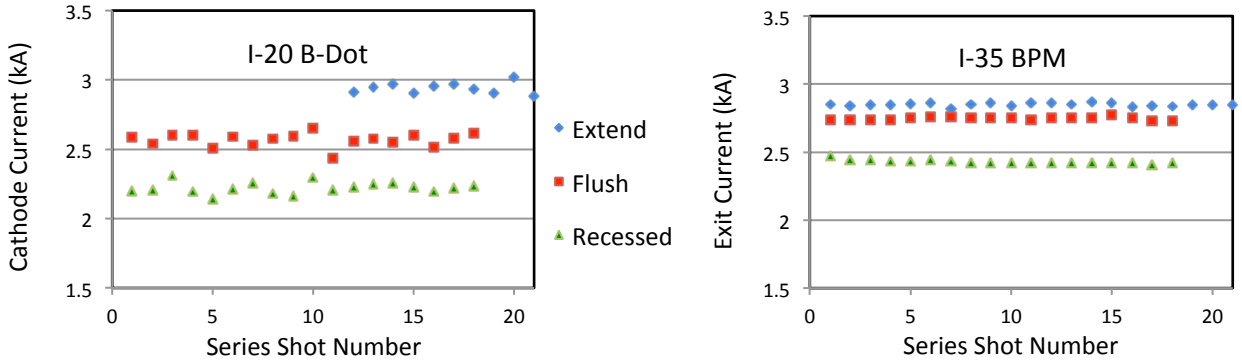

Figure 3-11. Graphs of the beam current are shown at the cathode and exit of the injector for the three velvet positions.

to the higher beam current. However, by checking the standard deviation (σ) of pixel intensity in a section of the images away from the velvet, that is, looking at the background, a relative measurement of the starring can be made. Normally, for an ideal background, σ would be zero. The large value of the starred pixels causes σ to increase. For the images in Figure 20 σ is 191 (268), 305 (366), and 514, respectively where the bracketed number is adjusted for current. Extending the velvet does generate significantly more beam loss in the entrance of the anode stalk.

Table 1. Average Current and Change from previous case

Case	Simulation Emitted (kA)	% Change	Cathode B-Dot I-20 (kA)	% Change	Exit BPM I-35 (kA)	% Change
Extend	3.812	---	2.945	---	2.849	---
Flush	3.117	-18%	2.569	-13%	2.747	-4%
Recessed	2.712	-13%	2.221	-14%	2.427	-12%

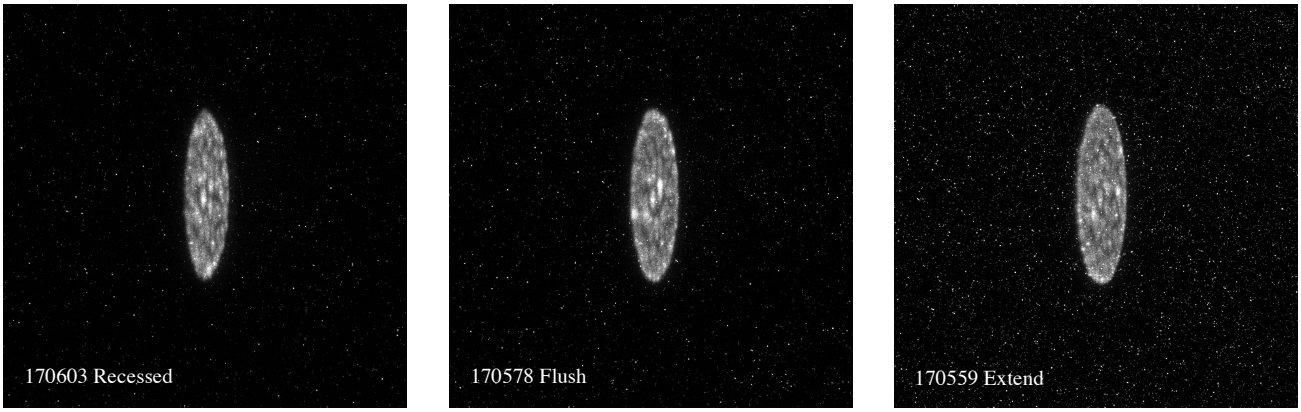

Figure 3-12. Shown is a series of images as the velvet is moved outward from a 1 mm recess to a flush position then extended with respect to the cathode shroud. Increased "starring" of the image is noted as the velvet is extended.

Explaining the decrease in the BBU strength with extension of the velvet is speculative. The BBU grows linearly with the initial frequency component, ξ_o, and exponentially with the current. Holding accelerator and magnet parameters constant, the BBU growth can be expressed as[35]:

$$\xi = \xi_0 e^{\alpha z}, \text{ where}$$

z is the longitudinal distance, α is a parameter that depends on the impedance of the accelerator cells, number of cells, beam energy, beam current, and focusing magnetic field strength, and ξ_o is the Fourier component of the initial beam transverse motion at the BBU resonant frequency. Often times the initial motion is simply due to an offset of the beam axis with respect to the accelerator axis. If the beam has a uniform cross-sectional current distribution with an offset from the axis and is passed through a smaller diameter, on-axis aperture, the resulting beam would have a smaller diameter, less current, and no offset.

Thus, a probable mechanism for the decrease in BBU as the velvet cathode is extended is a change in beam diameter. Simulations and beam loss data support this hypothesis. The beam is not aligned with the mechanical center of the anode either due to misalignment of the velvet cathode or an asymmetry of the emitted current distribution across the

velvet. With the velvet in the Extend position the beam diameter is larger than the interior diameter of the anode stalk and offsets in the beam centroid position, either constant or time variable, are not transported. Simulations (refer to Section 4) indicate that the emittance of the beam transported through the anode is increased as the velvet is extended. However, the image FOM defined in Section 4 was actually slightly better for the extended case (refer to Section 5).

Cathode images for Shots 170579, 80, 82, 83 (no BBU) and 170581 (the 3.8 outlier in Figure 3-10) taken with identical camera and velvet conditions are shown in Figure 3-13. The large disparity in BBU signal shown for shot 170581 led to the thought that the cathode image would show an anomaly. There is a noticeable "hot" spot near the bottom of the 170581 image, but in general the images are not significant different in appearance. All images were taken with 10 ns exposures and similar trigger delays (delays are annotated on the images). This may be first solid indication that the beam centroid will change depending on how the velvet lights off and that it can be noticed in a cathode image. However, neither the relative displacement measured by the I-20 B-Dot or from the image analysis (see Section 5), indicated a significant change so the phenomena causing the BBU may have occurred downstream of the diode.

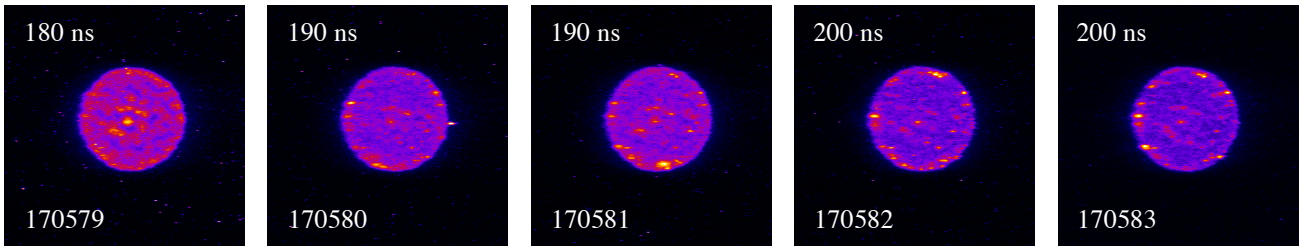

Figure 3-13. A series of cathode images taken with 10 ns exposures are shown to illustrate lack of significant change when the emitted beam shows increased transverse instability (BBU). Camera trigger delays are annotated on the images. The center image (170581) is the only image associated with an abnormally high BBU signal.

Edge Effects and Arcs

The decision was made to not use a Pierce[36] style shroud for the new cathode design. The face of the shroud is flat and the edge of the opening for the velvet is relatively sharp with only a nominal radius (break or chamfer of 0.5 mm). The shroud is fabricated from aluminum (6061-T651) with an 8 micro-inch polish and a Hard Clear Anodize per MIL-A-8625-E Type III Class I (0.0005 inch to 0.0015 inch thick) finish. This design brings up two issues related to edge effects related to the interface between the velvet and the cathode shroud. The first is related to beam dynamics and the electric field in the vicinity of the edge. The Pierce method involves finding a self-consistent solution for a space-charge dominated injector by calculating the shapes of the accelerating electrodes to produce a laminar beam with uniform current density. Basically the electrodes are shaped so that in the steady state solution the radial space charge field is balanced by the radial component of the applied electrical field. The total field, space charge and applied, is uniform and perpendicular to the emission surface at all radii including the edge. In practice, a perfect Pierce design is difficult to achieve and will be true for a single applied voltage and emitted current. In Section 4 "Computer Simulations", the effect of the edge on the electron orbits is illustrated. The new design intended for the velvet to be flush with the face of the cathode shroud. For the high field stress and high diode voltage used in the FXR diode, the Pierce geometry did not have a significant impact on the beam emittance assuming the emission surface is flush with the shroud.

The effect of direct emission from the cathode shroud is of greater concern. The new cathode design maintained nearly the same maximum field stress on the shroud, 280 kV/cm new compared with 250 kV/cm old. Although higher, the new design was still considered conservative for the hard anodized, polished aluminum surface. The concern was

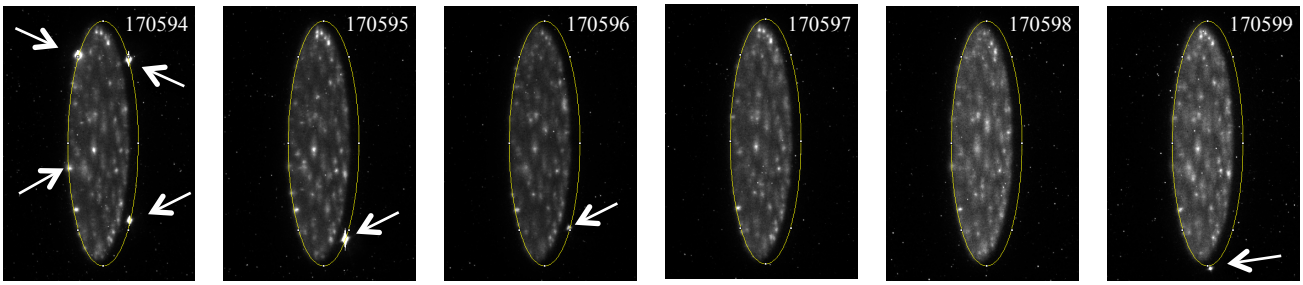

Figure 3-14. The images shown are a consecutive series for the recessed velvet case from the initial pulse for this case until no more edge emission was observed.

enhanced field stress on the edge of the shroud if the velvet was recessed. Figure 3-14 shows images of the first six pulses after the cathode was retracted to the Recessed position. The yellow outline indicates the location of the shroud edge and the arrows indicate explosive emission sites. Note that the orientation is such that the left edge of the plasma light in the image is nearest the camera so only the top of the shroud edge is seen. Moving to the right on the image is looking across the velvet and viewing the inner lip of the far edge. The remaining 12 images in the series did not show any explosive emission sites on the shroud edge. The recessed velvet series of images indicates that conditioning and/or burning off stray pieces of material from the cathode shroud will occur and explosive emissions from the edge is not an issue. Infrequently a image will indicate shroud emission. For instance in Figure 3-13 the second from left image (Shot Number 170580) shows an emission site on the shroud near the velvet. The cathode camera is an outstanding diagnostic for identifying contamination or surface damage to the shroud.

Late Time Cathode Images

Cathode images with 100 ns exposures were taken at times over a microsecond after the voltage pulse. These images were not directly related to the study of beam quality, but provide information regarding a couple of issues of future interest. The first issue regards the source of the light and characteristics of the explosively emitted plasma. Figure 3-15 is a series of 100 ns exposure images from the start of the voltage pulse until about 500 ns after the pulse with the associated current pulse. The fourth image from the left, #170275 with a 450 ns delay, exhibits a noticeable brightening in the center of the velvet. The brightening feature is repeatable and could be due to the density of the expanding plasma dropping below a threshold value for visible light propagation. Double pulse experiments[37] with a velvet cathode performed at LLNL's Advanced Test Accelerator (ATA) noted a decrease in the plasma expansion into the diode gap after 400 ns as measured by changing perveance. While beyond the scope of this study, these two phenomena provide a rich source of information for further studies.

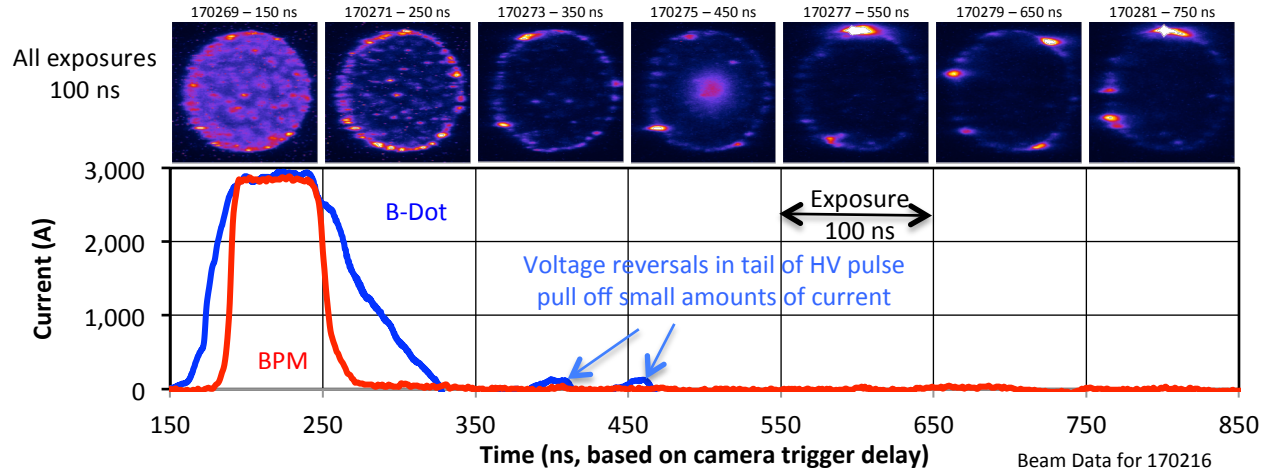

Figure 3-15. Composite picture showing the current pulse as measured at the diode (I20 B-Dot), the current pulsed measured at the injector exit, and cathode images for different exposures during the current pulse.

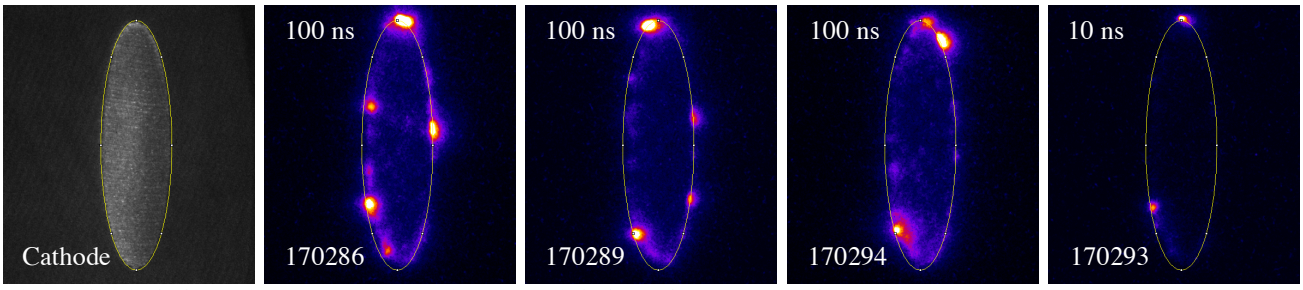

Figure 3-16. A front-lit cathode picture is on the left for reference. The following cathode images are representative images for a 1,150 ns trigger delay and exposure times as noted. Yellow outline is positioned the same for each image.

The second issue is double pulsing the cathode. Figure 3-16 shows that plasma activity is occurring a microsecond after the pulse. The dynamic range for these images has been reduced by a factor of 3 compared to Figure 3-15 to allow the blue glow over the velvet surface to be seen. It is not known how the existing plasma will affect a second pulse.

4 Computer Simulations

Operating a large accelerator is expensive and challenging to schedule. FXR is no exception. Changing the physical configuration to explore the effect of different parameters must allow for the accelerator to be returned to the nominal standard performance at completion. In addition some aspects of accelerator performance and beam quality are difficult to measure. Beam emittance and size can only be measured at discreet locations. Studying the performance of multiple cathode materials and configurations can be prohibitively expensive because the accelerator needs to be brought to air and the cathode disassembled for each installation. Computer simulations allow a broad variety of configurations to be studied quickly and with total knowledge of beam parameters. The simulations presented were performed with the *Advanced Charge-particle Design Suite* from Field Precision[38].

Cathode Position With Respect To Shroud Plane

Moving the velvet surface with respect to the plane of the cathode shroud has a large effect on the beam both at the cathode and at the exit from the injector. The two diagnostics available for measuring the total current and position of the beam, B-Dot and BPM, indicated that changes were occurring to the beam during transport through the anode. To gain a better understanding of the beam dynamics involved, a series of two-dimensional (R-Z) simulations of the FXR injector was performed. Refer to Figure 4-1. In the figure, the electron orbits are grey and at the shown resolution merge into a solid. The multi color background is filled contours of an equipotential plot that includes the applied field (-1.5 MV on the cathode and +1.0 MV on the anode) and space charge of the electrons. The simulated beam was found to have a larger radius in the first 2 meters of the anode stalk for the same magnetic transport as the velvet was moved outward. This larger radius led to beam scrapping in the early portion of the anode stalk and the loss of several hundred amperes of current. For the Extend and Flush cases, the orbits passed very close to, but did not intercept, the anode stalk at the transition to the narrower diameter.

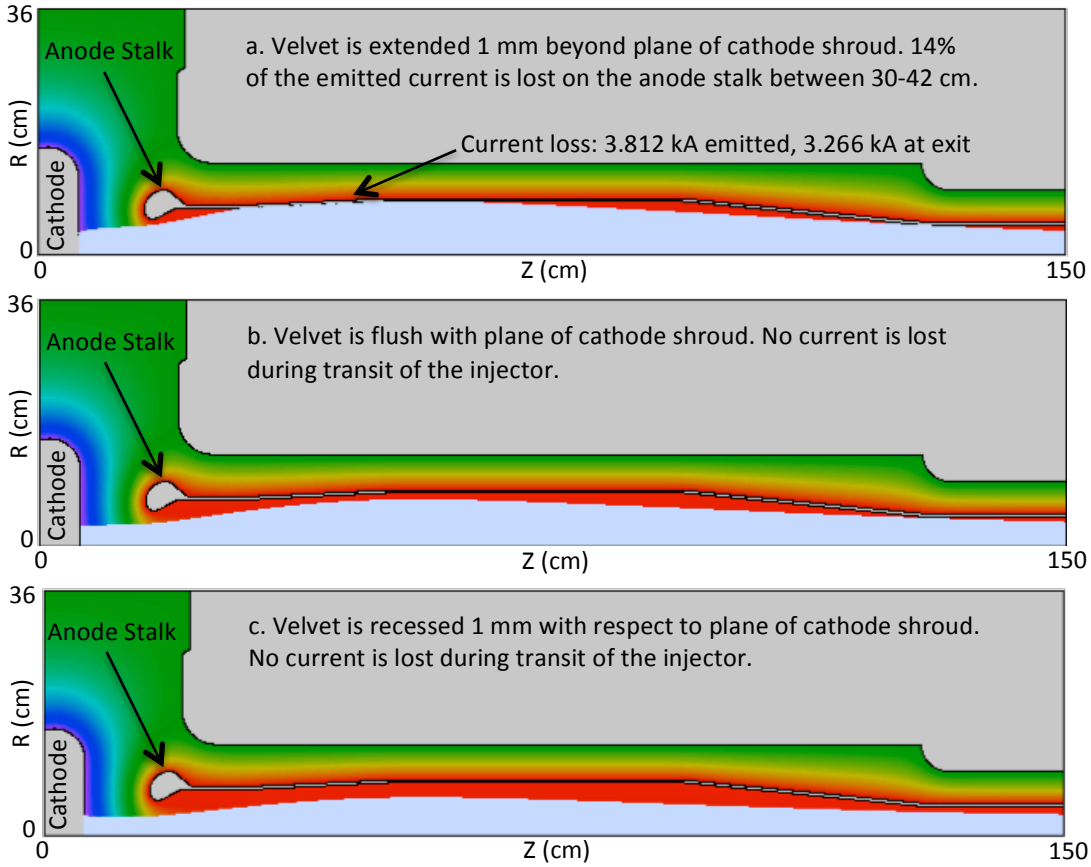

Figure 4-1. Shown are the results of R-Z simulations of the FXR Injector for the three velvet positions.

The primary cause for the larger diameter is edge effects between the velvet and shroud. Close up simulation plots of the cathode are shown in Figure 4-2. Child law or space-charge-limited emission is used to create model particles on the emission surface. Details of the numerical technique used can be found elsewhere[39]. A brief description of the technique is:

1. A set of emission facets and particle initiation points are generated based on the grid and requested number of particles per segment (multiple particles can be created per segment to improve statistics).
2. However, a numerical orbit calculation would not be possible if particles were created on the emission surface. The Child condition of zero electric field implies that zero-energy particles would not move, and the calculation would stall.
3. To resolve the impasse, a generation surface is created by projecting the particle initiation points a given distance, normally about 1.5 times the grid size, from the emission surface. Analytic formulas for space-charge limited flow in a planar gap of the specified width are employed to find the appropriate current and kinetic energy to assign to model particles at the generation surface. In the plots, the orbits can be seen starting at the generation surface located above the emission surface.
4. A novel backtracking technique is employed to ensure correct assignment of space charge in the volume between the emission and generation surfaces.
5. The simulation solves the problem iteratively by assigning current and kinetic energy to model particles at the generation surface based on present values of the local electric field. The orbits are reverse-tracked at fixed energy to the emission surface. Then the orbits are forward-tracked and Poisson equation is solved.

For the simulations shown, a 0.5mm by 0.5 mm mesh was used over the region including the emission and generation surfaces.

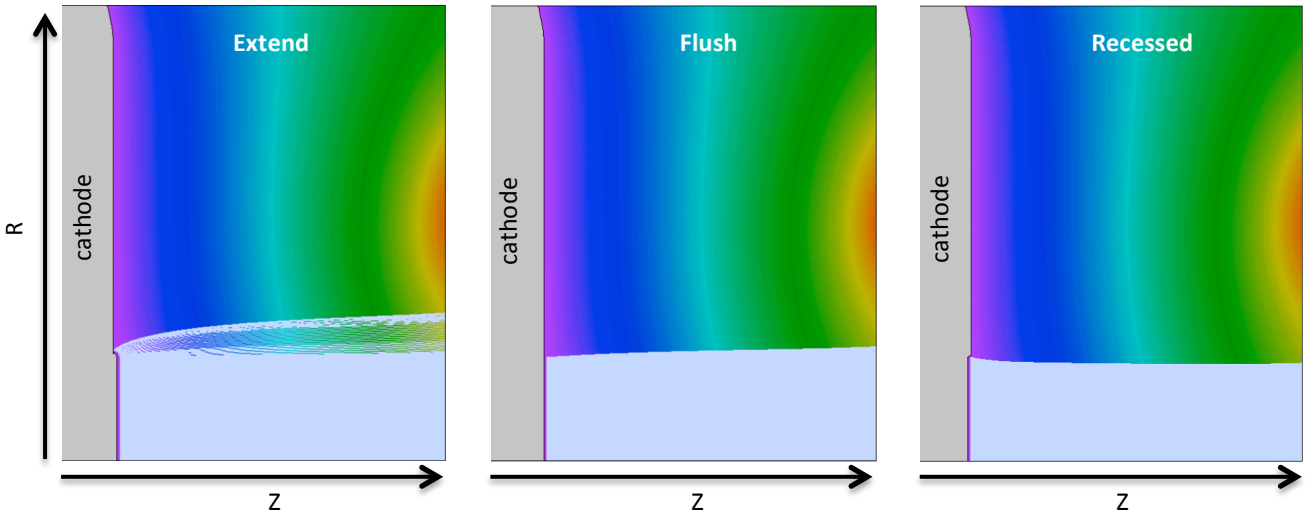

Figure 4-2. The emission/generation surfaces and electron orbits are shown in close up views of the cathode. The plots are filled contour equipotentials varying from -150 kV (purple) to +100 kV (red)

Edge effects have been studied[40] and are known to affect the emittance of the beam. The emittance for each of the three cases is shown in Figure 4-3. Current should also be considered when looking at the emittance values. The current increases as the velvet is extended. Refer to Figure 19 and Table 1 for measured and calculated current values. A rough scaling is that emittance increases as the square root of current. After the current loss for the Extend case, the current difference is not a large effect accounting for about 2 % of the emittance variation between the Extend-Flush and 10% for the Extend-Recessed.

3-D Simulations of Spotty Emission

Simulating sporty emission is inherently 3-dimensional. This presents a number of challenges involving the memory management for the large number of nodes. A technique employed to make the problem more tractable was to solve for the applied electric field on a coarse mesh (5-mm x 5-mm x 5-mm cubes) covering a large volume. The solution for this coarse mesh problem was used as part of the boundary condition for a finer mesh (2-mm x 2-mm x 2-mm cubes), smaller geometry simulation. Refer to Figure 4.4 for a description of the geometries. Once a sufficiently fine mesh was established, the emission surface needed to be defined. Images of the FXR cathode showed many, on the order

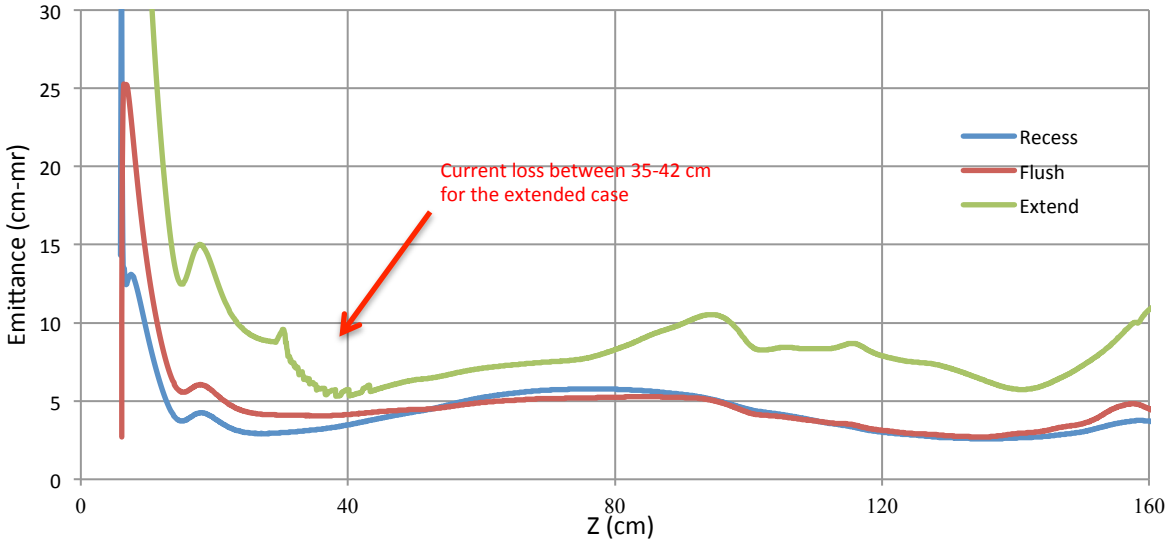

Figure 4-3. Emittance is plotted as a function of longitudinal distance for the three velvet positions

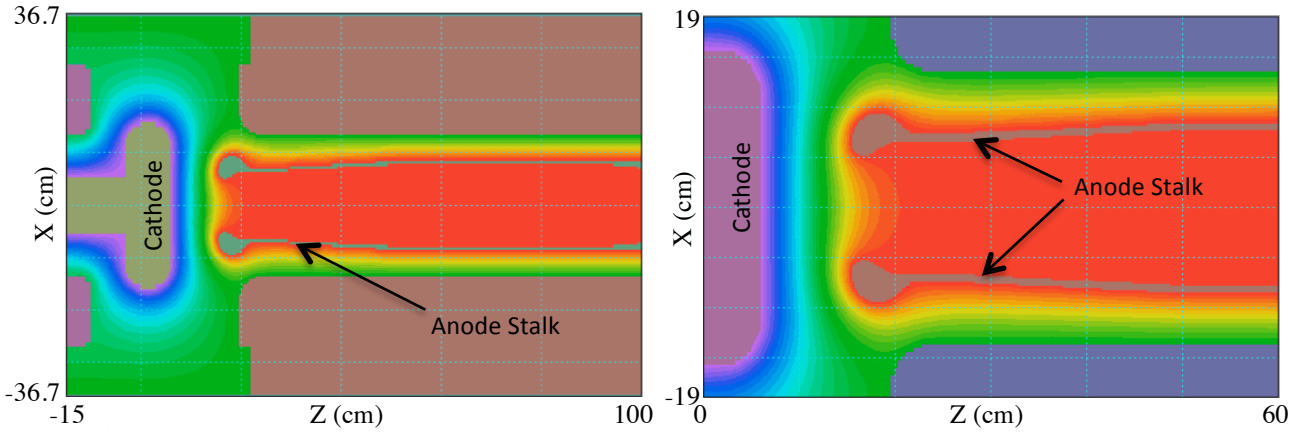

Figure 4-4. Slice plots of simulated geometry (Y = 0) are shown for the initial coarse grid (left) and fine grid (right).

of 100, small emission sites where any one site was about 5 mm in diameter. 100 five-mm spots exceeded the achievable mesh resolution and the number of allowed emission sites in the code. As a compromise, a pattern of as many as 24 12-mm diameter circles located within a 6.6 cm diameter was used to simulate the emission area. Figure 4.5 illustrates a uniform base emission surface and a 22 spot emission surface. A complete listing with surface depictions of the different simulated surfaces is given in Appendix F. An illustration of one of the simulations is shown in Figure 4-5. The simulations include self-consistent effects of beam-generated electric and magnetic fields. Electron emission is from Child-law emission surfaces as described above. The only difference between these simulations and the ones performed for the variation with velvet position is that axial symmetry is not assumed or required.

Two issues when comparing the various emission patterns are the emittance variation as a function of axial position and the differences in current with emission area. For this study the emissions spots are flush with respect to the cathode shroud. As indicated in Figure 4-3 and 4-6, the emittance is reasonably stable, but could change as much as a factor of two depending on where it is measured along the axis. An approach to this problem was to look at where beam was at a waist both by looking at the radius as a function of longitudinal position and the phase space (See Figure 4-7). For all cases a waist occurred near 55 cm and the emittances listed in Table 4.1 were determined at that location.

The current also varied due to the difference in emission area and relative location of emission spots as shown in Table 4.1. The Envelope Equation[41] or Paraxial Equation[42] can be used to indicate that emittance should vary as the root of current. Paraxial equation assuming energy and radius are constant:

$$\frac{d^2R}{dz^2} = -\left[\frac{eB_z(0,z)}{2\gamma\beta m_o c}\right]^2 + \frac{\epsilon^2}{R^3} + \frac{eI}{2\pi R\varepsilon_o m_o(\gamma\beta c)^3}, \tag{4-1}$$

where R is the beam radius, z is the longitudinal position, $B_z(0,z)$ is the on axis solenoidal magnetic field at z, ϵ is the emittance, I is the current, and the remaining terms are standard physical constants. For the beam parameters in the FXR

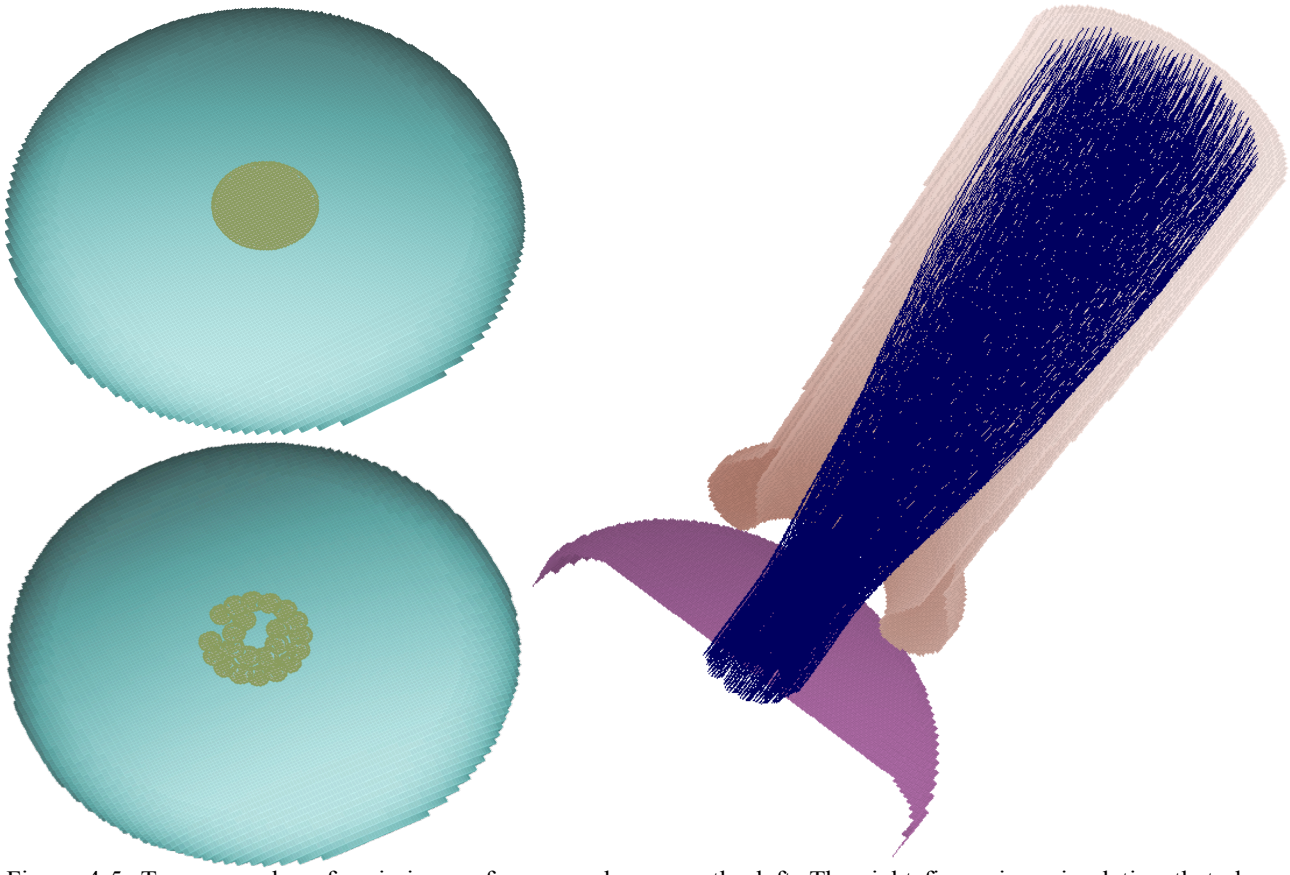

Figure 4-5. Two examples of emission surfaces are shown on the left. The right figure is a simulation that shows electron orbits from the emission surface entering the anode stalk (cut view of the cathode/anode to better show orbits).

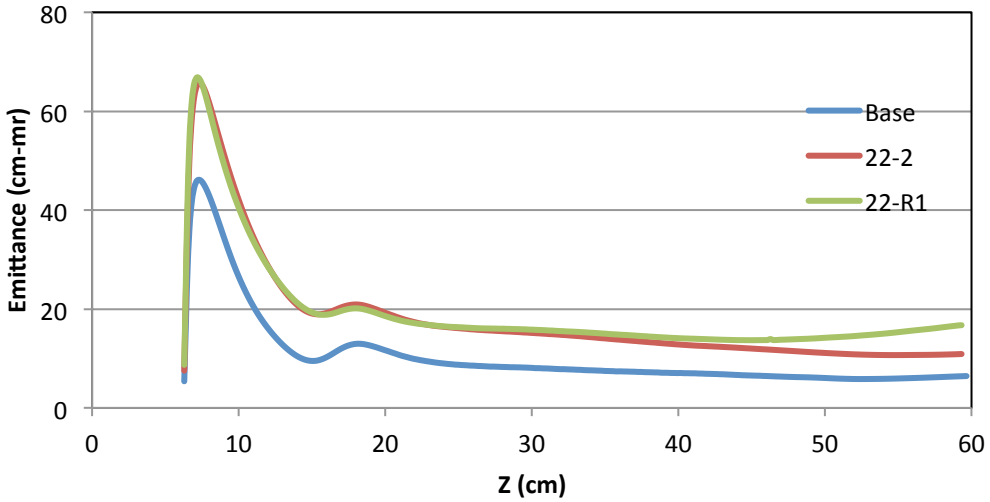

Figure 4-6 Emittance is shown as a function of longitudinal position for three emission surface cases.

injector the beam is space charge dominated. The emittance contribution in Equation 4-1 is small compared to the other terms. However, the magnetic field is kept constant and assuming that d^2R/dz^2 is also constant, we can make a rough approximation that the emittance varies as the square root of the current. In Table 4.1 the column labeled "Scaled Emittance" is the calculated emittance times the square root of the ratio of the base case current divided by the calculated current. While this is a crude adjustment for the variation in current, the effect is small as the standard deviation from the average current of 3.3 kA was less than 4% and the adjustment to emittance less than 2%.

Table 4.1 Parameters and calculated values for different cases of spotty emission.

Case #	Scaled Emittance	Emittance	Area (cm^2)	Current (kA)	# spots	Stdev
Base	6.0	6.0	29.23	3.396	25	0.484
24-A1	7.5	7.6	29.34	3.450	24	0.484
24-0	7.9	8.0	29.17	3.488	24	0.484
24-A2	8.4	8.5	30.16	3.442	24	0.484
23-7	8.6	8.6	27.05	3.396	23	0.492
23-10	9.4	9.4	27.46	3.385	23	0.492
23-R3	9.8	9.7	26.27	3.333	23	0.492
24-R1	9.9	9.8	25.13	3.312	24	0.588
22-2	10.8	10.7	26.25	3.308	22	0.498
22-1	11.3	11.2	25.32	3.321	22	0.498
21-2	11.9	11.6	24.80	3.249	21	0.502
21-1	13.3	13.0	23.83	3.244	21	0.502
20-2	14.1	13.6	22.54	3.142	20	0.505
20-1	14.5	14.0	22.73	3.162	20	0.505
22-R1	15.8	15.4	22.93	3.238	22	0.644
23-R5	15.9	15.6	23.36	3.263	23	0.639
24-R2	16.1	15.8	23.74	3.280	24	0.676
19-1	16.4	15.6	21.55	3.078	19	0.507

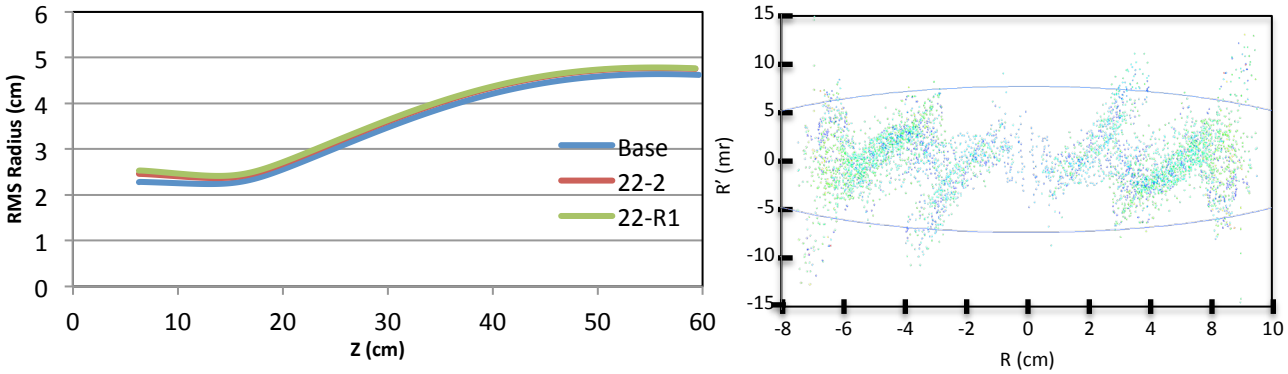

Figure 4-7. Beam RMS radius is shown as a function of longitudinal distance on the left. Phase space for Case 22-R1 is shown at Z = 55 cm on the right.

Simulations of Neighboring Emission Spots

The beamlet, or electrons, emitted from a tuff of velvet will affect the electrical field and emission from a neighboring tuff. An assumption of the magnitude of this neighboring effect was made in the previous Section when estimating the diameter of emission spots. Simulations were performed to provide an intuitive feel for the effect and validate the earlier assumption. Figure 4-8 illustrates the simulations performed. A single tuff of velvet with plasma sheath was modeled as a cylinder 1 mm in radius and 4 mm in length. The same overall geometry and magnetic field used in figure 4-5 was used. For a single tuff in isolation a total of 157 A was emitted. The individual orbits shown in Figure 4-8 have different current since the electric field is not uniform over the tuff. About 60% of the total current emitted is from the tip and over 85% is from the top third of the tuff.

A second tuff was placed some distance from the first tuff and moved closer until the two tuffs merged into a single tuff. The results of this study are presented in Figure 4-9. Even at distance of 10 diameters (20 mm) between tuff centers the space charge of the emitted current reduced the combined emission by 10% of what would be expected from two single tuffs. A large drop in emitted current occurs as the distance between tuffs is reduced from 2.5 to two diameters. The red curve in the plot represents the change in current based solely on emitting area as the tuffs are brought together and highlights the effect of space charge. A final simulation looked at the effect of placing a third tuff between two tuffs separated by two diameters, i.e. three tuffs in a row just touching adjacent sides. The increase in emitted current with the third tuff is only about 13% greater than for the two with a gap between. Thus, the earlier assumption for size and spacing of the emission spots is very reasonable.

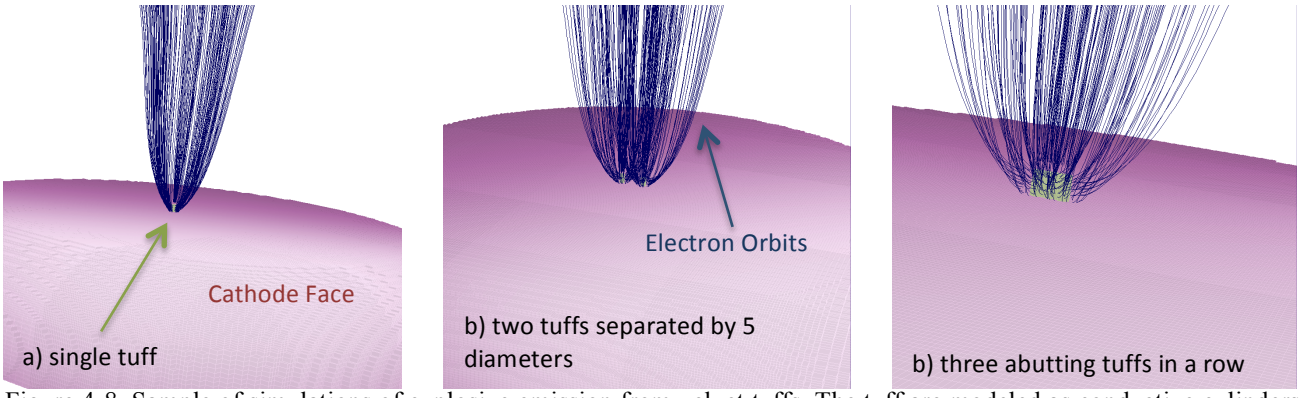

Figure 4-8. Sample of simulations of explosive emission from velvet tuffs. The tuff are modeled as conductive cylinders 1-mm in radius and 4-mm in height on the face of the cathode.

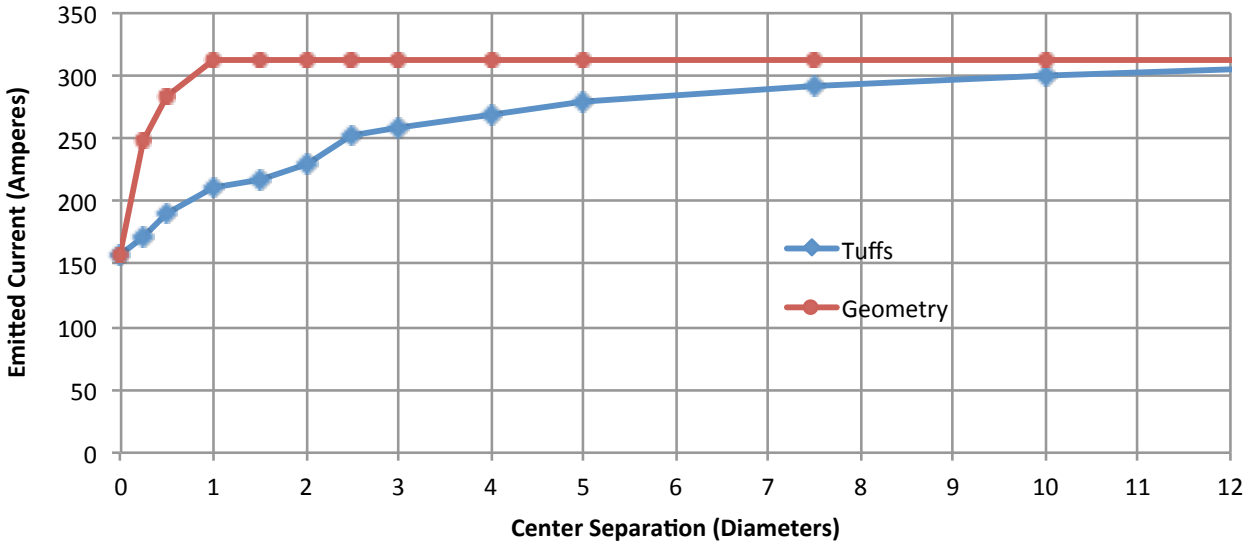

Figure 4-9. Plot of emitted current from two velvet tuffs as a function of separation.

Defining a Figure of Merit (FOM)

The emittance does vary for the different emission spot patterns used in the simulations. A goal of this study is to relate obvious characteristics of the spot pattern to emittance. In Figure 4-10 plots of the number of spots in the emission area and the standard deviation of the pattern from a uniform grid in relationship to the calculated emittance are shown. The standard deviation from a uniform pattern is determined by placing a square grid pattern over the emission surface as shown in Figure 4-11. The size of the grid pattern was chosen such that for a uniform spacing of spots that cover the emission surface, each grid square would contain an emission spot. The standard deviation is defined as:

$$\sigma = \left[\frac{\sum(G_{i,j}-\bar{G})^2}{N-1}\right]^{1/2}, \text{ where } G_{i,j} \text{ are the number of spots in grid square (i,j), } \bar{G} = \frac{\#}{N}, \tag{4-2}$$

is the total number of emission spots, and *N* is the number of allowed grid squares (non-shaded squares in Figure 4-11).

The choice of grid pattern is important. The ideal pattern would have a single emission spot in the center of each grid when the velvet surface is uniformly emitting. Non-Cartesian grids were explored with the thought that they might prove to be more suitable for the circular beam. Generating equal area grid elements proved to be overly complicated and the decision was made to use a square grid pattern. The edge length was selected to be equal to the diameter of an emission spot including allowance for plasma and space charge expansion. In the case of the simulations this size was approximately the diameter of the circles defining emission regions. Edges much different than the criteria would either not resolve the position of emission spots, or allow emission spots to be physically located too near each other.

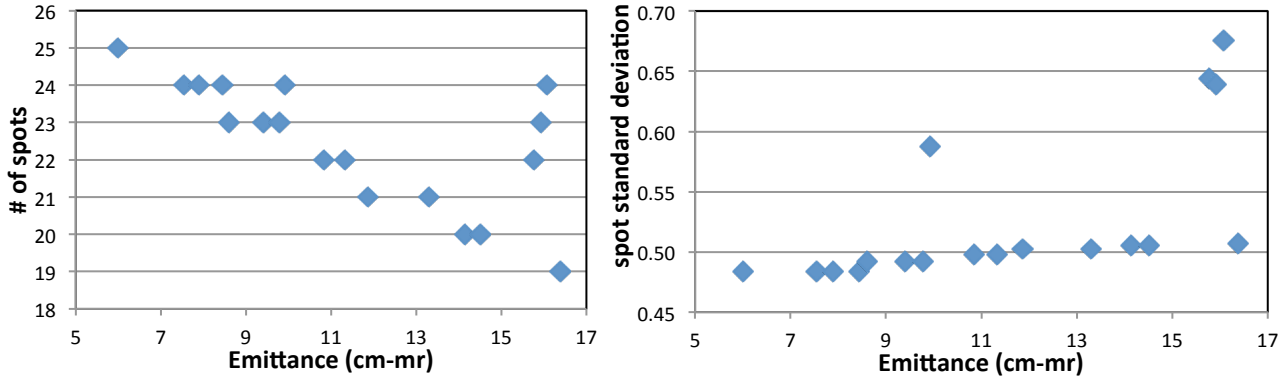

Figure 4-10. Plots of the number of spots and variation from uniform pattern as function of emittance.

The effect of the number of spots on emittance is interesting. The number of emitting spots is closely tied to total current and varied linearly with emittance except for a few outliers as seen in Figure 4-10. As long as there is no, or very little overlap, the number of spots is a very good indicator of emittance. Due to the close relationship between spots and current, emitted current is also a good gauge of emittance in the simulations. In actual operations, the emitted current is a less reliable indicator. Variation in the diode voltage can be used to correct for changes in emitted current requiring perveance to be measured to establish a consistent indicator. This will be discussed more in the Conclusions section. There is an additional problem of current loss in the anode stalk that would bias current measurements made at the injector exit.

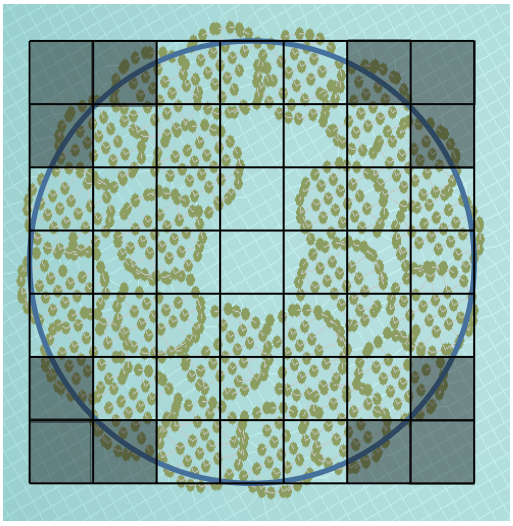

Figure 4-11. Example of grid array to check for emission spot uniformity.

The standard deviation as defined in Equation 4-2 is also a good indicator of emittance with the exception of a few outliers. Several FOM's were attempted based on a combination of number of spots and standard deviation with the goal of forcing the behavior of the outliers for the two measurements to cancel. These FOM's allowed reasonable correlation with simulated emittance. However, a more straightforward approach was to determine the number of grid elements with one or more emission spots, i.e. filled elements, and use that number as the FOM. Basically the outliers noted in Figure 4-10 are due to spots overlapping in the same grid element and merging into a single spot. Figure 4-12 illustrates the success of this approach. More and smaller spots with an appropriately finer grid are expected to produce a better fit.

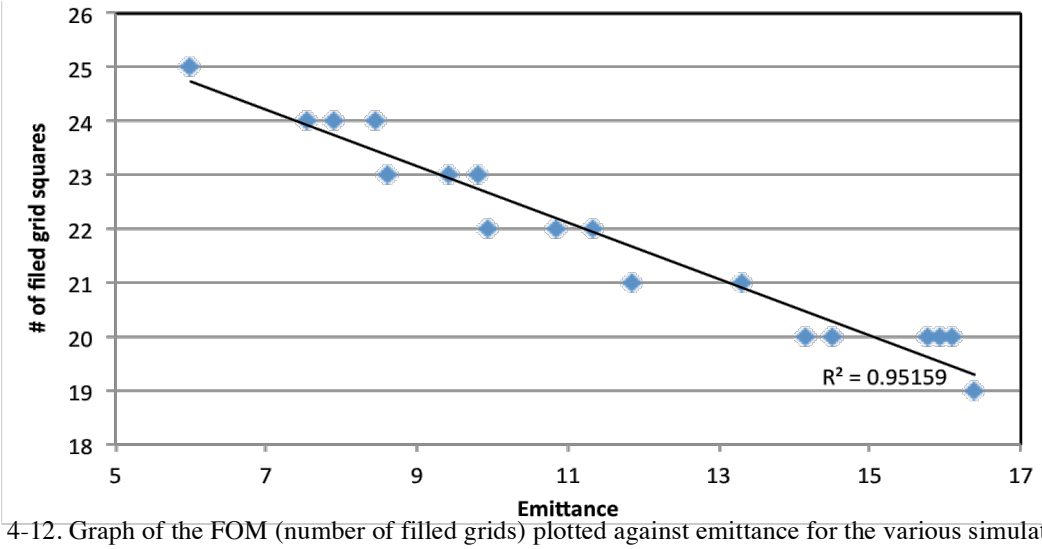

Figure 4-12. Graph of the FOM (number of filled grids) plotted against emittance for the various simulation cases.

5 Automated Image Analysis

There are two parts to the automation of the image analysis. The first is the image manipulation and extraction of desired information. The second part is automating the operation of the camera and acquisition of the cathode images. This proved to be much more difficult than expected primarily due to vendor supplied software.

Calculating and Displaying FOM

There are two important numbers that can be found in the cathode image. First, the simulations indicate the number of emission spots is a reasonable indication of the beam quality generated from the velvet surface. Next is the amount of "starring" in the cathode image that is useful in determining beam loss in the anode. There are several steps and some subtleties in extracting the desired information. A description of the process is given below. The actual image manipulation is done using ImageJ™[43] while LabView™[44] is used as the user interface.

1. The average background (median of pixel values) is determined for two rectangular regions away from the velvet surface (refer to Figure 5-1a).
2. The outliers (stars) are removed from the image. The outliers are removed by replacing pixel values by the median of the surrounding pixels (nearest neighbors, i.e. adjacent pixels) if the value deviates from the median by more than a certain value (1,000). A new average background is determined (refer to Figure 5-1b).
3. The new average is subtracted from the old to give a value related to the amount of "starring". (# Stars)
4. The image is scaled, actually stretched in the horizontal direction by a factor of 3.68 over the vertical (refer to Figure 5-1c).
5. An oval region of interest (ROI) is selected that encompasses the velvet surface and the image is cropped outside of the ROI (refer to Figure 5-1d).
6. A spatial (2D FFT) bandpass filter is performed that removes high spatial frequencies (blurring the image) and low spatial images (similar to subtracting a blurred image). Pixel values are then scaled so that the lowest value is set to 0 and the highest value is set to 255 (refer to Figure 5-1d). The bandpass filter will be discussed in more detail below.
7. Local maxima are determined by establishing a contiguous area around each maximum based on a threshold set at the maximum value minus a noise value (10). For accepting a maximum, the area must not contain any pixel with a higher value than the maximum (refer to Figure 5-1e). Maxima are excluded if the tolerance area falls outside of the cropped image. The XY coordinates of each maximum are recorded.

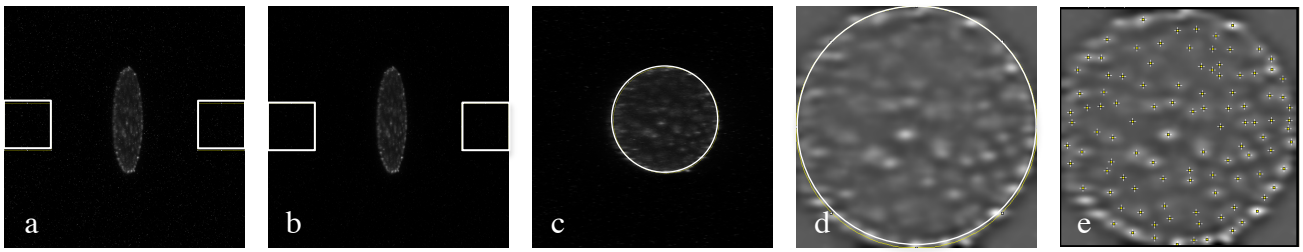

Figure 5-1. The series of images illustrates the image manipulation and analysis performed to determine the number of effective emission spots. Image shown is Shot #170571.

A square grid array is constructed that covers the image excluding corner elements that fall outside the ROI as shown in Figure 5-2. The choice of grid array element size and the parameters for the bandpass filter are related and not arbitrary. The diameter of the emission spots and emitted beam of current was estimated in Section 3 as 4.5 mm. Simulations in Section 5 indicate that if the emission spots are closer than this diameter overall emission will be suppressed. If the spots are more widely separated new emission spots could form between the existing spots. The bandpass filter is set to remove features with diameters less than about 3 mm and those with diameters larger than about 9 mm. Selecting an inappropriate diameter for the emission spots would lead to actual data being lost. After filtering, the peaks representing emission spots can be identified and located on the grid array. For the grid array, the element size should match the expected diameter of the emission spot such that every element will coincide with a spot for a uniformly emitting velvet surface. The size array chosen and shown in Figure 5-2 was a 13X13 pattern over 57 mm for an element edge length of 4.4 mm.

The quality or emittance of the beam was found in the simulations to be related to the number of filled grid elements. For the image analysis software the FOM has been defined as the number of filled elements divided by the

total number of allowed elements (169 – corners = 137). There is an important caveat with the analysis for finding the FOM. The software assumes that there is a cathode image within the ROI. If there is no image, just background noise, the bandpass filter will enhance the signal to noise ratio for pixel variations that are on the same scale as emission spots. This would lead to identifying maxima that are not image related and yielding FOM values approaching 1. Note that a background image should be a uniform field and that is what is desired for a good cathode image. A poor choice in trigger delay and exposure time can also produce an mage where features are not prominent. Images after the main voltage pulse will show the bright edge and little information over the velvet surface. The analysis software for such an image would likely show a high FOM although the image lacks any true content.

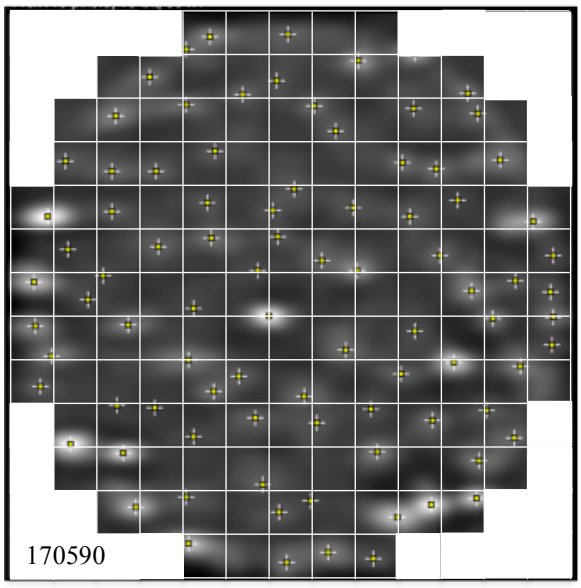

Figure 5-2. Grid array for calculating FOM.

The trigger delay time and exposure length for images used in calculating the FOM are important parameters. Plots of the number of filled elements (maxima) as a function of delay (10 ns exposure) and exposure (ns) are shown in Figure 5-3. The

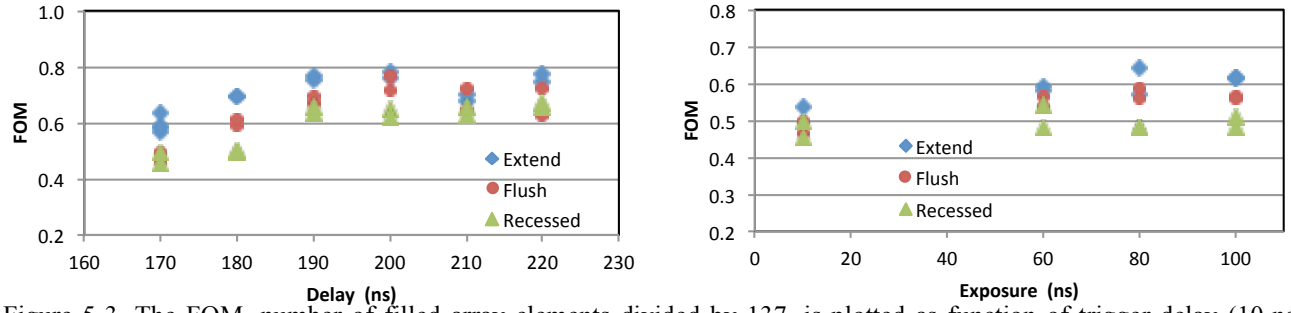

Figure 5-3. The FOM, number of filled array elements divided by 137, is plotted as function of trigger delay (10-ns exposures) and exposure time (170-ns trigger delay). Data from 1 March 2012.

data for the recessed velvet case is biased due part of the velvet surface being below the edge of the shroud. The increase in maxima with increased trigger delay is most likely due to emission spots being obscured by the expanding plasma front resulting in a more uniform light distribution. Refer to Figure 2-8 for 10-ns exposure images at different delays with respect to the current pulse. Interestingly, holding the trigger delay at 170 ns, the beginning of the current pulse, and increasing the exposure time has little effect on the number of maxima. Four analyzed images with peaks marked for the flush velvet and different exposure lengths are shown in Figure 5-4. Basically a subjective decision, for routine analysis a trigger delay of 170 ns and an exposure of 80 ns was chosen. The cathode image is comprised of light integrated from the start of the pulse through the entire portion of the pulse transported to the accelerator.

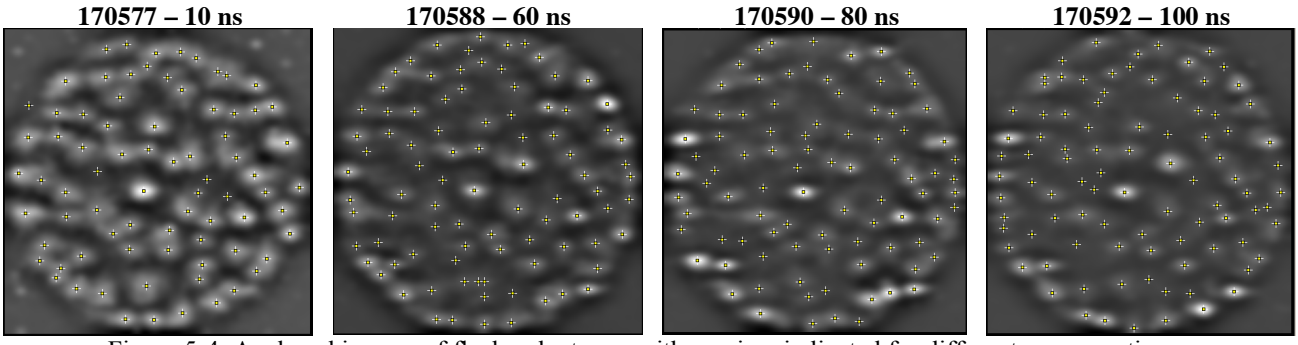

Figure 5-4. Analyzed images of flush velvet case with maxima indicated for different exposure times.

Additional information provided by the analysis software is the integrated pixel intensity over the ROI (refer to Figure 5-5) and the location of the center of the maxima (refer to Figure 5-6). Plotted as a function of trigger delay, all three velvet positions exhibited similar highest intensity at start of pulse followed by a small drop and then a slight

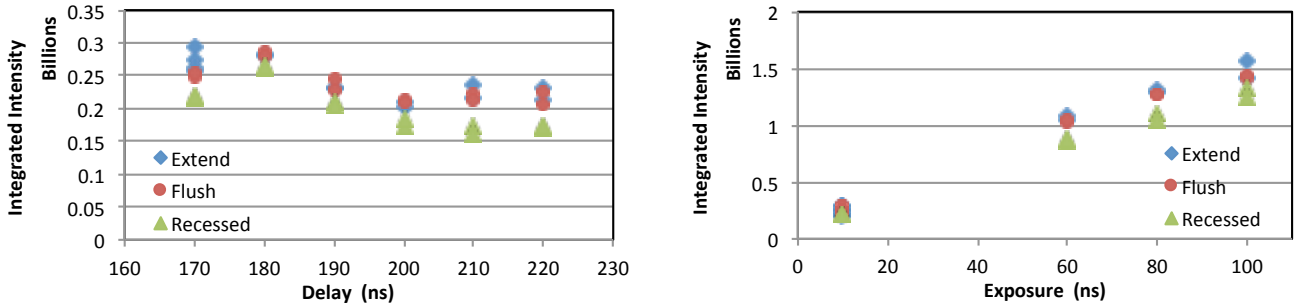

Figure 5-5. The integrated pixel intensity is plotted as function of trigger delay (10-ns exposures) and exposure time (170-ns trigger delay). Data from 1 March 2012.

increase similar to data plotted in Figure 2-8. Plotted as a function of exposure time for a 170-ns delay, the integrated intensity was nearly linear. This behavior supports the hypothesis that the light is created by an approximately constant source during the pulse located near the surface of the velvet and is scattered by the expanding plasma. The plot of maxima center in Figure 5-6 shows that the Flush velvet was more consistent.

The Star Count is used for detecting beam loss in the anode entrance and reflects the amount of x-ray noise imposed on the signal. Figure 5-7 plots the Star Count as a function of both trigger delay for a fixed exposure length (10 ns) and exposure length for a fixed delay (170 ns) for the three cases where the velvet position was varied. The data was consistent with expectations. All three cases exhibited a relative high count at the beginning of the pulse where the diode voltage (beam energy) is still increasing and the beam is not matched to the magnetic transport fields. For the Flushed and Recessed cases, the Star Count drops to a low value as the voltage (beam energy) reaches a steady state value matched to the transport, i.e. little beam is lost in the anode. In contrast, the Extend case retains a high Star Count throughout the pulse indicating a mismatched beam. The plot for exposure length is essentially an integration of the first plot starting with the value for 170 ns delay. Thus, for the Extend case the Star Count increases linearly with exposure time while the other two cases remains approximately constant.

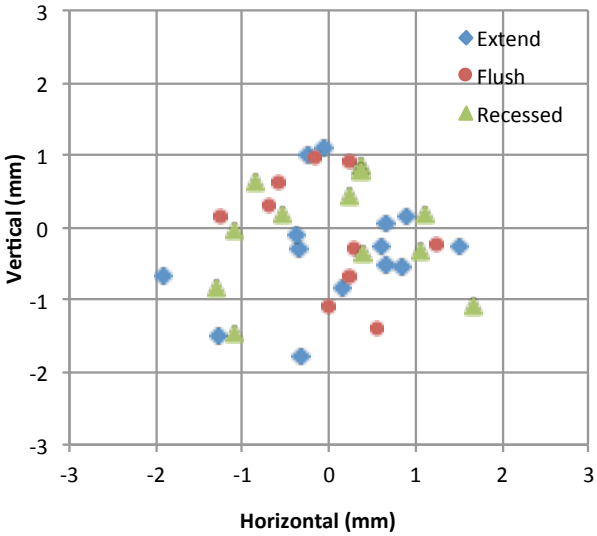

Figure 5-6. Position of the maxima centers is plotted for image data from 1 March 2012.

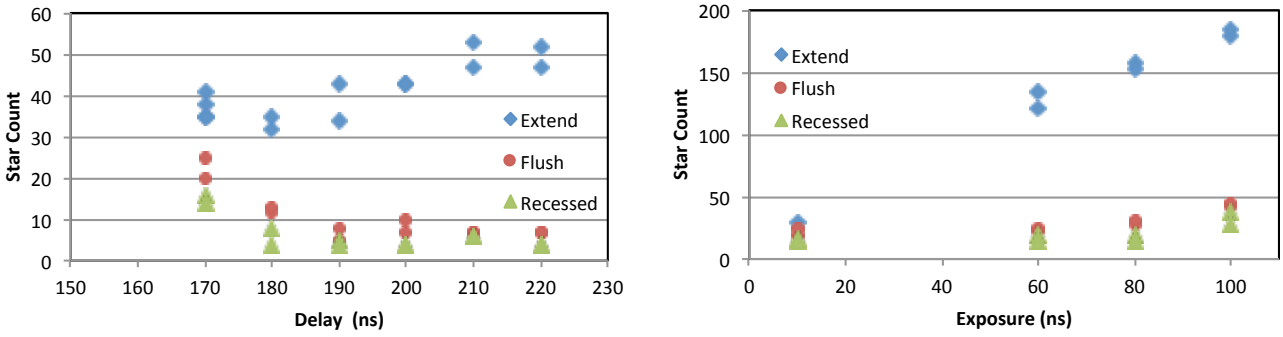

Figure 5-7. The Star Count is plotted as a function of trigger delay (10-ns exposures) and exposure time (170-ns trigger delay). Data from 1 March 2012.

The image analysis has been fully automated as a standalone LabView™ virtual instrument (VI). A screen shot of the prototype front panel for the analysis software is shown in Figure 5-8. The software generates and saves a series of images similar to those shown in Figure 5-1 during the analysis for later review as well as saving calculated information, e.g. FOM, spot locations, etc., to a spreadsheet. All data analysis shown in this Section was generated with this analysis software. The software will become a subVI in the FXR Data Acquisition System.

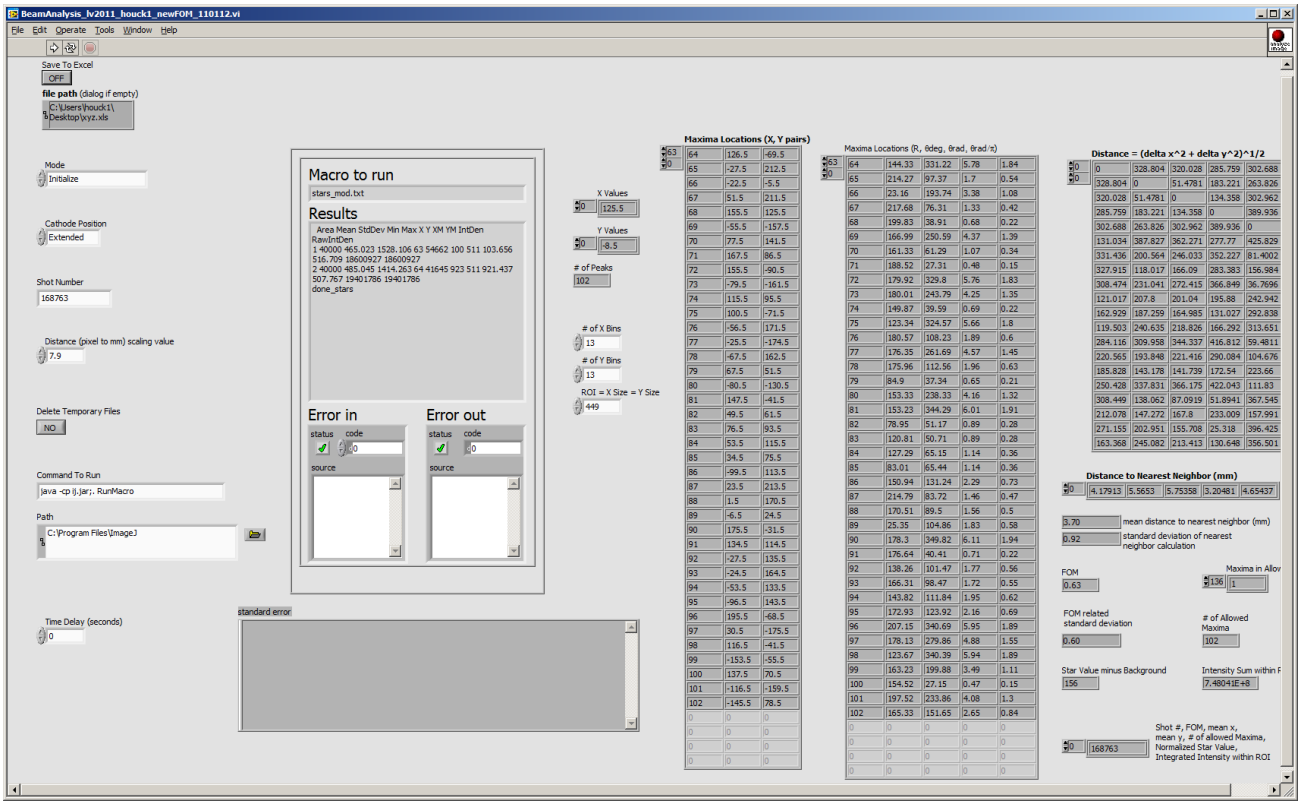

Figure 5-8. Screen shot of Data Analysis software VI front panel.

Automating Camera System and Integrating With FXR Control System

Automating the camera system is critically important due to the size of the operations crew. There is simply no one available who can watch the camera when the accelerator is operating. And the camera does require regular attention for effective integration into operations. A good example of this attention refers to arming the camera in preparation for acquiring an image. The CCD array begins accumulating dark current (thermal noise) as soon as the camera is powered. A "cleaning" cycle occurs on a regular basis to remove the accumulated noise. However, once armed the "cleaning" cycle ceases, so preferably the camera is triggered immediately after arming to reduce the accumulated noise. The time interval between armed and triggered should be kept constant to maintain similar backgrounds for images. To arm the camera shortly before a hydrodynamic test or even an accelerator check requires a member of the operational crew to shift their attention from preparing the accelerator for operations, move to a different computer, select an option on the display, and then return focus to the accelerator. Consistently following this process for a human is not a reasonable expectation. The crew needs to rely on a computer system that monitors the accelerator firing sequence and prepares/triggers the camera as needed. In the past a special team member was added to the crew when cathode images were desired. While not as consistent as a computerized system, a dedicated camera operator does work. The issue is that a dedicated camera operator is not routinely, or even normally, available and the recorded cathode image database is incomplete.

There are three camera parameters that need to be fully integrated into the control system such that the accelerator operator can monitor/set/change their values at the Accelerator Operations Console. Those items are camera Armed, exposure time (Pulse Width), and trigger delay (Pulse Delay). Other camera parameters that are desirable to monitor, but not necessary to control from the Accelerator Operations Console, are the image file name, camera gain, and the external trigger parameters. These monitored parameters can be set at the local control when the camera is initially powered. *Princeton Instruments/Roper Scientific*, the camera manufacturer, and *R Cubed Software*, a custom software design company specializing in CCD technology and image processing are the primary companies responsible for the software drivers used for the PI-MAX line of cameras. *Princeton Instruments* provides a software package called WinView™ for image acquisition, display, processing, and archiving with the PI-MAX cameras. WinView™ is a standalone package designed for use on computers running a 32-bit Windows OS. *R Cubed Software* sells software called the Scientific

Imaging ToolKit™ (SITK®) that allows a user to setup and control all *Princeton Instruments* cameras with LabView™, the software used for the FXR Control System. This toolkit gives the user the ability to setup experimental conditions for a camera (ROIs, exposure, temperature, etc.), collect data from the camera, perform image math and display and store the images. All of these functions are optimized in C and are callable from LabView™. *R Cubed Software* has written the majority of LabView VI's used in SITK and is the contact for software problems involving SITK.

Unfortunately, there appears to be an error in a code interface node of one of *R Cubed* supplied VI's that effects the Pulse Delay function. *Princeton Instruments* has been able to supply standalone executables, dynamic link libraries (dll's) and data files that could control the Trigger Delay. However, this software did not work correctly when incorporated with the *R Cubed* supplied VI's. Automating the camera system and integrating with the FXR Control System is still in progress.

A prototype Operator's Control Console screen is shown in Figure 5-9. The SHOT is an automatically generated number identifying the pulse that is provided to the VI by the control system. FOM and STARS are generated by the analysis software as well as the average location of the emission spots.

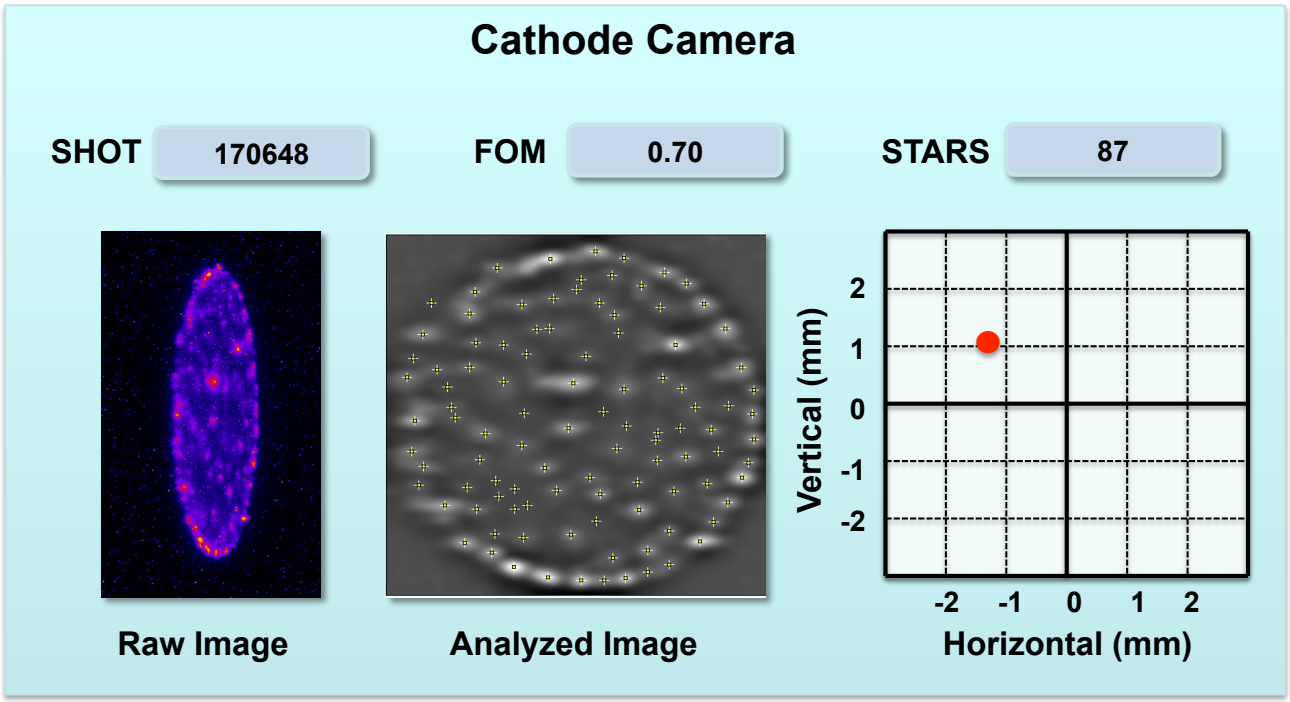

Figure 5-9. Prototype for the Operator's Control Console screen.

Reviewing Old Images/Historical Data

The analysis software is a powerful tool for acquiring information from the images. Once the software is incorporated in the FXR Data Acquisition System, the Trender[45] software will be able to display the stored analyzed data allowing for easy observation of cathode performance trends.

An example of using the analysis software is given in Figure 5-10. The Figure of Merit (FOM) for cathode images taken on 8 consecutive operational days is plotted. All images for this period were taken with a 170-ns trigger delay and a 40-ns exposure length. There is a large amount of scatter, but the data for day 01/01/2001 falls well below the others and is significantly different than for the preceding day, 10/25/2010. This observation led to checking the FXR Operational Log Book and discovering that the velvet had been replaced on 11/28/2010. Plotting the average value of maxima as a function of number of pulses on the new velvet. After about 50 pulses, sometime on the third operations day, the FOM had reached a nearly constant value of 0.585 that compares reasonably well with the value of 0.595 for the last operations day before the velvet change.

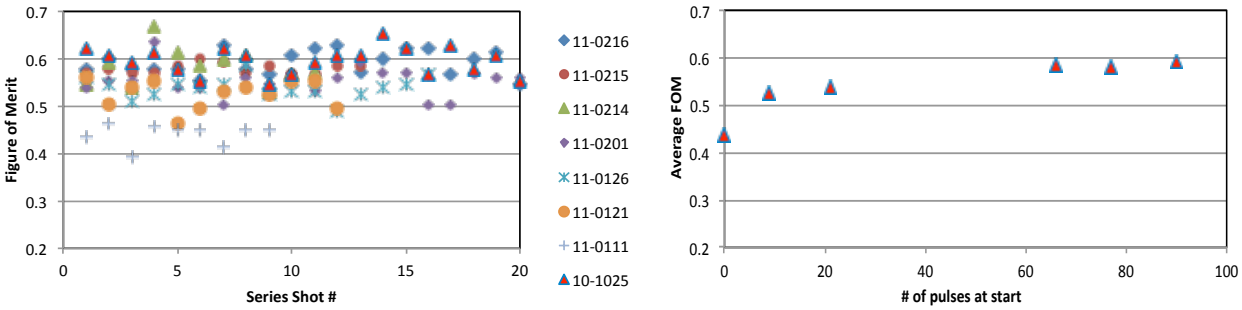

Figure 5-10. Plot of FOM per image on left and plot of average FOM per daily image set on right.

The improved performance with increase number of pulses may be due to the establishment of current paths through the tape backing. Figure 5-11 is a series of the first 4 cathode images on the new velvet. Each shot shows a qualitative improvement in uniformity. Interestingly, there is not a noticeable improvement during a specific operating day. The change in FOM occurs between operation days. There were two reasons for replacing the velvet at this particular time. First was that the injector was open for the replacement of the anode VRD diagnostic and the cathode was readily available. The second was that while the injector was opened a damaged spot was noticed on the velvet. To explore the effect of the damaged spot on the image, the images from a specific day were combined, i.e. added together. Refer to Figure 5-12 where the combined images are shown for four days: 10/25/2010, 01/11/2011, 01/21/2011, and 02/16/2011. The number in the upper left corner indicates the number of images that were added together. The pixel intensity range for the images used in Figure 5-12 is half that for those used in Figure 5-11.

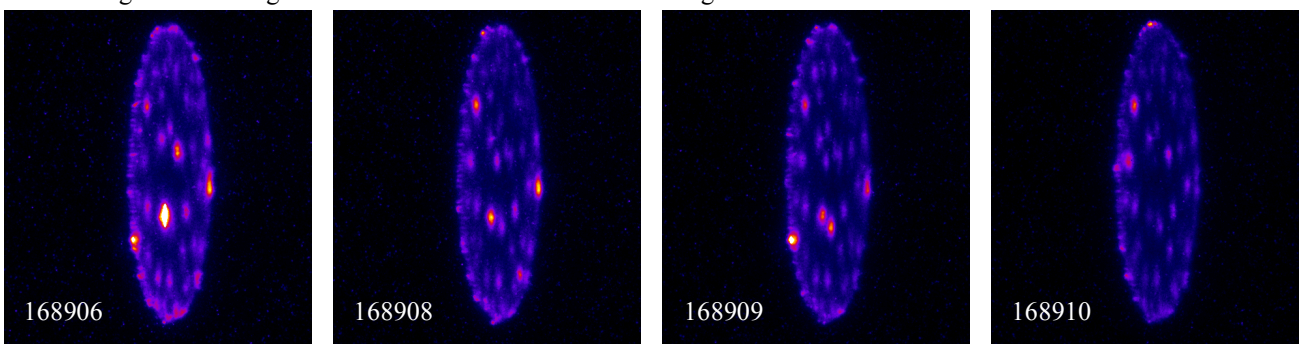

Figure 5-11. Cathode images taken immediately after the changing of the velvet in November 2010.

The images taken on 10/25/2010 all had a brighter spot at the same location on the interior of the velvet. Bright emission spots of the edge of the velvet are common and tend to shift location. Also, new velvet will exhibit bright interior spots as the velvet is "burned in" (refer to Figure 5-11 and 01/11/2011 combined image in Figure 5-12). However, for conditioned velvets this persistent bright spot is unusual. This spot did correspond to the damaged spot on the velvet.

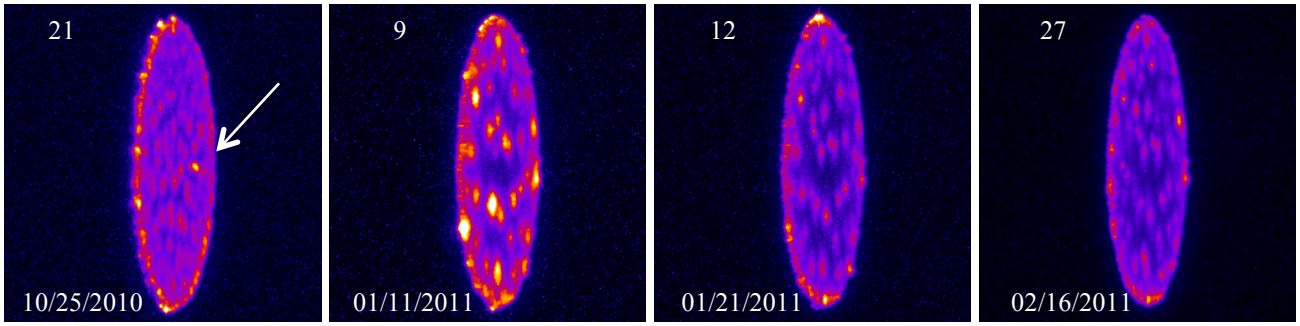

Figure 5-12. Composite cathode images produced by summing images taken on the same day. Number in upper, left corner refers to number of images summed. Arrow in left image points at brighter interior emission spot associated with damage to the velvet surface.

6 Conclusions

Emission from the cathode's velvet surface is strongly impacted by the backing to the velvet. Specifically, the current paths through the material attaching the velvet to the conductive structure of the cathode produces magnetic fields that affect the transverse forces on the emitted current. If the current paths are uniformly distributed through the velvet the total magnetic field generated approaches that of a cylindrical beam. If the current paths are not uniformly distributed the resulting magnetic field no longer has the azimuthal symmetry found with a cylindrical beam, and the electron orbits are deflected asymmetrically. The orbits will merge into a beam with essentially uniform current density. However, the beam will have higher transverse motion, i.e. emittance, than if the orbits had started with an azimuthally symmetric magnetic field. Beam emittance is an important beam quality for a radiographic accelerator such as FXR. The contribution from emittance to the beam diameter or x-ray spot size varies as the square root of emittance.

Images taken of the FXR cathode indicate a very non-uniform distribution of bright spots. These spots are areas where current flows through the velvet backing when high electrical fields are applied to the surface resulting in explosive emission. The velvet backing is critical. The double-sided tape used at FXR is nonconductive and current paths are "burned" through the tape during initial operations and remain until the velvet is changed. When the explosive emission occurs plasma is produced that expands outward from the velvet into a surface from which electrons are emitted. The images indicate that the initial emission spots remain during the entire HV pulse and, it is assumed, are the source of the currents running through the plasma to the emission surface. The spacing of the emission spots is determined by the size of the velvet tuffs, plasma expansion velocity, and emitted electron space charge. Once a tuff explodes into emission, the space charge of emitted electrons will suppress the surface electric field in the vicinity preventing neighboring tuffs from emitting. Plausible assumptions and measured emission spots indicate that for FXR parameters the diameter around an emission spot is about 4.5 mm.

The difficulty and expense of performing emittance measurements and cathode experiments on FXR required substituting simulations to determine the effect of non-uniform emission. The simulations indicated that a non-uniform distribution of emission spots would increase beam emittance. The simulations were used to establish a figure of merit (FOM) based on the number and distribution of emission spots. Based on the established FOM, we estimate that the emittance for the presently installed FXR cathode velvet could be increased by a factor of three over the minimum value for uniform emission. The simulations also indicated that placement of the velvet surface with respect to the face of the cathode shroud is important, e.g. extending the velvet above the surface of the shroud produces significantly higher beam emittance. The emittance increase is reduced somewhat when portions of the beam intercept the interior of the anode stalk and current is "scraped off". Operationally, the extended velvet leads to a larger diameter beam that is collimated by the anode. The beam exiting the anode is smaller diameter, reduced current, but centered on the mechanical axis of the accelerator and is less subject to exciting the transverse instability or BBU.

The cathode camera system has been automated with exception of the trigger delay. The camera has not been integrated into the FXR Control System due to vendor errors in the software drivers for the camera. Images can be captured, saved to disk, and analyzed through a LabView™ interface. The camera can be operated locally and images analyzed interactively through the software.

During this study several issues with the diode B-Dot diagnostic were found. The most serious is that the connection between the diagnostic cables and individual RF loops is not stable. Removing and reattaching the cable can change the resistance and bandwidth of the connection causing a calibration change. Relative changes in beam current and displacement can be inferred from B-Dot data taken during a series where the cable connections are undisturbed. However, an absolute calibration of the B-Dot is not presently possible. The location of the RF loops with respect to the injector spool is not optimum, but the effect can be modeled and used to calibrate the diagnostic. The B-Dot provides the most direct measurement of cathode emission and should be given priority for repair.

In summary:

1. Present means for securing the velvet to the cathode is contributing to an increase in beam emittance
2. Known techniques can be used to establish a uniform pattern of emission spots and improve emittance
3. Extending the velvet surface beyond the face or plane of the cathode shroud increases emittance
4. A FOM based on number and uniformity of emission spots has been established
5. Majority of the cathode camera functionality has been automated
6. Analysis of the cathode camera images has been automated
7. The cathode camera is a good diagnostic for spotting/locating cathode shroud explosive emission
8. The cathode camera is a good diagnostic for spotting beam scraping in the anode stalk

9. FXR does not have an issue with explosive emission from the shroud at this time
10. Performance of the diode B-Dot diagnostic has been analyzed and documented in this study

There are a number of actions and experiments recommended:

1. Replace red with black velvet to observe changes in image pedestal height
2. Use different backing (conductive epoxy) and/or mounting (stretched directly over metal surface) of velvet
3. Cut a uniform hole pattern into backing material and/or velvet, vary hole size and pattern
4. Perform emittance measurements on FXR to compared with FOM
5. Purchase new Gen III cameras
6. Increase resolution in simulations and expand number of emission sites
7. Upgrade or repair B-Dot diagnostic and write an installation procedure including cable connections

The cathode camera provides a substantial amount of useful data. Until we can correlate images with beam emittance measurements, the images will only provide guidance. However, images immediately after a velvet installation will indicate if there is a problem with the installation allowing for immediate correction. Without the camera an installation error is not obvious and would lead to a lengthy period of suboptimal performance while multiple systems are analyzed. The mostly like scenario for realizing the error would be a number of poor radiographs.

References

[1] B. Kulke, et al., "Design of a 20 MeV, 4 kA Linear Induction Accelerator, 1980 IEEE International Conference on Plasma Science, Madison, WI, 19-21 May 1980 (UCID-18939)
[2] L.G. Multhauf, "The LLNL Flash X-Ray Induction Linear Accelerator (FXR)," Procceedings of The 25th Conference on High Speed Photography and Photonics, Beaune, France, September 12-October 4, 2002 (UCRL-JC-148534)
[3] J_M. Zentler, et al., "Improved Focus Solenoid Design For Linear Induction Accelerators," Proceedings 16th International Linear Accelerator Conference, Ottawa, Ontario, Canada, August 23-28, 1992 (UCRL-JC-111229)
[4] R.D. Scarpetti, et al., "Upgrades to the LLNL Flash X-Ray Induction Linear Accelerator (FXR)," Proceedings 11th IEEE International Pulsed Power Conference, Baltimore, MD, June 29-July 2, 1997 (UCRL-JC-128385)
[5] M.M. Ong, et al., "LLNL Flash X-ray Radiography Machine (FXR) Double-Pulse Upgrade Diagnostics," Proceedings 11th IEEE International Pulse Power Conference, Baltimore, MD June 29-July 2, 1997 (UCRL-JC-125879)
[6] Y-J Chen, "Nuclear instruments & methods, Phys Res A, Vol. 398, Pp. 139-146, 1997 (UCRL-JC-109600-REV-1)
[7] M.M. Ong, et al., "Flash X-Ray (FXR) Linear Induction Accelerator (LIA) Optimization" Timing-error (Voltage-variation) Reduction," December 2005 (UCRL-TR-219445)
[8] T.L. Houck, et al., "Design of a High Field Stress, Velvet Cathode for the Flash X-Ray (FXR) Induction Accelerator," Proceedings 2007 Particle Accelerator Conference, Albuquerque, NM, June 25-29 2007 (UCRL-PROC-231690)
[9] T.L. Houck, et al., "Recent Flash X-Ray Injector Modeling," LLNL, UCRL-TR-208574, 14 December 2004
[10] A.C. Paul, "Flash X-Ray Injector Study," LLNL, UCRL-TR-203991, 26 March 2004
[11] A.C. Paul, "Flash X-Ray Injector and Accelerator Study," LLNL, UCRL-TR-212069, 6 May 2005
[12] G.P. LeSage, et al., "Time-resolved emittance characterization of an induction linac using Optical Transition Radiation," LLNL, UCRL-ID-153254, 5 November 2002
[13] J.S. Jacob, et al., "Time-resolved OTR Emittance Measurement," LLNL, UCRL-TR-214037, (2005)
[14] T.L. Houck, et al., "Tuning the Magnetic Transport of an Induction Linac using Emittance," LLNL, UCRL-CONF-223696, (2006)
[15] T.L. and P.E. Wargo, "Flash X-Ray (FXR) Linear Induction Accelerator (LIA) Optimization: Upgrade of the OTR Emittance Diagnostic," December 21, 2006 (UCRL-TR-226954)
[16] M.M. Ong, et al., "Flash X-Ray (FXR) Linear Induction Accelerator (LIA) Optimization: Cathode Camera System and Preliminary Images," November 16, 2006 (UCRL-TR-226156)
[17] T.L. Houck, et al., "Design of a High Field Stress, Velvet Cathode for the Flash X-Ray (FXR) Induction Accelerator," Proceedings 2007 Particle Accelerator Conference, Albuquerque, NM, June 25-29 2007 (UCRL-PROC-231690)
[18] Ya.E. Krasik, et al., "Characterization of the plasma on dielectric fiber (velvet) cathodes," J. Appl. Phys. **98**, 2005
[19] Ya.E. Krasik, et al., "Characterization of the plasma on dielectric fiber (velvet) cathodes," J. Appl. Phys. **98**, 2005
[20] Y.M. Saveliev, W. Sibbett, and D.M. Parkes, "Current conduction and plasma distribution on dielectric **(**velvet**)** explosive emission cathodes," J. Appl. Phys., Vol. 94, No. 12, 15 December 2003
[21] T.J. Fessenden, "Diagnostics for Induction Accelerators," LBNL, LBL-38523/UC-419, April 1996
[22] YJ Chen and T.J. Fessenden, "Improvements on the Accuracy of Beam Bugs," Proceedings 1998 Linear Accelerator Conference, Chicago, IL, August 23-28 1998 (UCRL-JC-130462)
[23] Nye, Holly L., "Experimental Analysis of B-dot Sensors", Naval Postgraduate School, June 1990, AD-A238 487
[24] C. A. Ekdahl, "Fourier analyzing coil arrays for pulsed relativistic electron beam experiments," Rev. Sci. Instrum. 55, 1221 (1984)
[25] W.K.H. Panofsky and M. Bander, "Asymptotic Theory of Beam Break-Up in Linear Accelerators," Rev. Sci. Instrum, **39** (2), pp. 206-212, 1968
[26] V.K. Neil and R.K. Cooper, "Coherent Instabilities in High Current Linear Induction Accelerators," Part. Acc. **1**, pp. 111-120, 1970
[27] V.K. Neil, L.S. Hall, and R.K. Cooper, "Further Theorectical Studies of the Beam Breakup Instability," Part. Acc. **9**, pp. 213-222, 1979
[28] P.R. Menge, et al., "Beambreakup growth and reduction experiments in long-pulse electron beam transport," J. Appl. Phys., Vol. 75, No.3, 1 February 1994
[29] R.B. Miller, "Mechanism of explosive electron emission for dielectric fiber (velvet**)** cathodes," J. Appl. Phys., Vol. 84, No. 7, 1 October 1998
[30] T. Houck, et al., "Study of Vacuum Insulator Flashover for Pulse Lengths of Multi-Microseconds," UCRL-CONF-223361, July 2006
[31] Saveliev, JAP 94 2003
[32] Ya.E. Krasik, et al., "Characterization of the plasma on dielectric fiber (velvet) cathodes," J. Appl. Phys. **98**, 2005

[33] Y.M. Saveliev, W. Sibbett, and D.M. Parkes, "Current conduction and plasma distribution on dielectric **(**velvet**)** explosive emission cathodes," J. Appl. Phys., Vol. 94, No. 12, 15 December 2003
[34] M. Ong and R. Paris, "FXR (Flash X-ray Radiography) Beam Breakup Instability (BBU) Analysis Using B-dot Sensor Data," to be published as a LLNL Technical Report
[35] S. Humphries, Jr., **Charged Particle Beams**, John Wiley and Sons, 1990 – free electronic version can be down loaded at http://www.fieldp.com/educa.html, pp 631-640
[36] J.R. Pierce, *Theory and Design of Electron Beams*, Van Nostrand, Princeton, NJ 1949
[37] T. Houck, et al., "Double Pulse Experiment with a Velvet Cathode on the ATA Injector," Proceedings 2005 Particle Accelerator Conference, Dallas, TX, May 1-5 2005 (UCRL-JC-119387)
[38] **Trak** is part of the **Advanced Charged-particle Design Suite** marketed by **Field Precision LLC,** PO Box 13595, Albuquerque, New Mexico 87192 U.S.A., http://www.fieldp.com/trak.html
[39] S. Humphries, Numerical modeling of space-charge-limited emission on a conformal triangular mesh, J. Comp. Phys. 125, 488 (1996)
[40] E. Henestroza, "Sensitivity Analysis of the DARHT-II 2.5MV/2kA Diode," LBNL, 05-29-2008 http://www.escholarship.org/uc/item/4g57x7vb
[41] E.P. Lee and R.K. Cooper, "General Envelope Equation For Cylindrically Symmetric Charged-Particle Beams," Particle Accelerators, Vol 7, 1976, pp. 83-95
[42] S. Humphries, Jr., **Charged Particle Beams**, John Wiley and Sons, 1990 – free electronic version can be down loaded at http://www.fieldp.com/educa.html, pp 400-406
[43] ImageJ is a public domain Java image processing program - http://rsb.info.nih.gov/ij/index.html
[44] LabVIEW is system design software built on a modular graphical development environment - http://www.ni.com/labview/
[45] E. Koh wrote a software package incorporated into the FXR control system that allows the retrieval and display of various machine parameters. This software is particularly useful for showing changes in operational parameters over periods of time, i.e. performance trends. For this reason the software came to be know as "Trender." Trender was presented at the Engineering Technical Showcase, 21 May 2009.

Acknowledgment

We acknowledge the invaluable help from the FXR team, Jan Zentler, Blake Krietzer, Jim Dunlap, and Tom McWilliams for operating the accelerator, gathering information on the accelerator hardware, and providing insightful observations. Ed Koh wrote the operational procedure for the Cathode Camera and began the initial work for automating the camera with LabView. We gratefully thank Dr. Larry Wiley for providing the funding and suggestions for the image analysis.

Appendix A: Experiment Shot Plans

The injector was operated on three different days to produce cathode image data.

31 January 2012 Shot Log

Accomplishment for this series of shots included:

- Determination of cathode light off relative to camera delay time (165-170 ns)
- Calibration of I20 B-Dot against I35 Beam Bug (Actually mistaken and not caught until third series)
- Scanned short image exposures as function of camera delay
- Checked reproducibility of images

Accelerator Tune: Rex06					
New Cathode A-K Gap = 9.44 cm					
Camera F/S: 2.0					
Camera Gain: 255					
Shot #	**Gate**	**Delay (ns)**	**Note**		
Background1	10	140			
Background2	10				
Background3	10				
170172	100	140			
170173	100	140			
170181	10	200			
170182	10	180			
170183	20	180			
170184	20	180	Possible trigger issue		
170185	20	180	Changed PTG termination to 50 ohms		
170186	50	180	Changed PTG termination back to high Z		
170187	50	180			
170188	50	150			
170189	5	160	before beam, no light		
170190	10	160			
170191	10	150	before beam, no light		
Delay Scan			**Note**	**Background (pixels)**	**Total Intensity**
170192	10	150		78	1.040E+06
170193	10	150		79	1.146E+06
170194	10	160		84	2.086E+07
170195	10	160		75	2.631E+07
170196	10	170		94	7.028E+07
170197	10	170		87	7.038E+07
170198	10	180		88	6.957E+07
170199	10	180		88	7.136E+07
170200	10	190		87	6.853E+07
170201	10	190		86	6.348E+07
170202	10	200		87	6.768E+07
170203	10	200		95	6.763E+07
170204	10	210		90	6.298E+07
170205	10	210		91	5.861E+07
170206	10	220		94	6.250E+07
170207	10	220		96	6.419E+07
170208	10	230		95	6.694E+07
170209	10	230		99	7.052E+07
170210	10	240		93	6.984E+07

170211	10	240		93	6.389E+07
170212	10	250		92	5.919E+07
170213	10	250		94	5.964E+07
170214	10	260		94	5.074E+07
170215	10	260		98	5.791E+07
170216	10	310		75	3.107E+07
170217	10	310		80	2.043E+07
170218	10	260		95	5.357E+07
170219	10	260		97	4.788E+07
170220	10	250		95	6.380E+07
170221	10	250		95	5.682E+07
170222	10	240		99	6.379E+07
170223	10	240		97	6.177E+07
170224	10	230		99	7.202E+07
170225	10	230		94	6.653E+07
170226	10	220		93	6.544E+07
170227	10	220		94	6.393E+07
170228	10	210		92	6.057E+07
170229	10	210		96	6.142E+07
170230	10	200		90	6.167E+07
170231	10	200		93	5.922E+07
170232	10	190		87	6.543E+07
170233	10	190		90	6.734E+07
170234	10	180		88	7.821E+07
170235	10	180		89	7.882E+07
170236	10	170		87	7.236E+07
170237	10	170		86	7.125E+07
170238	10	160		82	2.576E+07
170239	10	160		81	2.653E+07
170240	10	150		80	1.132E+06
170241	10	150		79	1.072E+06

8 February 2012 Shot Log

Accomplishment for this series of shots included:

- Scanned long (100ns) image exposures as function of camera delay
- Completed two scans of exposure (gate) width for different camera delays (170ns and 190ns)
- Continued checking image reproducibility, or acquiring more data for statistical analysis

Accelerator Tune: Rex06			
New Cathode A-K Gap = 9.44 cm			
Camera F/S: 2.0			
Camera Gain: 255			
Shot #	**Gate**	**Delay (ns)**	**Note**
170263	100	150	Warm Up
170264	100	150	Warm Up
170265	100	150	Warm Up
170266	100	150	Warm Up
170267	100	150	Warm Up
Trigger Delay Scan with 100 ns exposures			
170268	100	150	

170269	100	150	
170270	100	250	
170271	100	250	
170272	100	350	
170273	100	350	
170274	100	450	
170275	100	450	
170276	100	550	
170277	100	550	
170278	100	650	
170279	100	650	
170280	100	750	
170281	100	750	
170282	100	850	
170283	100	850	
170284	100	950	
170285	100	950	
170286	100	1050	
170287	100	1050	
170288	100	1150	
170289	100	1150	
170290	10	1150	
170291	10	1150	
170292	10	1150	
170293	10	1150	
170294	100	1150	
170295	100	1150	
170296	100	1150	
170297	100	1050	
170298	100	1050	
170299	100	1050	
170300	100	950	
170301	100	950	
170302	100	950	
170303	100	850	
170304	100	850	
170305	100	850	
170306	100	750	
170307	100	750	
170308	100	750	
170309	100	650	
170310	100	650	
170311	100	650	
170312	100	550	
170313	100	550	
170314	100	550	Injector PP Anomaly
170315	100	550	Injector PP Anomaly
170316	100	450	
170317	100	450	
170318	100	450	
Background	100	**Took background during lunch break & maintenance of I13 pressure regulator.**	
170319	100	350	missed 19

170320	100	350			
170321			missed 21		
170322	100	350			
170323	100	350			
170324	100	250			
170325	100	250			
170326			missed 26		
170327	100	250			
170328	100	150			
170329	100	150			
170330	100	150			
Gate Width Scan at 170 ns Delay			**Note**	**Background (pixels)**	**Total Intensity**
170331	10	170		94	7.6412E+07
170332	10	170		89	7.4789E+07
170333	20	170		95	1.3857E+08
170334	20	170		89	1.3644E+08
170335	30	170		99	1.9826E+08
170336	30	170		102	2.0150E+08
170337	40	170		110	2.4458E+08
170338	40	170		111	2.4630E+08
170339	50	170		119	2.7459E+08
170340	50	170		117	2.6998E+08
170341	60	170		148	3.2630E+08
170342	60	170		128	3.2989E+08
170343	70	170		93	3.7055E+08
170344	70	170		140	3.6968E+08
170345	80	170		159	3.9834E+08
170346	80	170		150	3.9795E+08
170347	90	170		163	4.4804E+08
170348	90	170		174	4.3532E+08
170349	100	170		180	4.7221E+08
170350	100	170		187	4.5310E+08
170351	10	170		105	7.7427E+07
170352	10	170		88	7.4719E+07
170353	10	170		106	8.1135E+07
170354	20	170		93	1.4019E+08
170355	20	170		94	1.3874E+08
170356	20	170		91	1.3545E+08
170357	30	170		91	1.9550E+08
170358	30	170		101	2.0172E+08
170359	30	170		106	1.9544E+08
170360	40	170		110	2.4423E+08
170361	40	170		174	2.5435E+08
170362	40	170		111	2.4755E+08
170363	50	170		81	2.7207E+08
170364	50	170		88	2.7509E+08
170365	50	170		117	2.7191E+08
170366	60	170		131	3.2202E+08
170367	60	170		130	3.1474E+08
170368	60	170		89	3.1298E+08
170369	70	170		273	3.8551E+08

170370	70	170		93	3.6034E+08
170371	70	170		89	3.7429E+08
170372	80	170		101	4.1966E+08
170373	80	170		161	4.0490E+08
170374	80	170		151	4.1763E+08
170375	90	170		99	4.2034E+08
170376	90	170		164	4.3100E+08
170377	90	170		158	4.4953E+08
170378	100	170		187	4.8056E+08
170379	100	170		189	4.6327E+08
170380	100	170		177	4.6298E+08
Gate Width Scan at 190 ns Delay			**Note**	**Background (pixels)**	**Total Intensity**
170381	10	190		104	7.4987E+07
170382	10	190		84	7.5580E+07
170383	10	190		68	7.6044E+07
170384	20	190		106	1.2729E+08
170385	20	190		156	1.3752E+08
170386	20	190		102	1.3510E+08
170387	30	190		110	1.8283E+08
170388	30	190		114	1.9800E+08
170389	30	190		104	1.8933E+08
170390	40	190		126	2.3851E+08
170391	40	190		142	2.3607E+08
170392	40	190		123	2.3886E+08
170393	50	190		133	2.7432E+08
170394	50	190		133	2.6839E+08
170395	50	190		132	2.6265E+08
170396	60	190		149	3.2191E+08
170397	60	190		151	3.2986E+08
170398	60	190		153	3.0962E+08
170399	70	190		155	3.6441E+08
170400	70	190		160	3.5008E+08
170401	70	190		170	3.5465E+08
170402	80	190		174	3.8591E+08
170403	80	190		170	3.7812E+08
170404	80	190		169	3.9587E+08
170405	90	190		177	4.1574E+08
170406	90	190		175	3.9987E+08
170407	90	190		184	4.0480E+08
170408	100	190		198	4.5122E+08
170409	100	190		190	4.4139E+08
170410	100	190		182	4.4677E+08
170411	10	190		101	7.1800E+07
170412	10	190		92	7.7142E+07
170413	20	190		99	1.2548E+08
170414	20	190		102	1.2320E+08
170415	30	190		108	1.7626E+08
170416	30	190		111	1.8333E+08
170417	40	190		127	2.4501E+08
170418	40	190		124	2.3464E+08
170419	50	190		154	3.0999E+08

170420	50	190		133	2.7973E+08
170421	60	190		148	3.2755E+08
170422	60	190		138	3.2198E+08
170423	70	190		160	3.5665E+08
170424	70	190		153	3.5406E+08
170425	80	190		175	3.6857E+08
170426	80	190		173	4.0717E+08
170427	90	190		181	4.1106E+08
170428	90	190		181	4.2796E+08
170429	100	190		191	4.5061E+08
170430	100	190		183	4.1388E+08

1 March 2012 Shot Log

Accomplishment for this series of shots included:

- Did scans at 3 different velvet positions
- Constant exposure (10 ns) at different delays
- Constant delay (170 ns) with different exposures
- Rotated cable connections to I-20 B-Dot to check a few issues with calibration
- Excited BBU with velvet placement
- Discovered a vacuum leak source in the injector!

Accelerator Tune: Rex06						
New Cathode A-K Gap = 9.44 cm						
Camera F/S: 2.0						
Camera Gain: 255						
Shot #	**Gate**	**Delay (ns)**	**Note**	**I-20 (kA)**	**I-35 (kA)**	**L-44 BBU**
170555	10	170	Warm Up, I20 B-Dot cables in standard configuration		2.85	0.294
170556	10	170	Warm Up		2.84	0.347
First velvet position scan - nominal position, extends out from shroud						
170557	10	170			2.845	0.268
170558	10	170			2.845	0.298
170559	10	180			2.855	0.404
170560	10	180			2.86	0.240
170561	10	190			2.82	0.228
170562	10	190			2.85	0.224
170563	10	200			2.86	0.432
170564	10	200			2.84	0.281
170565	10	210			2.86	0.181
170566	10	210	shifted I20 B-Dot cables, N to U, etc., caused leak	2.91	2.86	0.223
170567	10	220		2.95	2.85	0.412
170568	10	220		2.97	2.87	0.218
170569	60	170		2.90	2.86	0.330
170570	60	170		2.95	2.83	0.336
170571	80	170		2.97	2.84	0.236
170572	80	170		2.93	2.835	0.305
170573	100	170		2.90	2.845	0.251
170574	100	170		3.02	2.845	0.343
170575	10	170		2.88	2.845	0.258
Second velvet position scan - flush to slightly recessed with shroud by 1 turn, 28 turns equal 1 inch						
170576	10	170	Current no longer flat out of injector	2.59	2.74	0.270
170577	10	170		2.54	2.74	0.576
170578	10	180		2.61	2.74	0.449
170579	10	180		2.60	2.74	0.390

170580	10	190		2.51	2.75	0.401
170581	10	190	BBU	2.59	2.76	3.840
170582	10	200	No BBU	2.53	2.76	0.773
170583	10	200		2.58	2.75	0.693
170584	10	210		2.60	2.75	0.523
170585	10	210		2.65	2.75	0.268
170586	10	220		2.44	2.74	0.663
170587	10	220		2.56	2.75	0.493
170588	60	170		2.58	2.75	0.509
170589	60	170		2.55	2.75	0.410
170590	80	170		2.61	2.77	0.343
170591	80	170		2.51	2.75	0.624
170592	100	170		2.58	2.73	0.615
170593	100	170		2.62	2.73	0.601
Third velvet position scan - recessed with shroud by 1 more turn, 28 turns equal 1 inch						
170594	100	170	BBU, double bump to current "flat top"	2.20	2.47	1.410
170595	100	170	Little BBU	2.21	2.44	0.601
170596	80	170		2.31	2.44	0.926
170597	80	170		2.20	2.43	0.471
170598	60	170		2.14	2.43	1.070
170599	60	170		2.21	2.44	1.350
170600	10	170		2.26	2.43	1.460
170601	10	170		2.18	2.42	0.436
170602	10	180	BBU	2.16	2.42	1.660
170603	10	180		2.30	2.42	0.601
170604	10	190		2.20	2.42	0.523
170605	10	190		2.23	2.42	0.969
170606	10	200		2.25	2.42	1.110
170607	10	200		2.26	2.42	1.650
170608	10	210		2.23	2.42	0.961
170609	10	210		2.19	2.42	1.100
170610	10	220		2.22	2.41	0.453
170611	10	220		2.24	2.42	0.327
Returned velvet to original position						
170612	80	170		2.99	2.86	0.317
170613	80	170		2.96	2.86	0.260

Appendix B: Absolute Diagnostic Timing

Time Alignment of I20 B-Dot, I35 BPM, and the Cathode Camera

The schematic below shows the measurements and calculations required to obtain the absolute timing between the three diagnostics. Basically the time for the signals to arrive at the different diagnostics from a fixed reference, Light Off Time or LOT, was calculated on a time of flight. The electrons become relativistic, velocity approximately equal to light, in a very short distance. Next the length of the diagnostic cables for the B-Dot and BPM were measured with a TDR. The

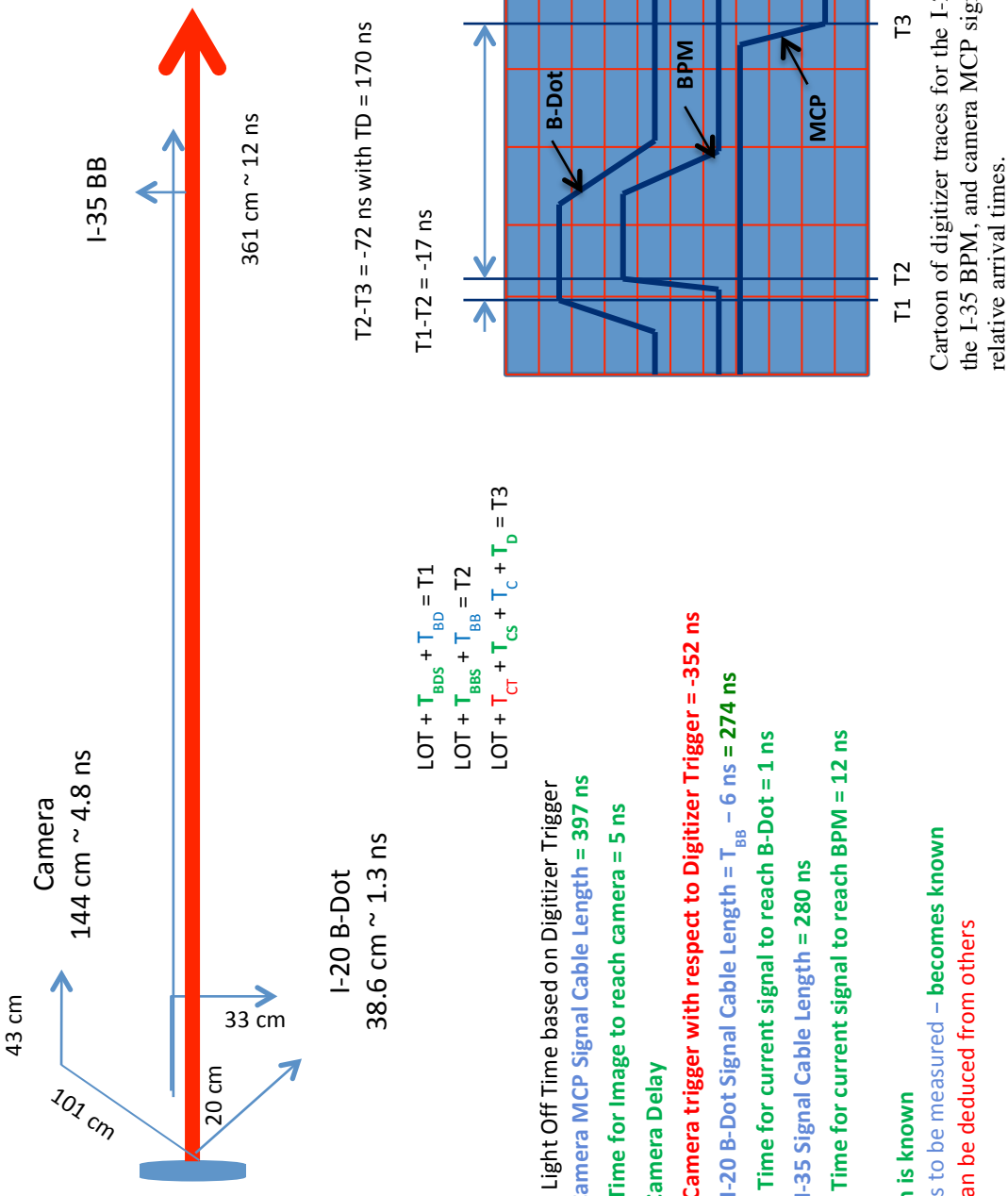

Cartoon of digitizer traces for the I-20 B-D0t, the I-35 BPM, and camera MCP signal shows relative arrival times.

length for the camera's MCP reference signal cable was also measured with the TDR. This reference signal is the time window of the camera exposure and provides the start of the exposure. The one quantity that could not be measured directly was the time between the camera trigger and the trigger for the digitizers that captured the B-Dot and BPM signals. The time of arrival of the BPM signal and the camera MCP reference signal was measured on a scope similar to the cartoon shown in the schematic. These timings were used to produce the below figure.

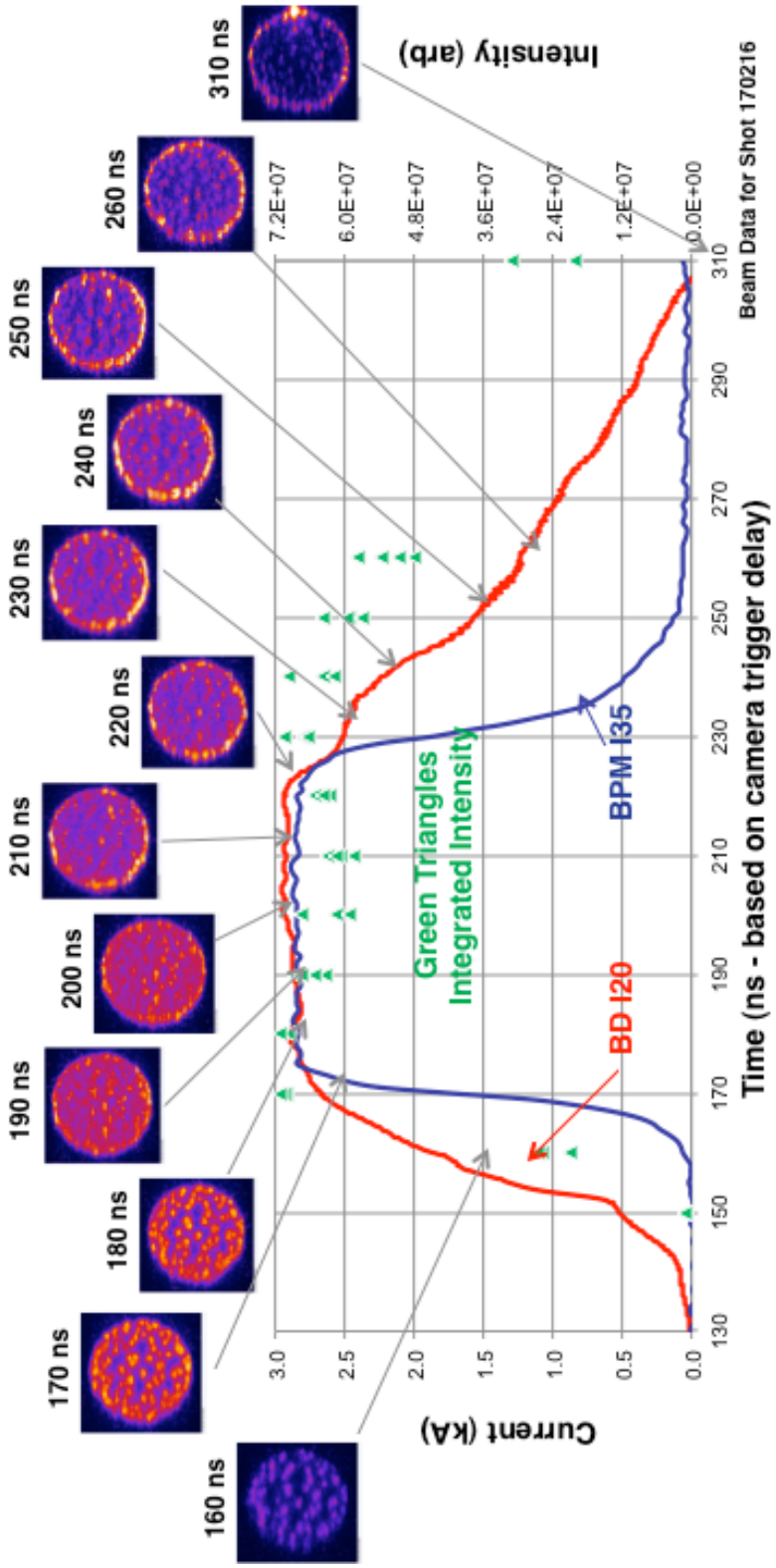

Composite picture showing the current pulse measured at the diode (BD I20), the current pulse measured at the injector exit (BPM I35), cathode images for different camera trigger delay times (all 10 ns exposures) during the current pulse, and the integrated intensity of the cathode images.

Appendix C: B-Dot Operation and Issues

Simplified Equations

The general geometry and definition of terms are shown in Figure C-1. The mechanical axis is perpendicular to the page and the B-Dot diagnostic is located at a radial distance R. The beam axis is parallel to, but offset a distance r from

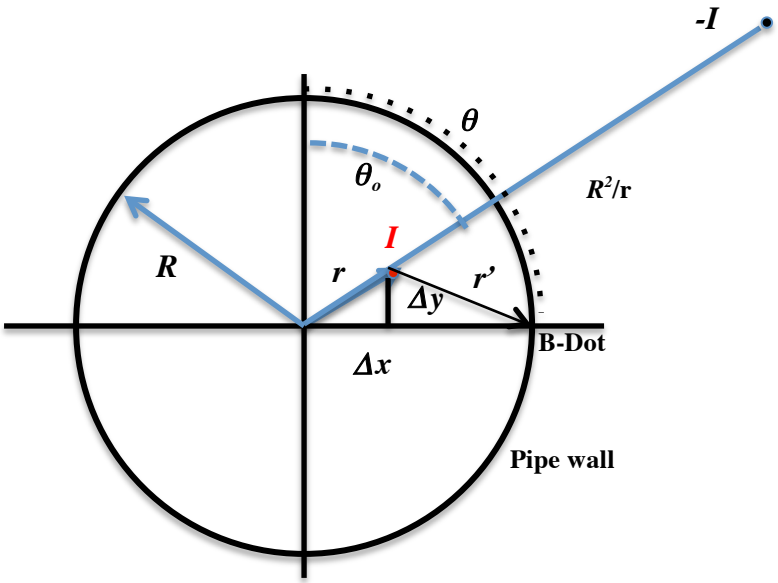

Figure C-1. Definition of quantities used in calculating the magnetic field at the wall of a conducting pipe from a line current are shown graphically in the figure.

the mechanical axis. Neglecting the pipe wall, e.g. a long pulse or dielectric wall, the magnitude of the magnetic field at the B-Dot location is:

$$|B| = \frac{\mu I}{2\pi r'}, \text{ where} \tag{C1}$$

B is the magnetic field located a distance *r*' from the line current I. A little algebra shows that:

$$r' = R\sqrt{1+\rho^2-2\rho\cos(\theta-\theta_0)}, \text{ where } \rho = r/R. \tag{C2}$$

The B-Dot is aligned to be only sensitive to the azimuthal component of the field relative to the mechanical axis. Thus,

$$B_\theta = |B|\frac{R-\Delta x}{r'} = \frac{\mu I}{2\pi r'}\frac{R\left(1-\Delta x/R\right)}{r'} = \frac{\mu I}{2\pi R}\frac{1-\rho\cos(\theta-\theta_0)}{1+\rho^2-2\rho\cos(\theta-\theta_0)}. \tag{C3}$$

For short current pulses and conductive wall as we have on FXR, the magnetic field generates eddy currents that prevent the field from penetrating the wall. The effect of the eddy currents can be modeled as an image current similar to image charges in electrostatic problems. For the magnetic field, the boundary condition is that the field is parallel to the conductive wall. Using this boundary condition, it is straightforward to show that the image current is parallel to, but opposite polarity, as the beam current at a distance of $L = R^2/r$ along the same ray.

The total magnetic field due to the image current at the wall (B_i) is

$$|B_i| = \frac{\mu I}{2\pi L'}, \text{ where } L' = \frac{R}{\rho}\sqrt{1+\rho^2-2\rho\cos(\theta-\theta_0)}. \tag{C4}$$

The azimuthal component for the magnetic field due to the image current at the wall (B_i) is

$$B_{i\theta} = |B_i|\frac{L-\mathrm{R}\cos(\theta-\theta_0)}{L'} = \frac{-\mu I}{2\pi L'}\frac{R\left(1/\rho-\cos(\theta-\theta_0)\right.}{L'} = \frac{-\mu I}{2\pi R}\frac{\rho^2-\rho\cos(\theta-\theta_0)}{1+\rho^2-2\rho\cos(\theta-\theta_0)}. \tag{C5}$$

Adding the two azimual components together gives the total field at the wall,

$$B_{T\theta} = B_\theta + B_{i\theta} = \frac{\mu I}{2\pi R}\frac{1-\rho^2}{1+\rho^2-2\rho\cos(\theta-\theta_0)}. \quad \text{(C6)}$$

Equation (C6) shows that the magnetic field measured at the wall can be related to the current and the displacement of the current from the axis. A convenient method for measuring the magnetic field is with a loop of cross sectional area aligned perpendicular to the field, i.e. by measuring the flux through the loop. There are two unknowns in Equation (6), the current (I), and the displacement (r). The symmetry of the problem requires a minimum of four loops to get a unique solution. *Ekdahl*[i] provides the exact solution for summing over many sets of loops. Below is an approximate solution for only four loops as is used in the FXR B-Dot diagnostic similar to the derivation of *Nye*[ii].

If the beam is reasonably aligned with the mechanical axis so that $r << R$, or $\rho << 1$, Equations (C3) and (C6) can be simplified by only keeping terms to first order in ρ. Using the approximation $(1\text{-a})^{-1} \sim 1 + \text{a}$ when $a<<1$,

$$B_\theta \approx \frac{\mu I}{2\pi R}\left(1+\rho\cos(\theta-\theta_0)\right) \text{ neglecting wall effects, and} \quad \text{(C7)}$$

$$B_{T\theta} \approx \frac{\mu I}{2\pi R}\left(1+2\rho\cos(\theta-\theta_0)\right) \text{ including wall effects.} \quad \text{(C8)}$$

Using Faraday's Law of Induction, the voltage developed around a B-Dot loop is

$$V = \frac{\partial(\vec{B}\cdot\vec{A})}{\partial t} = A\frac{\partial B}{\partial t} \text{ (if the loop area remains constant and is perpendicular to the field),} \quad \text{(C9)}$$

where A is the cross sectional area of the loop. Refer to the *Ekdahl* and *Nye* for details and limitations in the derivation. The measurement of the voltage should be into high impedance so that negligible current flows through the device and self-inductance and resistive loses will not add significant errors. In our case we have four loops located every 90° azimuthally around the beam line such that

$$V_{+x} = A\frac{\partial B_{T\theta}(\theta_0)}{\partial t}, V_{+y} = A\frac{\partial B_{T\theta}(\theta_0-\pi/2)}{\partial t}, V_{-x} = A\frac{\partial B_{T\theta}(\theta_0-\pi)}{\partial t}, \text{ and } V_{-y} = A\frac{\partial B_{T\theta}(\theta_0+\pi/2)}{\partial t}. \quad \text{(C10)}$$

$$\text{Let } \Sigma = \int V_{+x}dt + \int V_{-x}dt + \int V_{+y}dt + \int V_{-y}dt\,, \Delta_x = \int V_{+x}dt - \int V_{-x}dt\,, \text{ and, } \Delta_y = \int V_{+y}dt - \int V_{-y}dt\,. \quad \text{(C11)}$$

Combining Equations (C7) through (C11):

$$\Sigma = \frac{2A\mu I}{\pi R}, \text{ or I} = \frac{\pi R}{2A\mu}. \quad \text{(C12)}$$

Note that Equation (C12) is true whether or not the wall is included as the ρ terms cancel. This is not the case when you look at the differences. Considering the wall, i.e. Equation (C8),

$\Delta_x = \frac{2A\mu I}{\pi R}\rho\cos(\theta_0) = \frac{2A\mu I}{\pi R^2}\Delta x = \frac{\Sigma}{R}\Delta x$, and $\Delta_y = \frac{2A\mu I}{\pi R}\rho\sin(\theta_0) = \frac{2A\mu I}{\pi R^2}\Delta y = \frac{\Sigma}{R}\Delta y$, or rearranging,

$$\Delta\text{x} = R\frac{\Delta_x}{\Sigma} \text{ and } \Delta\text{y} = R\frac{\Delta_y}{\Sigma}. \text{ (wall included)} \quad \text{(C13)}$$

Using Equation (C7) the result becomes $\Delta\text{x} = 2R\frac{\Delta_x}{\Sigma}$ and $\Delta\text{y} = 2R\frac{\Delta_y}{\Sigma}$. (wall not included). (C14)

Issues: Clocking, Location, and Cable Connections

There are a number of issues that complicate the use of the I-20 B-Dot diagnostic: clocking, location, and cabling. Clocking is the easiest problem to compensate. Mechanical considerations led to the B-Dot probes not being aligned with the mechanical Top/Bottom and North/South coordinates of the accelerator as shown in the Figure C-2. The loops are spaced at 90° intervals. However, the clocking is 12.5° off of vertical/horizontal. Thus,

$$X_H = \Delta x\cos\phi + \Delta y\sin\phi \text{ and } Y_V = -\Delta x\sin\phi + \Delta y\cos\phi\,, \quad \text{(C15)}$$

where ϕ is 12.5°, X_H and Y_V are the beam's displacements in the accelerator's vertical and horizontal coordinates.

The location of the B-Dot presents some obvious difficulties and a subtle problem. First, the B-Dot is located on the radial (side) wall of the Injector Spool as shown in Figure 2-7. Thus the actual geometry is different than that used for Equations (C12) and (C13). The image current due to the outer wall needs to be included, but the magnetic field needs to be calculated at a location $R_p < R$.

Making a few new definitions:
R_p is the radial distance to the probe, $\rho_p = {}^{r}/_{R_p}$ is ratio of the centroid displacement to the probe's radial distance, and $R' = {}^{R_p}/_{R} \leq 1$. The magnetic field, after considerable algebra and geometry similar to what was done before, can be expressed as:

$$B_{T\theta} = \frac{\mu I}{2\pi R_p} \frac{\left[1-R'^2\rho_p^2\right]\left[\frac{1}{R'}\left(1+\frac{1}{R'^2\rho_p^2}\right)-\frac{\left(R'^2+1\right)}{R'\rho_p}\cos(\theta-\theta_0)\right]}{R'\left[1+\rho_p^2-2\rho_p\cos(\theta-\theta_0)\right]\left[1+\frac{1}{R'^4\rho_p^2}-\frac{2}{R'\rho_p}\cos(\theta-\theta_0)\right]}, \text{ or (C16)}$$

$$B_{T\theta} = \frac{\mu I}{2\pi R} \frac{\left[1-\rho^2\right]\left[\frac{1}{R'}\left(\rho^2+1\right)-\left(R'^2+1\right)\rho\cos(\theta-\theta_0)\right]}{\left[R'^2+\rho^2-2\rho R'\cos(\theta-\theta_0)\right]\left[\rho^2+\frac{1}{R'^2}-2\rho\cos(\theta-\theta_0)\right]}. \quad \text{(C17)}$$

For the FXR I-20 B-Dot where R' = 34/36.7 = 0.93, this is a small correction compared to other effects.

The individual rf loops of the B-Dot are recessed into the wall as shown in Figure 2-7. A greater issue is that the loops are positioned over the anode stalk and along a radial, conductive wall. 3-dimensional simulations of the injector vacuum spool were performed to study the effect of asymmetrically located access ports on the magnetic field at the location of the rf loops. Refer to Figure C-3 for the simulated geometry. The beam was modeled as a solid rod carrying a current, I, that was parallel to, but displaced transversely from the mechanical axis. Due to the physical volume modeled, the grid was limited to 2.5-mm sided cubes. Checks of the code[iii] were performed in a simple coaxial arrangement against Equation (C8) at better than 1% accuracy for current and better than 2% accuracy in displacement. The access ports were found to have negligible effect on the field at the loops. The average field outside of the recessed ports for the rf loops, the sum term from Equation (C12), provided an accurate calculation of the current. However, the difference term for calculating the displacement produced values less than 25% of the actual displacement. Removing the anode stalk from the simulation improved the displacement calculation by a factor of 1.6 to about 43% of the correct value. The discrepancy is due to the asymmetrical return currents flowing azimuthally on radial surfaces to minimize the asymmetry. The simulation results will be used to correct for this factor.

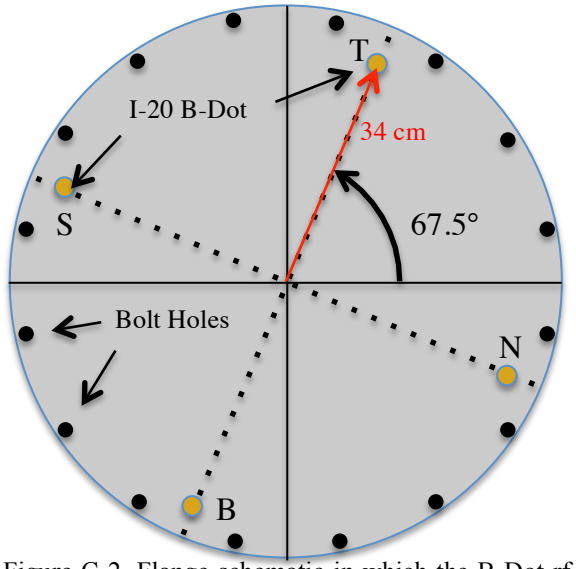

Figure C-2. Flange schematic in which the B-Dot rf loops are embedded showing rotation and position notation with respect to accelerator coordinates.

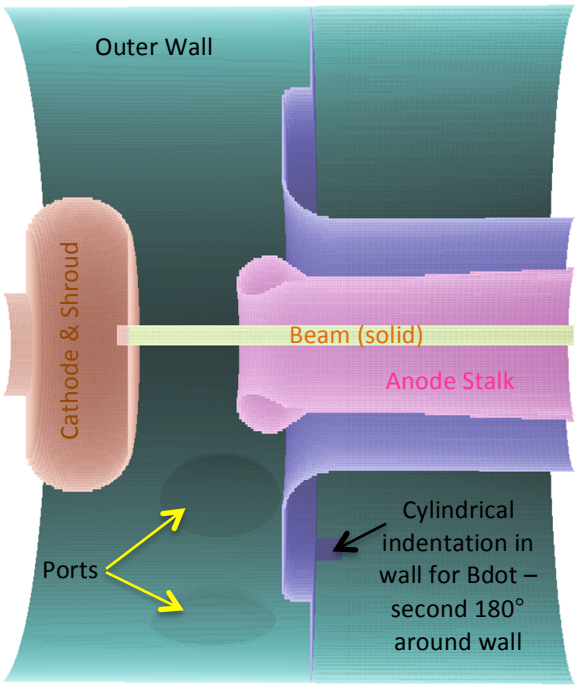

Figure C-3. Cut view of 3-dimensional simulation used in modeling beam generated magnetic field.

The shape of the injector spool resembled a cylindrical microwave resonator as shown in Figure 2-7. An off-centered beam acts as a driving signal for the higher order resonances. In particular, the TM_{1m0} transverse magnetic mode[iv] has an azimuthal field structure that varies as:

$$B_\theta \sim J_1'\left(\frac{p_{1m}\, r}{R}\right)\cos\theta, \text{ with frequency } f = \frac{c\, p_{1m}}{2\pi R}, \text{ where} \quad \text{(C18)}$$

m is an index, p_{1m} are the zeros of the first Bessel function (J_1), R is the resonator radius, J_1' is the derivative of the first Bessel function, and c is the speed of light. This signal will be detected by the rf loops in addition to the beam generated magnetic field. Substituting R = 3.67 cm the resonant frequencies are:

f = 498 MHz, 913 MHz and 1.324 GHz for m = 1, 2 , and 3

Note that there is no contribution to the loop sum, Equation (C11), used for calculating the current as the TM_{1m0} signal has reversed polarity on opposing loops and cancels. Unfortunately, the difference of the TM_{1m0} signal on opposing

loops add together generating a large, fast oscillation on the desired beam displacement signal. Figure C-4 shows plots of the difference and sums of the "North" and "South" RF Loops of the I-20 B-Dot as well as the integrated quantities. Adding the signals does reduce the magnitude, but does not achieve a cancellation. Fortunately, integration acts as a filter significantly reducing the resonant cavity effect on the integrated sum used for calculating total beam current (purple curve). The integrated difference (red curve) divided by the integrated sum is proportional to the beam centroid displacement as described in Equation (C13).

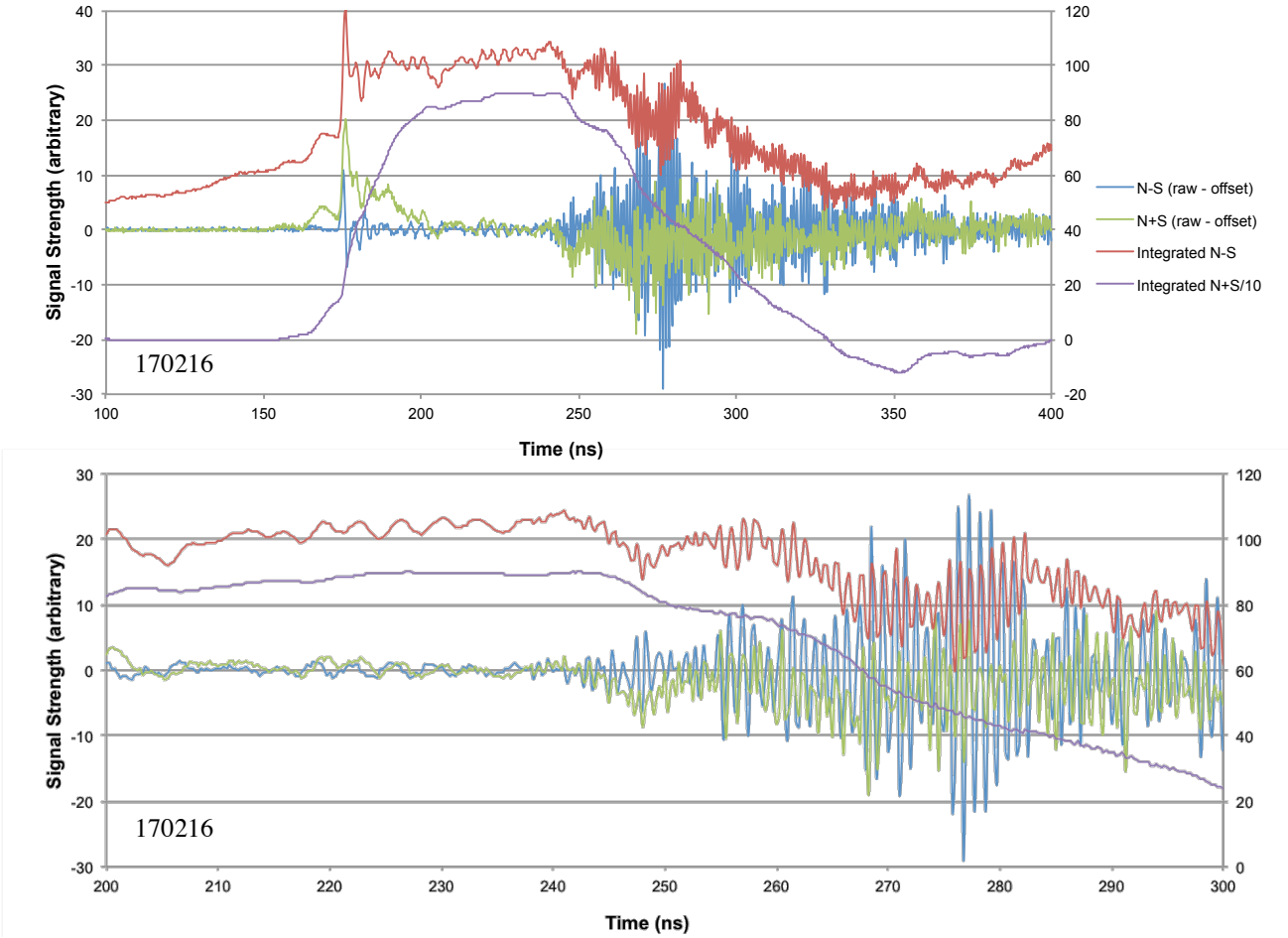

Figure C-4. Plots of the difference and sum of the I-20 B-Dot North and South RF loops with time integrated signals. Top graph covers time of entire current pulse and bottom graph is expanded time view.

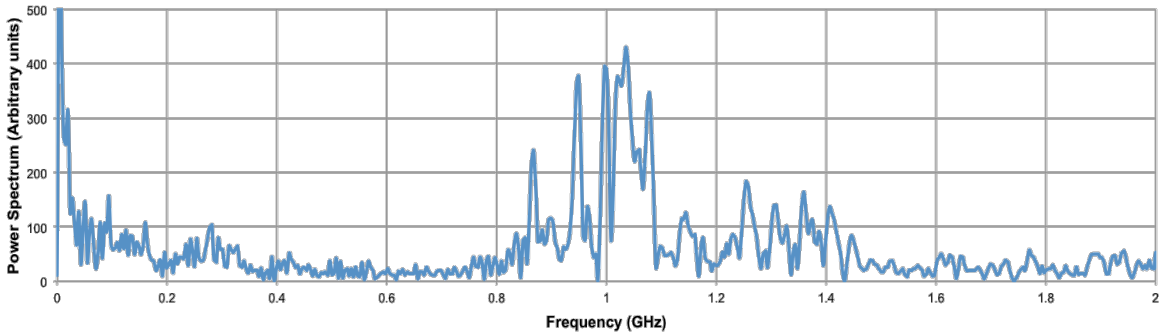

Figure C-5. The Fourier Power Spectrum is plotted for the North RF Loop signal on shot 170216.

The non-canceling of the fast oscillation (approximately 1GHz ringing) on the RF Loop difference signal is due to a number of things. The injector spool is a much more complicated geometry than a simple cylindrical resonator and there are complex hybrid resonances in addition to transverse electric and magnetic resonances. Figure C-5 is the Fourier

Transform Power Spectrum of the "North" RF Loop. There are a number of frequency peaks near 1 GHz as well as a smaller set between 1.2 – 1.4 GHz. The time resolution of the digitized signals is also a source of error when combining these relatively high frequency signals. The digitizers used for the study stored the data in 250 ps intervals. That resolution equates to only 4 data points in a 1 GHz cycle or about 2 cm wavelength in the diagnostic cable. Adding a small component, e.g. an elbow, to one of the diagnostic cable runs would shift it sufficiently in phase that the cancelation would not occur when the signals were added in software. Combining the signals before digitizing as is done for the BPM's and B-Dots used in the BBU diagnostic system avoids the digitizer bandwidth problem. Constructing cables and hardware to match the RF Loop signal path lengths can be done with sufficient accuracy.

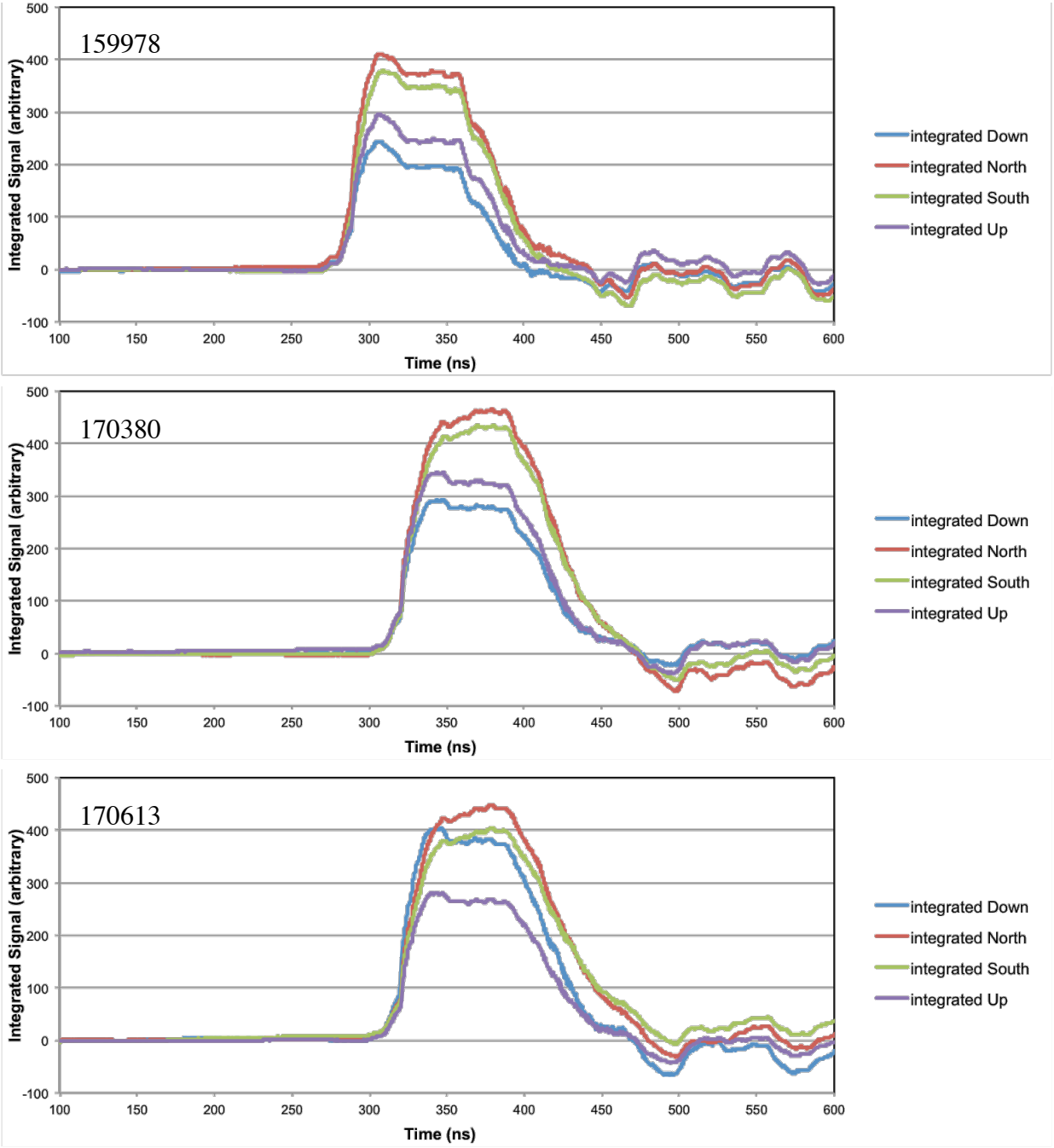

Figure C-6. Plots of the integrated RF Loop signals are shown for three different pulses taken on different days.

The connection of the diagnostic cables to the B-Dot RF loops is the final familiarity issue to be discussed. The integrated signals from each of the four RF loops are shown in Figure C-6. Three different cases are shown: shot

#159978 taken 4/11/07, shot #170380 taken 2/18/12, and shot #170613 taken 3/1/12. Shot #159978 was taken shortly after the installation of the new cathode[v] with smaller diameter velvet emission area. Shot #170380 was taken nearly five years later and about half way through this study. The relative maximums of the respective set of integrated loop signals are similar although there is a noticeable difference in pulse shape for the North and South loops. The cases shown are representative of the signals taken for similar operational conditions during the same period of time, i.e. these signals are not unique. The diagnostic cables were switched, as will be described below, for a series of pulses including #170613. There are two puzzling features regarding these signals.

1. The signals should be proportional to the beam current, so it is not reasonable that the North and South loops have a different shape than the Up and Down loops for #170380 and shot #170613.
2. Since the signals are proportional to the current and the hardware (rf loops) are identical, all of the signals should have approximately the same magnitude unlike what was measured.

One explanation for the puzzle was that the diagnostic lines and/or digitizers were different for some/all signals. A check of the equipment did not show damaged cables, nonstandard rf components, or unusual digitizing hardware. A second check involved rotating the diagnostic lines with respective to the RF loops: Upper loop came back on the North Line, the South Loop came back on the Upper Line, etc. The results after rotating the lines were not encouraging as shown for the 170613 plot. Instead of seeing the expected general reversal of North/South with Up/Down, the North and South remained essentially the same with slightly lower magnitude. Thus the new expectation was that the diagnostic lines were very similar and the UP/Down signals would remain the same with possibly slightly higher magnitudes. Instead the Down magnitude increased significantly while the Up decreased.

The conclusion was that the problem occurred with the mating of the diagnostic line with the RF loops. There is no easy way of correcting the problem other than rebuilding the connectors on the cables and/or RF loops. The B-Dot can be used for relative measurements between pulses where the connections have not been disturbed, but cannot be used between pulses where the connections have been disturbed or for absolute measurements. A procedure for properly mating the connections including torque requirements is required.

---

[i] C. A. Ekdahl, "Fourier analyzing coil arrays for pulsed relativistic electron beam experiments," Rev. Sci. Instrum. 55, 1221 (1984)

[ii] H.L. Nye, "Experimental Analysis of B-Dot Sensors," MS Dissertation, Naval Post Graduate School, June 1990

[iii] **Magnum** is part of the **Advanced Charged-particle Design Suite** marketed by **Field Precision LLC,** PO Box 13595, Albuquerque, New Mexico 87192 U.S.A., http://www.fieldp.com/magnum.html

[iv] O.P. Gandhi, *Microwave Engineering and Applications*, Pergamon Press, New York, 1981, pp. 248-250.

[v] T.L. Houck, et al., "Design of a High Field Stress, Velvet Cathode for the Flash X-Ray (FXR) Induction Accelerator," Proceedings 2007 Particle Accelerator Conference, Albuquerque, NM, June 25-29 2007 (UCRL-PROC-231690)

Appendix D: Diode Photographs

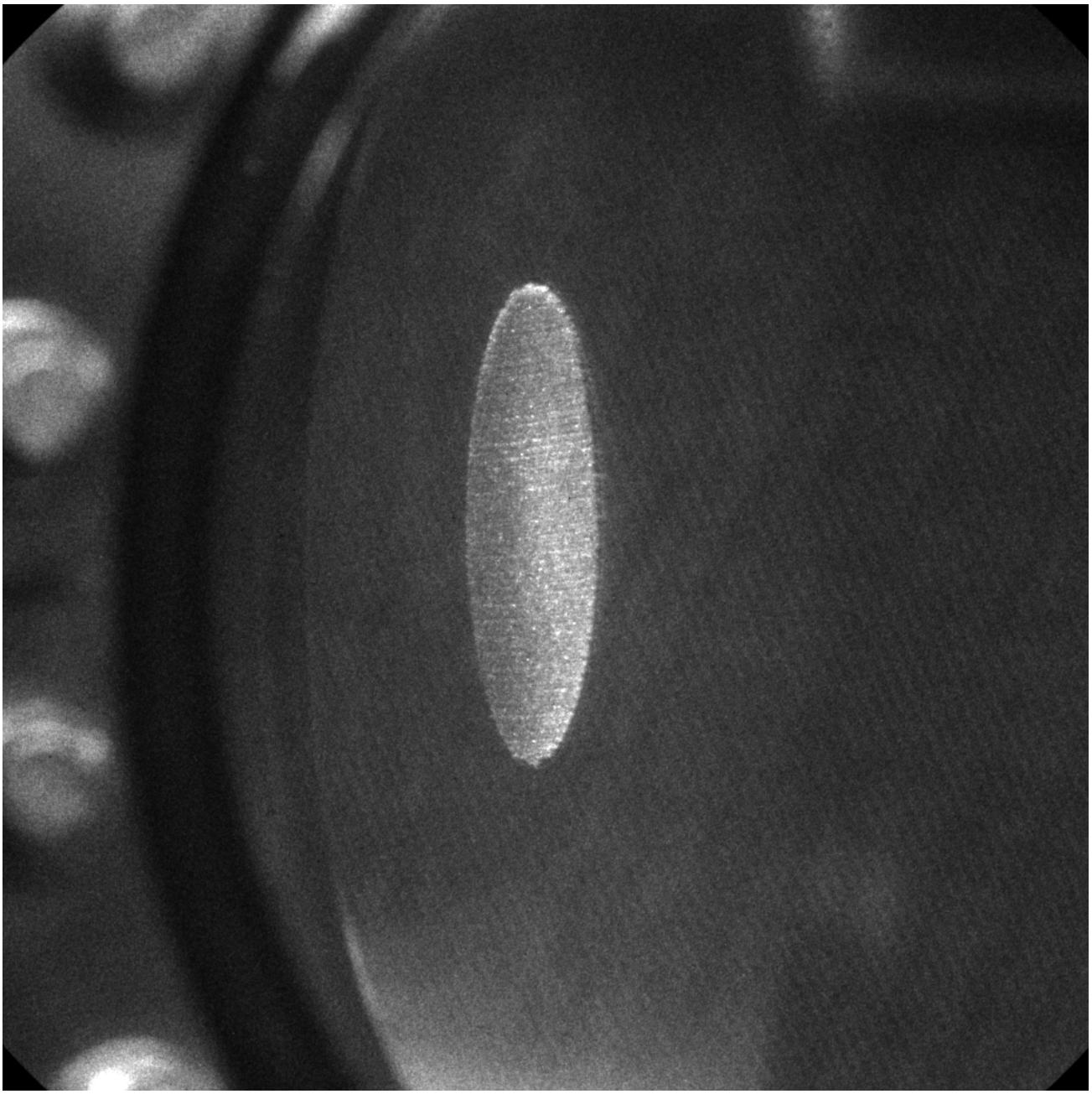

Figure D-1. Picture is a cathode image using front lighting, f/16, and 6 ms exposure. This image was taken to establish mechanical center. Image is for Extend case where velvet protrudes about 1 mm beyond cathode shroud. The pattern visible on the shroud is due to the screen over the interior of the port used for return currents.

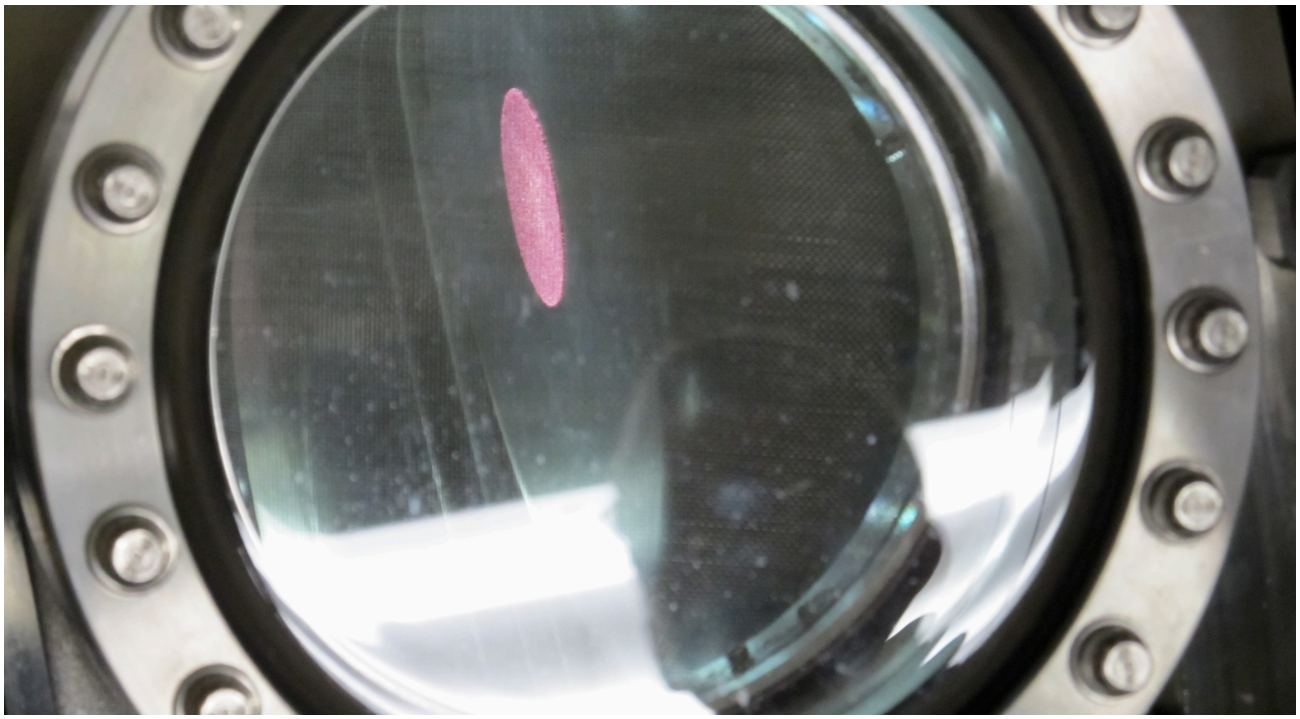

Figure D-2. View through injector vacuum spool looking at the cathode. Velvet is extended approximately 1 mm above the plane of the cathode shroud. The edge of the velvet is visible.

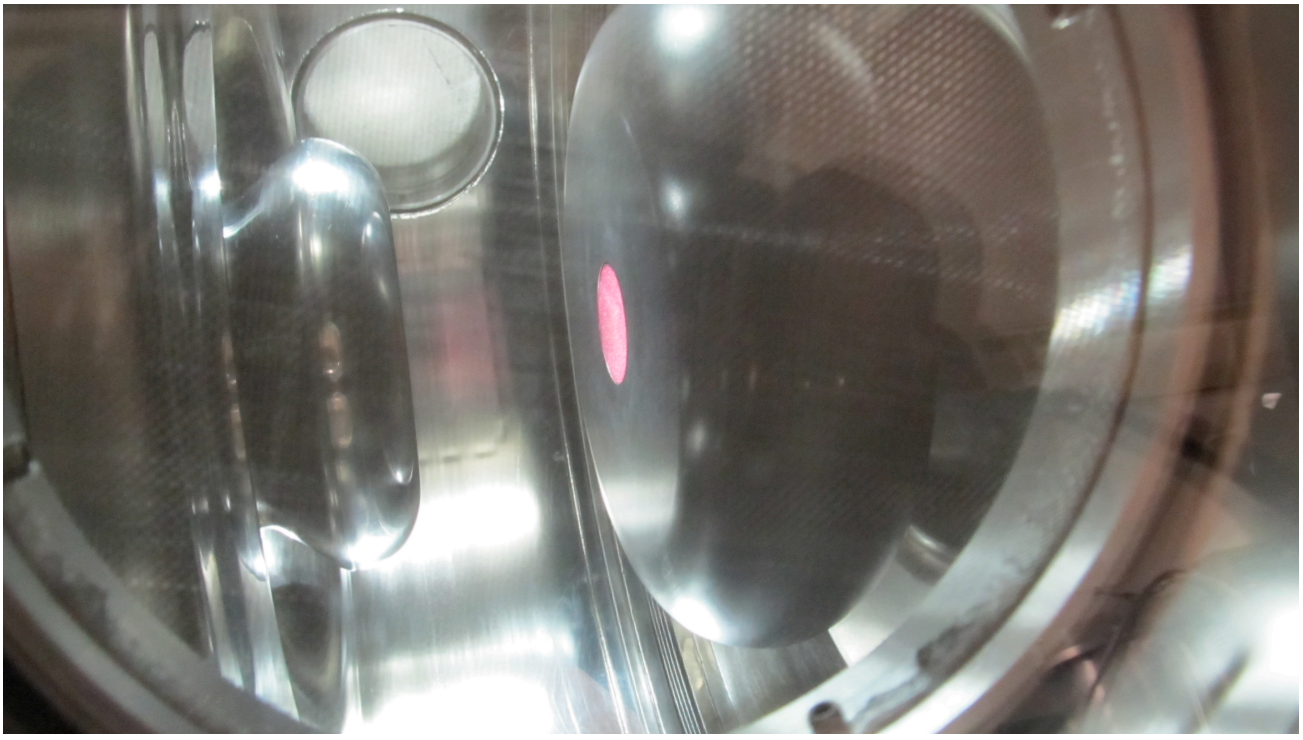

Figure D-3. View through injector vacuum spool looking at the cathode. Velvet is approximately flush with the plane of the cathode shroud.

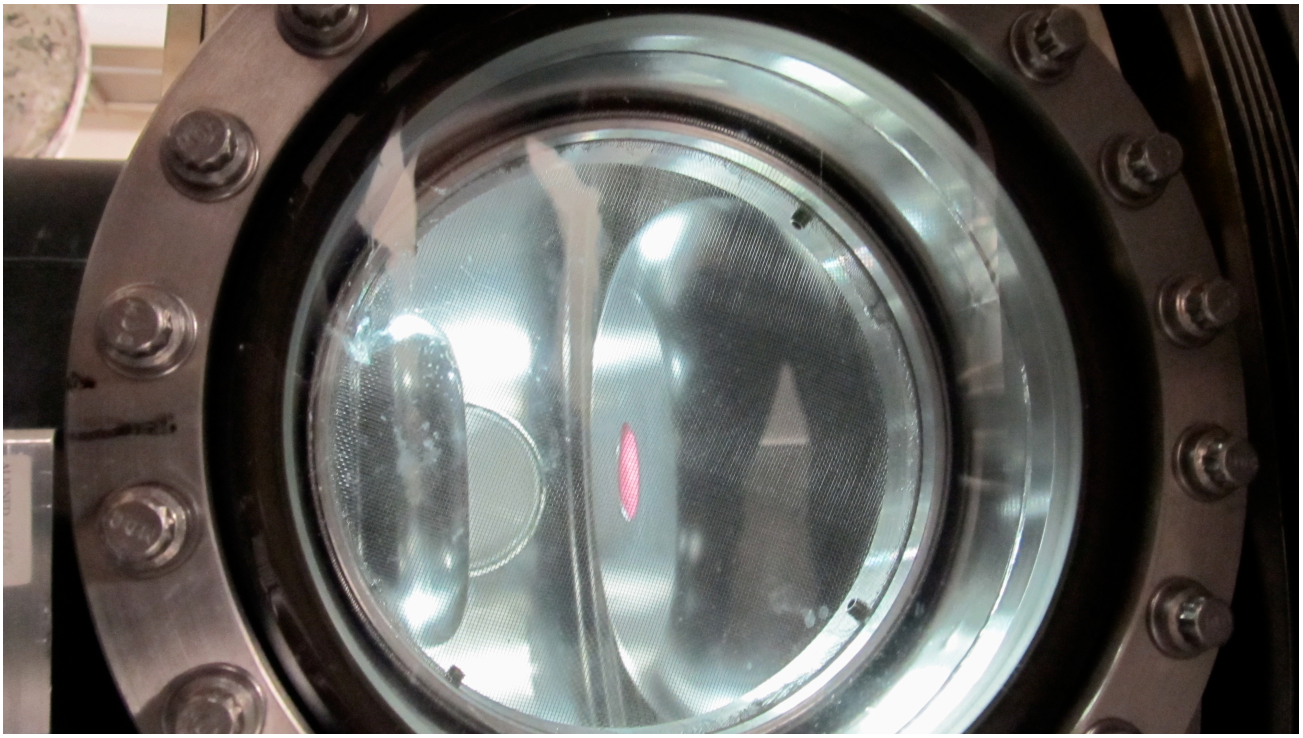

Figure D-4. View through injector vacuum spool looking at the cathode. Velvet is recessed approximately 1 mm below the plane of the cathode shroud. The interior edge of the cathode is visible.

Appendix E: Voltage versus Current (Perveance)

Child's Law or space charge limited current density is often cited to say that the emitted current varies as the diode voltage to the 3/2. However, Child's Law and the 3/2 dependency is for non-relativistic beams. For ultra relativistic beams the current is proportional to the voltage. The FXR beam is relativistic by the time it crosses the AK gap. The relativistic factor γ for electrons can be defined as (total energy = rest energy + kinetic energy):

$$\gamma = 1 + \frac{eV}{m_e c^2} = 1 + \frac{V_d}{0.511}, \text{ where} \tag{E1}$$

eV is the kinetic energy, $m_e c^2$ is the electron's rest energy, and V_d is the diode voltage in MV. Depending on the precision and application, an electron is considered relativistic when its γ is 2 to 4, or 0.5 MeV to 1.5 MeV. From simulations performed for the FXR injector, the current varies somewhat less than $V^{3/2}$. For a very readable reference on space charge limited emission including the assumptions used in deriving Child's Law see Stan Humphries' *Charged Particle Beam*[li], pages 195-200 for non-relativistic beams and pages 242-246 for relativistic beams. Fitting calculated values, the space charge limited current density for 0.5 MV to 10 MV electron beams is approximately,

$$j_e \approx \left[\frac{2\varepsilon_o m_e c^3}{e d^2}\right]\left[\left(1 + \frac{eV_d}{m_e c^2}\right)^{1/2} - 0.8471\right]^2, \text{ where} \tag{E2}$$

d is the gap distance. Note that the theory is for the current density, not the current. You need to multiply by the emission area to get the current. Substituting for the physical constants,

$$j_e \approx \frac{2.71(\text{kA})}{d^2}\left[\left(1 + \frac{V_d}{0.511}\right)^{1/2} - 0.8471\right]^2, \text{ where } V_d \text{ is in MV.} \tag{E3}$$

The current from a circular emission area of radius r is then,

$$I \approx \frac{\pi r^2}{d^2} 2.71\left[\left(1 + \frac{V_d}{0.511}\right)^{1/2} - 0.8471\right]^2 (\text{kA}). \tag{E4}$$

Assuming I = 3 kA, r = 2.9 cm, and V_d = 2.5 MV, the effective AK gap, d = 7.7 cm. The non-relativistic Child's Law produces d = 9 cm and the physical spacing between the shroud and anode is 9.44 cm. There is likely a reasonable amount of uncertainty in both I and V_d. However, these values should be good for estimating the sensitivity of the perveance to plasma expansion and velvet position.

[li] S. Humphries, Jr., **Charged Particle Beams**, John Wiley and Sons, 1990 – free electronic version can be down loaded at http://www.fieldp.com/educa.html.

Appendix F: Simulations of Spotty Emission

Simulations of beam emission

The geometry of the FXR diode region was simulated in four steps. The first was an electrostatic model of the region out to the full radius of the spool containing the diode of about 37 cm to determine the electric field in the accelerating gap. The minimum grid size was limited by available computer memory, although more than sufficient for determining the field. However, a finer grid was required for modeling the emission surface and beam transport. A second simulation was performed out to a radius of 19 cm and used the electric field calculated in the first simulation as the boundary field. A separate magnetostatic simulation was performed to generate the solenoidal magnetic focusing fields used in the FXR injector. These fields were used in the 3-Dimensional particle initiation, orbital tracking code, OmniTrak, to simulate the flat top portion of the injector electron beam. The generated beam properties were then calculated. A cut away view of a sample simulation showing the cathode shroud, anode, and generated beam is shown in Figure F-1. The emission patterns of the 18 cases used for the simulated analysis are shown below with pertinent parameters.

Figure F-1. Cutaway view of the simulated FXR injector diode with beam.

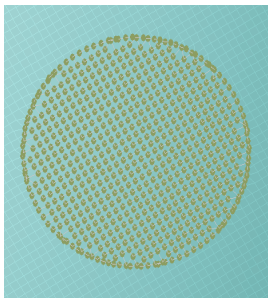

Base case for reference. Used uniform circle for emitter surface so that number of emission sites was determined by simulation grid:
2,760: emitting points
29.23 cm^2: emission area
3.396 kA: total current emitted
6.0 cm-mr: emittance
6.0 cm-mr: scaled emittance

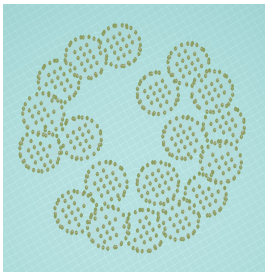

Case 19-1, this is a form of Case 23-7 (refer to below) where four of the original 23 spots were removed:
2,216: emitting points
21.55 cm^2: emission area
3.078 kA: total current
15.6 cm-mr: emittance
16.4 cm-mr: scaled emittance

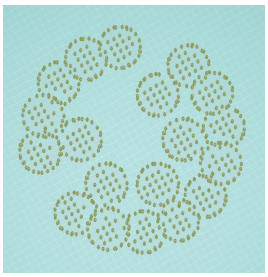

Case 20-1, this is a form of Case 23-7 (refer to below) where three of the original 23 spots were removed:
2,328: emitting points
22.73 cm^2: emission area
3.162 kA: total current
14.0 cm-mr: emittance
14.5 cm-mr: scaled emittance

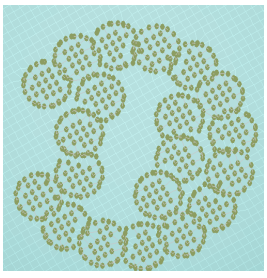

Case 20-2, this is a form of Case 24-0 (refer to below) where four of the original 24 spots were removed:
2,328: emitting points
22.54 cm^2: emission area
3.142 kA: total current
13.6 cm-mr: emittance
14.1 cm-mr: scaled emittance

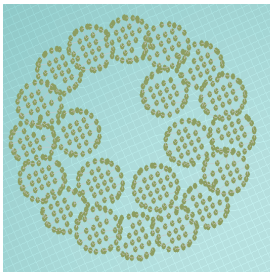

Case 21-1, this is a form of Case 23-7 (refer to below) where two of the original 24 spots were removed:
2,424: emitting points
23.83 cm^2: emission area
3.244 kA: total current
13.0 cm-mr: emittance
13.3 cm-mr: scaled emittance

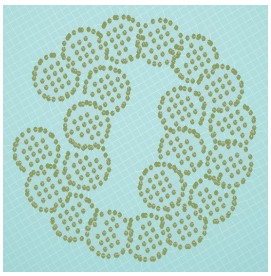

Case 21-2, this is a form of Case 24-0 (refer to below) where three of the original 24 spots were removed:
2,508: emitting points
24.80 cm^2: emission area
3.249 kA: total current
11.6 cm-mr: emittance
11.9 cm-mr: scaled emittance

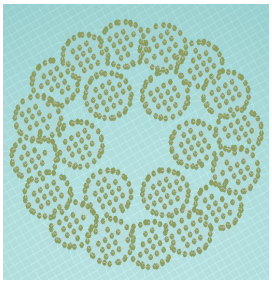

Case 22-1, this is a form of Case 23-7 (refer to below) where the center spot of the original 24 spots was removed:
2,576: emitting points
25.32 cm^2: emission area
3.321 kA: total current
11.2 cm-mr: emittance
11.3 cm-mr: scaled emittance

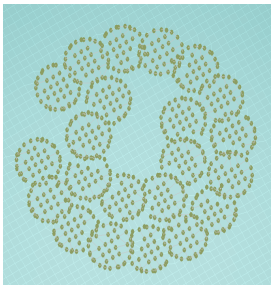

Case 22-2, this is a form of Case 24-0 (refer to below) where two of the original 24 spots were removed:
2,652: emitting points
26.25 cm^2: emission area
3.308 kA: total current
10.7 cm-mr: emittance
10.8 cm-mr: scaled emittance

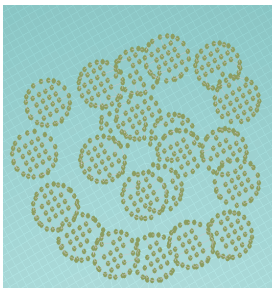

Case 22-R1, this is a form of Case 24-R2 (refer to below) where two of the original 24 spots were removed:
2,388: emitting points
22.93 cm^2: emission area
3.238 kA: total current
15.4 cm-mr: emittance
15.8 cm-mr: scaled emittance

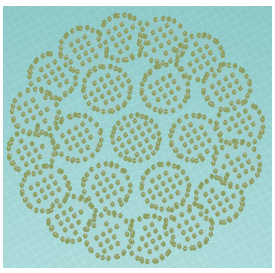

Case 23-7, symmetric and relatively uniformly filled:
2,760: emitting points
27.05 cm^2: emission area
3.396 kA: total current
8.6 cm-mr: emittance
8.6 cm-mr: scaled emittance

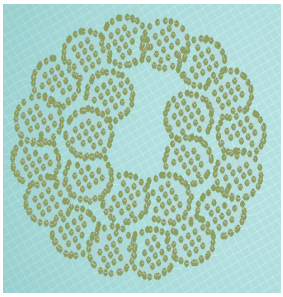

Case 23-10, this is a form of Case 24-0 (refer to below) where one of the original 24 spots was removed:
2,768: emitting points
27.46 cm^2: emission area
3.385 kA: total current
9.4 cm-mr: emittance
9.4 cm-mr: scaled emittance

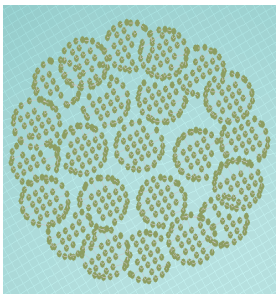

Case 23-R3, this is a form of Case 23-7 (refer to above) where several of the original 23 spots were shifted randomly by 1 mm in x and/or y (note that no spots overlapped):
2,680: emitting points
26.27 cm^2: emission area
3.333 kA: total current
9.7 cm-mr: emittance
9.8 cm-mr: scaled emittance

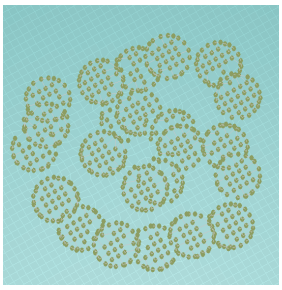

Case 23-R5, this is a form of Case 24-R2 (refer to below) where one of the original 24 spots was removed:
2,448: emitting points
23.36 cm^2: emission area
3.263 kA: total current
15.6 cm-mr: emittance
15.9 cm-mr: scaled emittance

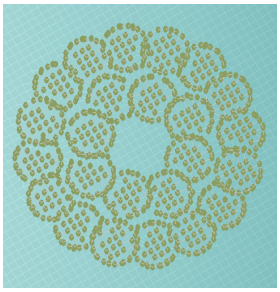

Case 24-0, symmetric and relatively densely filled even with center hole (note that the emission area is greater than for 23-7):
2,928: emitting points
29.17 cm^2: emission area
3.488 kA: total current
8.0 cm-mr: emittance
7.9 cm-mr: scaled emittance

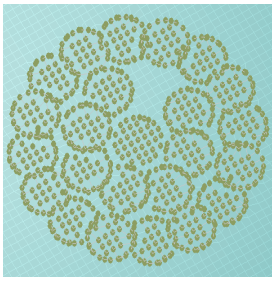

Case 24-A1, this is a form of Case 24-0 (refer to above) where one of the original 24 spots was moved to fill in center:
2,948: emitting points
29.34 cm^2: emission area
3.450 kA: total current
7.6 cm-mr: emittance
7.5 cm-mr: scaled emittance

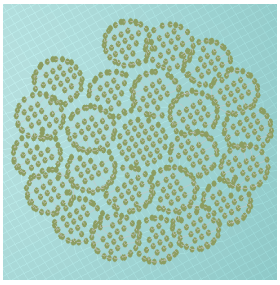

Case 24-A2, this is a form of Case 24-0 (refer to above) where one of the original 24 spots was moved to fill in center:
2,948: emitting points
29.34 cm^2: emission area
3.450 kA: total current
7.6 cm-mr: emittance
7.5 cm-mr: scaled emittance

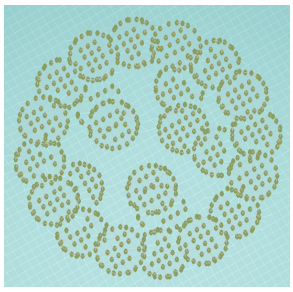

Case 24-R1, this is a form of Case 24-0 (refer to above) where interior spots were shifted randomly by 5 mm in x and/or y from the original 24 spot locations:
2,564: emitting points
25.13 cm^2: emission area
3.312 kA: total current
9.8 cm-mr: emittance
9.9 cm-mr: scaled emittance

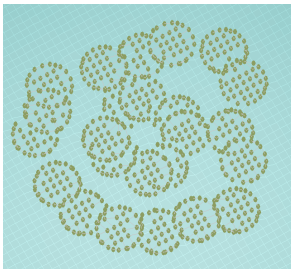

Case 24-R2, this is a form of Case 24-0 (refer to above) where interior and exterior spots were shifted randomly by 5 mm in x and/or y from the original 24 spot locations:
2,492: emitting points
23.74 cm^2: emission area
3.280 kA: total current
15.8 cm-mr: emittance
16.1 cm-mr: scaled emittance

Appendix G: Geometry of the Camera View

A simplified sketch of the cathode as viewed by the camera is shown in Figure G-1. The camera lens system and mirror are ignored in this example. The most important feature of the sketch is demonstrating how the effective center position of the cathode shifts in the horizontal as the velvet is moved longitudinally. Figure G-2 illustrates how dimensions were taken from the front-lit cathode photograph and converted into pixels per mm. By comparing the height (vertical dimension) of the velvet where the diameter is not subject to foreshortening to the width (horizontal) the viewing angle, α, can be calculated. This value is used to scale the image generating a pseudo normal view where the cathode image looks circular. α is also used to calculate the apparent translation of the image center in the horizontal as the velvet is moved along the beam axis. A second effect involving the movement of the velvet along the beam axis is that the edge of the velvet becomes visible when the velvet extends past the shroud cathode surface. To ensure that the surface area of the velvet used in the analysis of the FOM is consistent for the different velvet placement, the ROI for the analysis needs to exclude edge effects. Refer to Figures G-2 b and c. A similar problem occurs when the velvet is retracted below the surface of the shroud. For this case part of the velvet surface is not visible. Unfortunately there is no technique to create the hidden information, but a retracted cathode is not a normal or desirable operational condition.

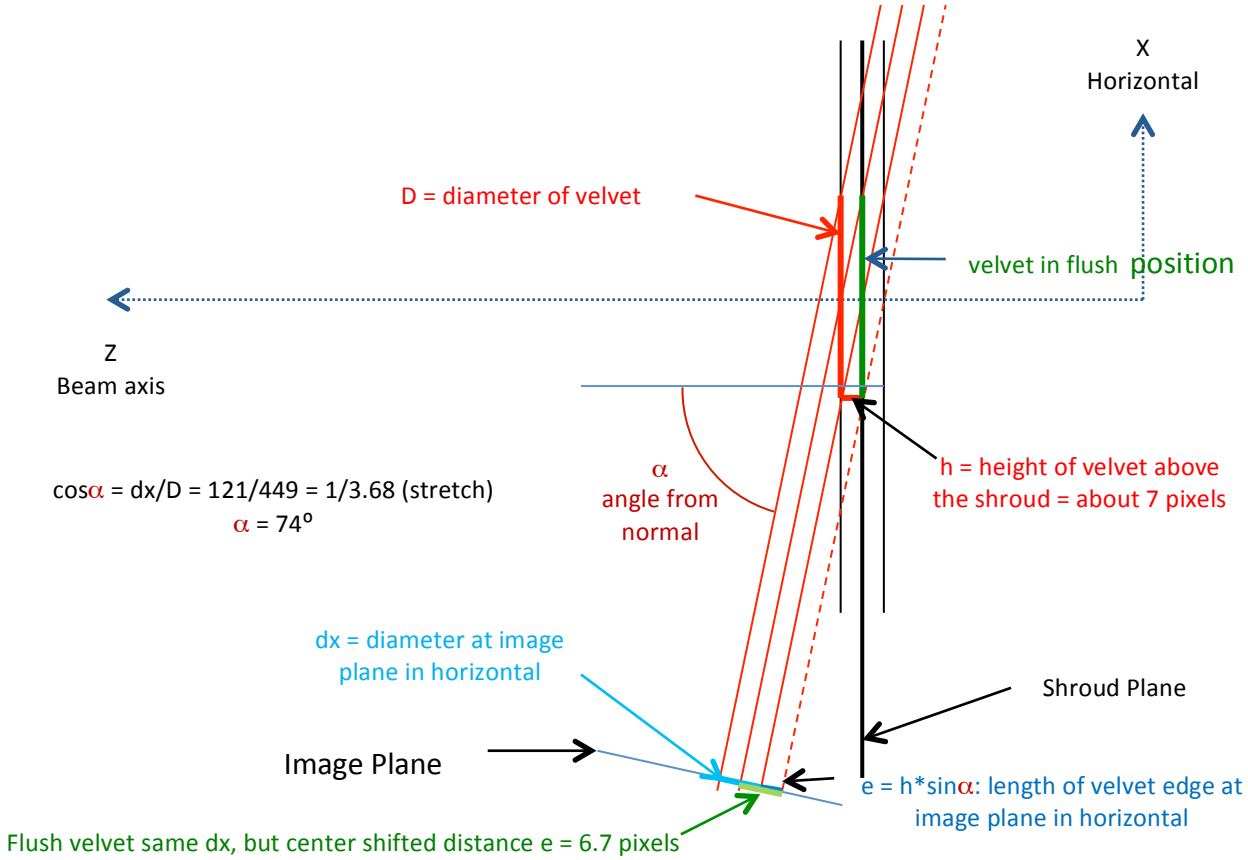

Figure G-1. Simplified sketch of the cathode velvet surface as viewed from the camera is shown.

The camera is located at a finite distance from the velvet and parallax needs to be considered. Figure G-3 provides a sketch of this issue. The sketch in Figure G-3 is taken looking in the horizontal at the velvet to isolate the parallax from the viewing angle issue in Figure G-1. The important number for this is the change in velvet height from the physical velvet to the image velvet at the image plane compared to the distance between the velvet to the image plane. What is calculated for the correction term as the velvet is moved with respect to the shroud is a change of only 0.03 mm that is much less than can be measured with the camera system. This figure is also insignificant compared to the viewing angle correction of 6.7 pixels (0.85 mm).

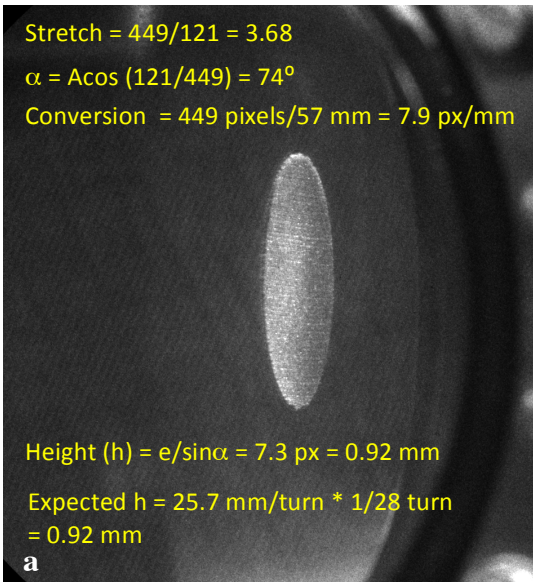

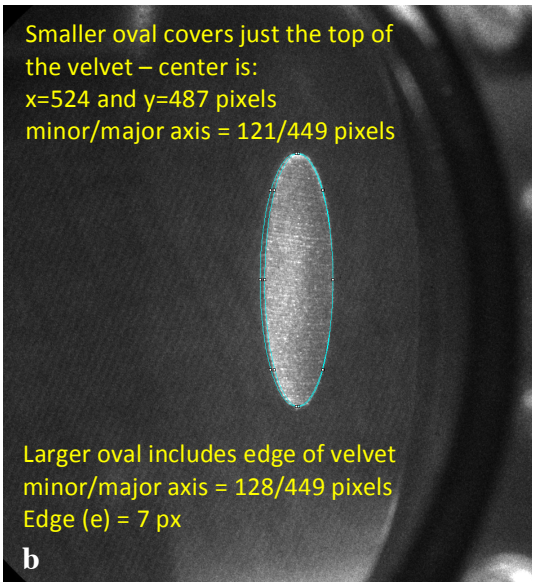

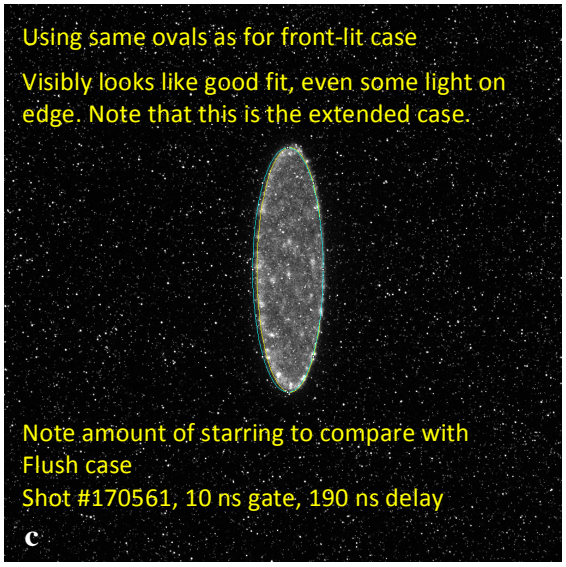

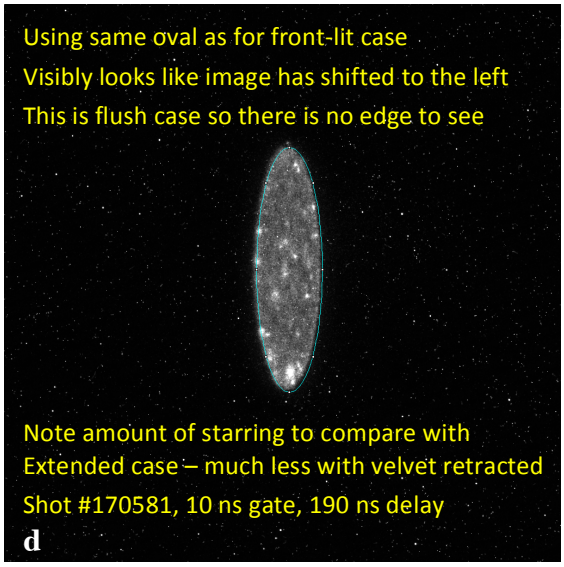

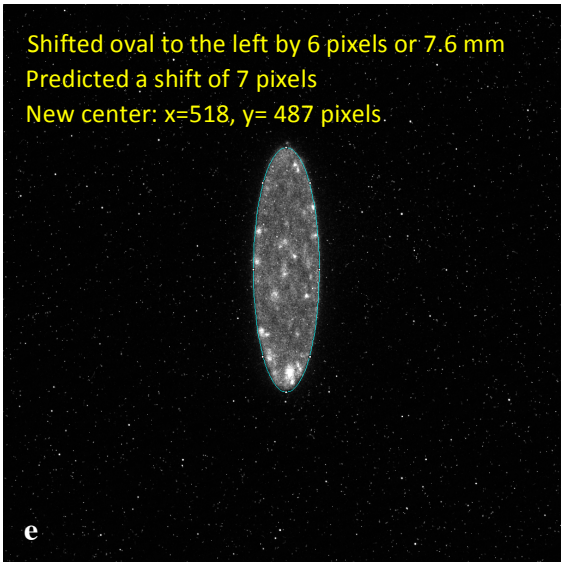

Figure G-2. Images of the front-lit cathode with extended velvet are shown in figures a and b. Figure G-2 b has two ovals inscribing the surface and the surface with edge of the velvet. Figure G-2 c is a cathode image with the velvet extended with ovals located as in Figure G-2 b to highlight the velvet surface and edge. Figures d and e are cathode images of the flush velvet used to highlight the shift of the apparent velvet center.

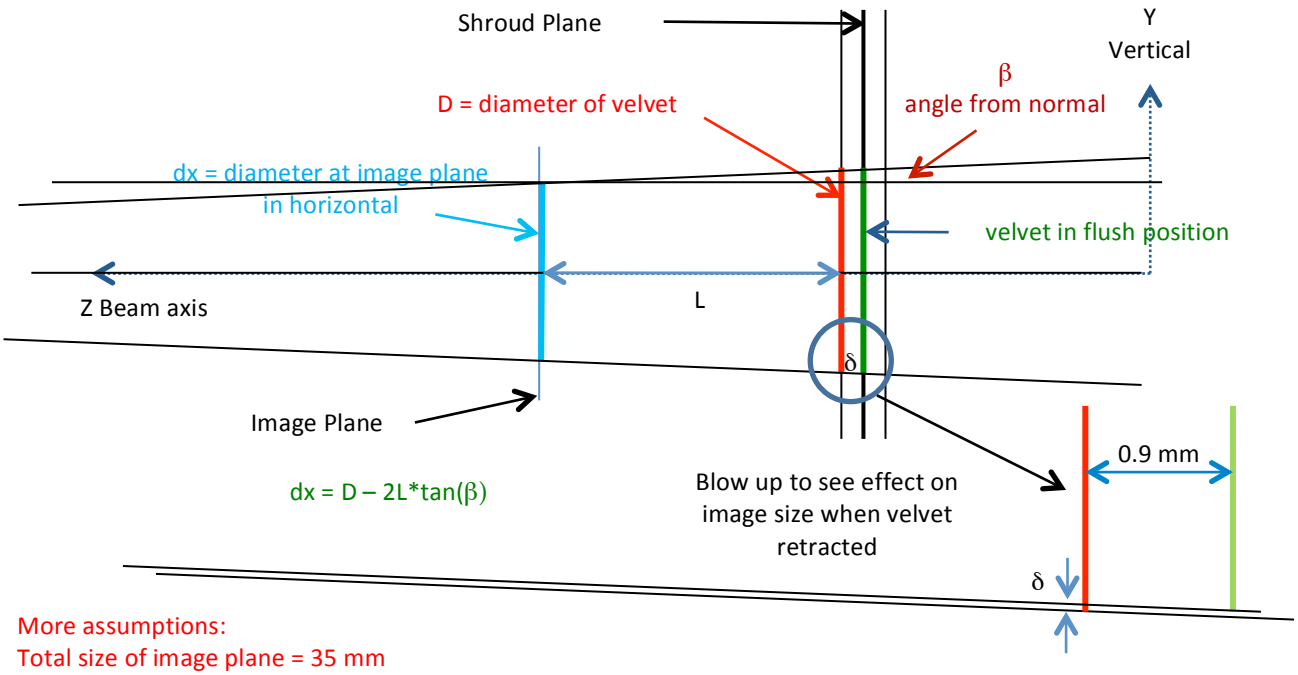

More assumptions:
Total size of image plane = 35 mm
Velvet height on image plane = 35 mm * 449 px/1024 px ~ 15 mm
L ~ 144 cm + 13.5 cm = 157.5 cm
β = Atan[(D-dx)/2L] = 0.8°

Tanβ = D/(L+0.9mm) = (D-δ)/L
δ = 0.9D/L/(1-0.9/L) = 0.03 mm
effect to small to resolve

Figure G-3. Simplified sketch showing the effect of parallax due to the finite distance of the camera from the cathode.